UNIVERSIDAD COMPLUTENSE DE MADRID

FACULTAD DE CIENCIAS FÍSICAS
Departamento de Física Teórica I

TESIS DOCTORAL

Indirect searchers of TeV dark matter

Búsqueda indirecta de materia oscura a la escala de TeV

MEMORIA PARA OPTAR AL GRADO DE DOCTOR

PRESENTADA POR

Viviana Gammaldi

Directores
José Alberto Ruiz Cembranos
Antonio López Maroto

Madrid, 2016

Universidad Complutense Madrid

Doctoral Thesis

Indirect Searches of TeV Dark Matter.

Búsqueda indirecta de materia oscura a la escala del TeV.

Author:
Viviana Gammaldi

Supervisors:
Prof. Jose A. R. Cembranos
Prof. Antonio L. Maroto

A thesis submitted in fulfilment of the requirements for the degree of Doctor of Physics

in the

Departamento de Física Teórica I

July 10, 2015

No te rindas - Mario Benedetti

No te rindas, aún estás a tiempo
De alcanzar y comenzar de nuevo,
Aceptar tus sombras,
Enterrar tus miedos,
Liberar el lastre,
Retomar el vuelo.
No te rindas que la vida es eso,
Continuar el viaje,
Perseguir tus sueños,
Destrabar el tiempo,
Correr los escombros,
Y destapar el cielo.
No te rindas, por favor no cedas,
Aunque el frío queme,
Aunque el miedo muerda,
Aunque el sol se esconda,
Y se calle el viento,
Aún hay fuego en tu alma
Aún hay vida en tus sueños.
Porque la vida es tuya y tuyo también el deseo
Porque lo has querido y porque te quiero
Porque existe el vino y el amor, es cierto.
Porque no hay heridas que no cure el tiempo.
Abrir las puertas,
Quitar los cerrojos,
Abandonar las murallas que te protegieron,
Vivir la vida y aceptar el reto,
Recuperar la risa,
Ensayar un canto,
Bajar la guardia y extender las manos
Desplegar las alas
E intentar de nuevo,
Celebrar la vida y retomar los cielos.
No te rindas, por favor no cedas,
Aunque el frío queme,
Aunque el miedo muerda,
Aunque el sol se ponga y se calle el viento,
Aún hay fuego en tu alma,
Aún hay vida en tus sueños
Porque cada día es un comienzo nuevo,
Porque esta es la hora y el mejor momento.
Porque no estás solo, porque yo te quiero.

Non ti arrendere - Mario Benedetti

Non ti arrendere, c'é ancora tempo
per arrivare e ricominciare
accettare le tue ombre
seppellire le tue paure
liberarti del fardello
riprendere il volo.
Non ti arrendere perché questo é la vita
continuare il viaggio
perseguire i sogni
sciogliere il tempo
togliere le macerie
e scoperchiare il cielo.
Non ti arrendere, per favore non cedere
malgrado il freddo bruci
malgrado la paura morda
malgrado il sole si nasconda
e taccia il vento
c'é ancora fuoco nella tua anima
c'é ancora vita nei tuoi sogni
Perché la vita é tua e tuo anche il desiderio
perché l'hai amato e perché ti amo
perché esiste il vino e l'amore, é certo
perché non vi sono ferite che non curi il tempo
Aprire le porte
togliere i catenacci
abbandonare le muraglie che ti protessero
vivere la vita e accettare la sfida
recuperare il sorriso
provare un canto
abbassare la guardia e stendere le mani
aprire le ali
e tentare di nuovo
celebrare la vita e riprendere i cieli
Non ti arrendere, per favore non cedere
malgrado il freddo bruci
malgrado la paura morda
malgrado il sole si nasconda e taccia il vento
c'é ancora fuoco nella tua anima
c'é ancora vita nei tuoi sogni
perché ogni giorno é un nuovo inizio
perché questa é l'ora e il momento migliore
perché non sei sola, perché ti amo.

Don't Give Up - Mario Benedetti

Don't give up, you still have time
to reach up and start anew,
Accept your shadows,
Bury your fears,
Free your burdens,
Fly again.
Don't give up, that's what life is
Continue the journey,
Follow your dreams,
Unstuck time,
Move the rubble,
And uncover the sky.
Don't give up, please don't give way,
Even if the cold burns,
Even if fear bites,
Even if the sun sets,
And the wind goes silent,
There is still fire in your soul
There is still life in your dreams.
Because life is yours and yours is the desire
Because you have loved it and because I love you
Because wine exists and love is true.
Because there are no wounds that time doesn't cure.
To open the doors,
Take away the locks,
Abandon the walls that have protected you,
To live life and accept the challenge
Get back laughter,
Practice a song,
Lower the guard and extend the hands
Open the wings
And try again,
Celebrate life and take back the skies.
Don't give up, please don't give way,
Even if the cold burns,
Even if fear bites,
Even if the sun sets,
And the wind goes silent,
There is still fire in your soul
There is still life in your dreams.
Because every day is a new beginning,
Because this is the hour and the best moment.
Because you are not alone, because I love you.

Acknowledgements

Firstly, I would like to acknowledge the contribution of my Ph.D. supervisors, Prof. Antonio Lopez Maroto and Prof. Jose Alberto Ruiz Cembranos, to this work. This thesis would have never been possible without their help. They showed to me how to do research.

This work has been funded by UCM predoctoral grant, MICINN (Spain) project numbers FIS 2008-01323, FIS2011-23000, FPA2011-27853-01, Consolider-Ingenio MULTIDARK CSD2009-00064, and the Department of Energy, Contract DE-AC02-76SF00515. During the period of this work I had the chance to collaborate with Dr. Roberto Lineros at *Instituto de Física Corpuscular* (IFIC, CSIC-UV) in Valencia. I would like to thank him particularly, for his quality as researcher and for his pleasantness. I would also like to acknowledge the collaboration of Dr. Álvaro de la Cruz-Dombriz in this thesis. Finally, I thank Prof. Vladimir Avila-Reese and the collaboration of the *Instituto de Astrofísica* (IA) of *Universidad Autónoma de Mexico* (UNAM) and *Becas Santander Iberoamérica Jóvenes Profesores e Investigadores y Alumnos de Doctorado. España 2015* that made possible this collaboration.

Recuerdo perfectamente mis primeros días en España y en Madrid.

En primer lugar, quiero volver a mostrar mi agradecimiento a Antonio y José Alberto de una forma más informal. Ellos *me eligieron* y me dieron la oportunidad de venir a España, y aprender muchas cosas más que la *simple* física. Aquí he aprendido un idioma, una cultura, una forma de vivir única en el mundo. Han sido estupendos conmigo.

Quiero mostrar mi agradecimiento particular a JAR, jefe y compañero de departamento. Recuerdo perfectamente las miles de vueltas por Madrid por hacer todo el papeleo y este momento en el metro en que me dijo *You seem sad* y le contesté *I'm not sad. I'm just afraid, a bit.* No tenía de que tener miedo. Una grande aventura iba a empezar.

Quiero agradecer a Carol, Andrea y Enzo por haberme dado un techo los primeros días y haberme introducido a la locura de Madrid.

La primera persona que conocí en el departamento fue Marco, y probablemente es la persona con que más horas he compartido en estos cuatro años: todos los días en el despacho y la mayoría de los fines de semana por Madrid. La segunda persona que conocí fue Domingo. Nunca podré olvidar la primera vez que salimos... *I'm going to an exhibition, do you want to go with me? ... mmmmh...Ok!* Y fuimos a la exposición, y luego me invita a un vino... y tengo q pagar yo, porque no tiene cartera!! Grande Domi!! Tercera persona... Bea. Otro plan improvisado de viernes por la noche... *He quedado con mis amigos por Malasaña, os apuntáis?* Domingo y yo nos miramos: *Vale!*. Muchos eventos parecidos se sucedieron en este despacho... Juan con su celebración del Guadalajara, o Édgar a las 17:00 horas de un martes: *He tomado café de verdad,*

necesito salir de fiesta. Caras perplejas por mi parte y por parte de Domingo : *Vale!* Y cómo vamos? Con el (ex)-descapotable de Domingo por supuesto... Así nació el DomiLab, más o menos. No se me olvida de los *últimos en llegar*: Santos, probablemente mi opuesto más perfecto, con que ha sido un placer compartir despacho, grupo de trabajo, viaje a Canarias, patatas fritas, habitaciones y muchos chistes, y Rafa, que con su espontaneidad nos sorprende siempre. Al DomiLab dedico mi mayor agradecimiento. A todos ellos, y a cada uno singularmente, por estar siempre allí, aunque sea desde lejos.
Todavía me falta mucha gente a la que dar las gracias. A Ginevra por muchas cosas, sobre todo, por haber compartido conmigo una *casa*. Porque ese piso ha sido mi segunda casa y no sólo una vivienda temporal, incluyendo los buenos y los malos momentos que una familia puede tener. Pero sobre todo, por nuestra aventura en California, entre los mejores momentos de mi vida.
Quiero agradecer a Markus, a Oscar, a Davide, a Alex por muchos buenos momentos entre barbacoas, tapas, cañas y muchos bailes salseros y tangueros. En particular, agradezco a Markus por sus buenos consejos sobre el trabajo y Davide por *... esta parte de los agradecimientos ha cambiado recentemiente.* Es muy triste. En la primera versión, le agradecía la experiencia de *haberme tirado de un avión (y haber sobrevivido).* Ahora, desgraciadamente, tengo que lamentar su pérdida. Empezamos nuestra aventura en Madrid práticamente a la vez, él en Octubre y yo en Enero. Nos despedimos también a la vez, pero de forma muy distinta. No hay palabras para describir lo que ha pasado. Siempre quedarás siendo el compañero de trabajo, la pareja de tango, el amigo con el que compartí la experiencia de volar, por primera (y última) vez, *Somewhere over the rainbow.* Sabía que recordaría esta canción para siempre, pero esperaba que fuera por un motivo diferente. No te olvidaré.
Quiero agradecer la Version 2.0 del DomiLab: Laura, Jeny, Giovanni, Arkaitz, Jóse, que han dado nueva vida a los departamentos de Física Teórica I y II, y que seguramente serán dignos herederos de la dinastía de Domi.
Para concluir, querría agradecer a Álvaro y Emma, que con su boda han alegrado la conclusión de esta época en Madrid. Ha sido un placer véros tan felices y compartir con vosotros y con todos este momento tan importante de vuestras vidas.
También agradezco a las amistades de Multidark: Adiv, por acogerme siempre en su casa y en la de sus amigos y por compartir la aventura mexicana, y también Simon, Alicia y Agustin. Roberto entra también dentro de este grupo. No se me olvida dentro del *grupo canario* de aventuras, a Remi y a Vlad.
Todavía no termino... me falta *el equipo de fútbol femenino* y esas personas que allí conocí y que se han vuelto amigas: Izarra, por estar siempre presente en los momentos de crisis, Punky por estar siempre en los momentos de crisis pre-charla y Cris, por su alegría constante, cada una luego y en su manera ha ocupado un lugar particular y independiente de las demás.

Quiero agradecer *los amigos de amigos* que me han acogido como una de ellos: Joserra, Berto, Javi, Itxi, Jesus, Lon, Jorge, Oscar, perdonad si se me ha olvidado hacer el nombre de alguien. Todos los que han venido a verme a Nápoles, y todos los que vendrán a Trieste.
Falta el grupo tanguero todavía, donde poco a poco han ido formándose amistades importantes: destaco el nombre de Francesco por su consejos en tema de becas europea, y agradezco a todos los demás por los bailes y los buenos momentos vividos juntos. Lo mismo hago con el grupo salsero. Salseros y tangueros me váis a perdonar que no haga un elenco con los nombre de todos, cada uno de vosotros sabe lo importante que ha sido para mí. La vida en Madrid no habría sido la misma sin nuestras diversiones juntos.

Adesso, mi tocca iniziare a parlare in italiano. É un pó come chiudere un capitolo e tornare alle origini. Ringrazio mia madre Anna Rosaria e mio padre Francesco per avermi fatto sempre scegliere liberamente, per aver sostenuto le mie scelte e per affrontare con me quello che significa stare lontano dalle persone a cui vuoi bene. Li ringrazio, per avermi dato ognuno di loro una parte di sé, molto diverse tra loro, che hanno creato una persona probabilmente tra le piú complesse al mondo, con i suoi pregi e i suoi difetti. Ringrazio mio fratello Sergio, per essere lí dove le mie scelte non mi fanno essere. Ringrazio tutta la mia famiglia, Patrizia, Mariella, Manu, Armando, Checco e Chiara, nonno Sergio, per tutti i consigli di vita, e per esserci sempre quando si ha bisogno di loro. Ringrazio i familiari *acquisiti*, che sono piú vicini di me alle persone a me care e li rendono felici. Ringrazio anche zio Carlo e zia Grazia, Valentina e Carlotta, per il nuovo rapporto recuperato, che spero si conservi nel tempo. Ringrazio tutti coloro che sono venuti a trovarmi a Madrid, ma anche quelli che non sono venuti. I miei amici di sempre, Gianpaolo, Roberta, Sasy, Claudia, Nello, Federica, Davide, Ornella, Panda, Valerio, Valeria, Paolo, Claudio, perché tutte le volte che torno mi fanno sentire come se non fossi mai andata via. Ringrazio le amicizie perenni, Luna, Eleonora, Anna, che sia dove sia nel mondo, sicuro che continueremo vedendoci, anche se non tutti i giorni come ai tempi del liceo e dell'universitá. Mi vengono in mente tante altre persone da ringraziare, persone con le quali magari non sono piú in contatto, ma che hanno fatto sí che sia la persona che sono.

I also thank to all the travel friends, that people that you met once in your life, that gave you something important and unique before vanishing forever.

Publications

- *Antiproton signatures from astrophysical and dark matter sources at the galactic center*,
  J. A. R. Cembranos, V. Gammaldi, A. L. Maroto, JCAP 03 (2015) 041.

- *Neutrino fluxes from Dark Matter in the HESS J1745-290 source at the Galactic Center*,
  J. A. R. Cembranos, V. Gammaldi, A. L. Maroto, Phys. Rev. D 90, 043004 (2014).

- *Reliability of Monte Carlo event generators for gamma ray dark matter searches*,
  J. A. R. Cembranos, A. de la Cruz-Dombriz, V. Gammaldi, R. A. Lineros, A. L. Maroto, JHEP 1309 (2013) 077.

- *Spectral Study of the HESS J1745-290 Gamma-Ray Source as Dark Matter Signal*,
  J. A. R. Cembranos, V. Gammaldi, A. L. Maroto, JCAP 1304 (2013) 051.

- *Dark matter origin of the gamma ray emission from the galactic center observed by HESS*,
  J. A. R. Cembranos, V. Gammaldi, A. L. Maroto, Phys. Rev. D 86, 103506 (2012).

- *Detection of branon dark matter with gamma ray telescopes*,
  J.A.R. Cembranos, A. de la Cruz-Dombriz, V. Gammaldi, A.L. Maroto, Phys. Rev. D 85, 043505 (2012).

These works have been also presented in international conferences:

- *Highlights on gamma rays, neutrinos and antiprotons from TeV Dark Matter*,
  Viviana Gammaldi,
  Proceeding of RICAP-14 "The Roma International Conference on Astroparticle Physics".

- *Gamma-ray and neutrino fluxes from Heavy Dark Matter in the Galactic Center*,
  V. Gammaldi, J. A. R. Cembranos, A. de la Cruz-Dombriz, R. A. Lineros, A. L. Maroto,
  Proceedings of TAUP2013 "13th International Conference on Topics in Astroparticle and Underground Physics".

- *Cosmic Rays from Heavy Dark Matter from the Galactic Center*,
  Jose A. R. Cembranos, Viviana Gammaldi, Antonio L. Maroto,
  Proceedings of the "European Physical Society Conference on High Energy Physics" EPS-HEP2013, 18-24 July 2013, Stockholm (Sweden).

- *Indirect constraints to branon dark matter*,
  J. A. R. Cembranos, A. de la Cruz-Dombriz, V. Gammaldi, A. L. Maroto,
  Contribution to the Proceedings of Spanish Relativity Meeting ERE2011, Madrid 29 August - 2 September 2011.

- *Dark matter with photons*,
  Álvaro de la Cruz-Dombriz, Viviana Gammaldi,
  Proceedings of PHOTON11 "International Conference on the Structure and the Interactions of the Photon"

Resumen

El problema de la existencia de la materia oscura (DM) es una cuestión de gran importancia para la física del siglo XXI. El Modelo Cosmológico Estándar proporciona una buena descripción de la evolución del Universo, de acuerdo con los datos de experimentos como COBE, WMAP y PLANCK. Según este modelo, el 69.2% del contenido de energía del Universo está constituido por un tipo de energía oscura con presión, responsable de la expansión acelerada, el 26.8% por DM, mientras que la componente conocida de la materia sería sólo alrededor del 5% del total. Sin embargo, la componente oscura de la materia se ha detectado hasta ahora sólo por medio de pruebas gravitacionales. En el caso de que dicha componente esté constituida por partículas, distintos experimentos de búsqueda directa e indirecta en tierra y en satélites, podrían detectar esta nueva partícula por medio de su interacción con la materia ordinaria y también a través de los productos secundarios de su aniquilación y desintegración en fuentes astrofísicas. Desde un punto de vista más teórico, la búsqueda de DM incluye modelos más allá del Modelo Estándar (SM) de partículas elementales, modelos de supersimetría y dimensiones extra. Una introducción más detallada a la cosmología y al problema de la DM se presenta en el Capítulo 1, mientras que en el Capítulo 2 introducimos la búsqueda de DM en colisionadores de partículas y en experimentos de búsqueda directa e indirecta.

La mayoría de los estudios sobre DM se han centrado hasta ahora en partículas de masas menores de 1 TeV. Sin embargo, el límite superior en la masa para DM térmica alcanza los 100 TeV. Este tipo de DM a escala del TeV (TeVDM) es particularmente atractiva, teniendo en cuenta la ausencia de evidencias experimentales con respecto a la existencia de DM a masas mas bajas. En esta tesis se desarrolla una investigación multi-canal desde un punto de vista fenomenológico de la posibilidad de detección de materia oscura pesada. En particular, se demostrará que el flujo de rayos gamma observado por el telescopio HESS desde la fuente J1745-290 situada en el centro galáctico (GC) puede ser ajustado como una señal de DM más una componente de fondo. La señal de HESS había sido anteriormente analizada en el contexto de materia oscura supersimétrica y en teorías con dimensiones extra. En esta tesis se abre una nueva posibilidad de interpretación de la misma señal como TeVDM. El nuevo análisis se presenta en el Capítulo

3. El flujo en rayos gamma proveniente desde el GC ha sido observado también por FERMI-LAT. La fuente J1745.6-29000 observada por FERMI-LAT a energías entre 2-300 GeV coincide con la fuente J1745-290 observada por el telescopio HESS, que muestra un corte en el flujo de rayos gamma alrededor de 30 TeV. El ajuste desarrollado proporciona excelentes ajustes a los datos para una masa de la DM entre 10 y 100 TeV para casi todos los canales de aniquilación. En trabajos anteriores se descartó la posibilidad de explicar los datos de HESS como aniquilación de partículas de DM supersimétrica o de Kaluza-Klain de masa menor de 10 TeV, sin la componente de ley de potencia para describir el fondo. Nuestro análisis es independiente del modelo, sin embargo, estudiamos el caso particular de los branones. En concreto DM con masas alrededor de los 50 TeV constituida por branones que se aniquilan principalmente en una combinación de W^+W^- y ZZ explicaría los datos de HESS y FERMI-LAT entre 1 GeV y 50 TeV. Para obtener este resultado, hemos desarrollado los siguientes análisis.

En primer lugar, en el Capítulo 4 consideramos los branones como posibles candidatos de DM. Los branones son fluctuaciones masivas de una brana, es decir nuevos campos escalares cuyo acoplamiento con las partículas del SM es inversamente proporcional a la tensión f^4 de la brana. En este Capítulo, analizamos el flujo mínimo de rayos gamma producidos en la aniquilación de brenones en varias fuentes astrofísicas, como galaxias enanas y el centro de la Galaxia, que podría ser detectado en un amplio intervalo de masas y estimamos la sensibilidad de diversos experimentos, tanto satélites como telescopios Cherenkov en tierra. Los resultados son compatibles con la falta de detección de una señal de rayos gamma con las posibles combinaciones de fuentes y telescopios analizadas. Sin embargo, estos análisis también sugieren que futuros experimentos como CTA serán capaces de detectar un posible flujo de rayos gamma generados por branones con masas por encima de 150 GeV.

En segundo lugar, desarrollamos una comprobación de los resultados obtenidos con análisis adicionales de flujos secundarios de otros rayos cósmicos esperados para el mismo candidato de DM con la misma distribución de densidad en la Galaxia. Para desarrollar estos análisis, hay que tener en cuenta que la TeVDM térmica necesita un factor astrofísico más grande que el estándar para explicar el flujo observado de rayos gamma. Motivado por el reciente descubrimiento por parte de IceCube de varios neutrinos astrofísicos de alta energía, hemos realizado un análisis detallado sobre la posible detección de un flujo de neutrinos emitidos por aniquilación de DM a la escala del TeV en el centro galáctico. Entre los resultados de este trabajo presentamos explícitamente la mejor combinación de área efectiva, ángulo de resolución y tiempo de exposición necesarias para detectar el flujo de neutrinos esperado. Como mostramos en el Capítulo 5, esto podría ser interesante para futuras observaciones de esta región tanto con la generación actual de telescopios de neutrinos como con futuros experimentos como KM3NeT.

En el Capítulo 6, hemos estudiado el flujo de antiprotones que podría ser generado por

una fuente puntual en el GC. De hecho, la fuente puntual representa una buena aproximación para nuestro candidato, debido a la resolución angular del telescopio HESS, a la dimensión angular de la fuente J1745-290 y a su distancia desde el GC. Hemos considerado tres espectros de emisión diferentes que podrían ser asociados con diferentes fuentes astrofísicas. Para los tres casos espectrales, encontramos que la detección de antiprotones producidos por este tipo de fuente puntual en el GC no es prometedora, debido a la difusión de los antiprotones en la Galaxia y a la ausencia de una descripción detallada de dicha difusión en la parte mas interna de la Galaxia. La hipótesis de una fuente puntual es de particular importancia para la emisión y propagación de los antiprotones. De hecho, un aumento local en la densidad de DM es conceptualmente muy distinto a un aumento en el valor de la sección eficaz de aniquilación, que tendría un efecto global en toda la distribución de DM en el halo de la Galaxia. En el Capítulo 6 demostramos que en ambos casos el flujo de antiprotones generado por TeVDM queda por debajo del flujo difuso detectado por PAMELA. Por otro lado, DM de menor masa, alrededor de 100 GeV, queda excluida por este tipo de análisis. Finalmente en el Capítulo 7, discutimos ciertas incertidumbres asociadas con la búsqueda indirecta de DM. Como normalmente se hace en la literatura, todos los análisis presentadas en esta tesis, utilizan simulaciones Monte Carlo de los eventos de aniquilación y desintegración. Estas simulaciones pueden ser desarrolladas con diferentes códigos. PYTHIA y HERWIG son los más populares, ambos en las dos versiones de FORTRAN y C++. Por ejemplo, estudiamos el flujo de rayos gamma generado por los cuatro códigos, concretamente PYTHIA 6.4 y 8 (versiones FORTRAN y C++) y HERWIG y HERWIG++. Las cuatro simulaciones presentan diferencias no solamente en la forma del espectro, sino también en el número de fotones emitidos en cada evento. El origen de estas diferencias puede encontrarse en la distinta implementación y modelización de la electrodinámica y cromodinámica cuánticas así como en el proceso de hadronización. En el caso particular de los fotones, tiene particular importancia la distinta implementación del efecto de Bremsstrahlung para leptones de altas energías. Estas incertidumbres pueden afectar en particular a la estimación del factor astrofísico y/o a la del valor de las secciones eficaces de aniquilación. Los resultados presentados en esta tesis muestran que aunque un candidato de TeVDM parezca ser compatible con los datos de rayos gamma, neutrinos y antiprotones, necesitamos más resultados experimentales para comprobar o rechazar este modelo. En particular, estudio detallado de las propiedades de estas partículas en aceleradores y experimentos de búsqueda directa será fundamental en un futuro próximo para comprobar o rechazar la hipótesis de TeVDM, como discutimos en las conclusiones de esta tesis (Capítulo 8).

Preface

The problem of the existence and nature of the dark component of matter represents an important issue of the physics of the XXI Century. The Cosmological Standard Model in accordance with satellite experiments such as the Cosmic Background Explorer (COBE), Wilkinson Microwave Anisotropy Probe (WMAP) and PLANCK, represents a good description of the Universe and its evolution. Based on this model, the 69.2% of the total mass-energy content of the Universe today is made of a kind of fluid with negative pressure, that is responsible for the present state of accelerating expansion and that is called dark energy. The ordinary matter we know corresponds to merely a few percent (4.9%) of the total amount, while the 26.8% is made of a kind of Dark Matter (DM) that is still unknown. However, apart from gravitational probes, this unknown component of the matter remains undetected. On the experimental side, assuming that DM admits a description in terms of new particles, collider experiments as well as direct and indirect searches are addressed to reveal the presence of these particles on the Earth, through the interaction with ordinary matter, and detect the secondary products of their annihilation/decay in astrophysical sources. From the theoretical point of view, the research on the DM nature covers concepts of particle physics beyond the Standard Model (SM), such as Supersymmetry and Extra-dimensions. A more detailed introduction to cosmology and on the DM problem, observations and theory, is presented in Chapter 1, whereas in Chapter 2 we introduce the search of DM at colliders and the direct and indirect experiments.

The majority of these searches have focused on DM with masses below 1 TeV, although the thermal limit extents to approximately 100 TeV. In this thesis, we will follow a phenomenological approach to the DM problem, paying particular attention to the mass range between 1-100 TeV. This type of TeV Dark Matter (TeVDM) is attracting more attention given the lack of convincing evidences of the existence of DM of lower masses. In particular, we develop a multi-messenger analysis of cosmic-rays detection from astrophysical sources. We show that the gamma-ray flux observed by HESS from the J1745-290 Galactic Center (GC) source is well fitted as the secondary gamma-ray photons generated from DM annihilating into SM particles, in combination with a simple

power law background. Although the HESS signal has been analyzed in previous works, we present a new analysis which opens the possibility of a TeVDM interpretation. This result could motivate new experimental and theoretical developments.

The new analysis is discussed in Chapter 3. Both FERMI-LAT and HESS telescopes observed the GC region in gamma rays. The FERMI-LAT 1FGL J1745.6-2900 source is spatially coincident with the HESS source J1745-290. The FERMI-LAT data between 2-300 GeV are well fitted by a power law. Instead, a bump appears in the HESS data around the TeV scale and a cut-off around 30 TeV. We perform model independent fits for all the possible channels of annihilation of DM into SM particles. The resulting DM mass is above ~ 10 TeV for all the annihilation channels. Previous works discarded the possibility to fit the HESS data with a supersymmetric or Kaluza-Klain DM particle of lower mass, without the background component. Although our analysis is model independent, we have studied the case of branon DM as a viable example. A branon DM candidate with a mass of ~ 50 TeV annihilating in a combination of W^+W^- and ZZ channels well fits both the HESS and FERMI-LAT data between 1 GeV and 50 TeV. Motivated by this result, we have cross-checked this hypothesis.

Firstly, we consider branon as a prospective DM candidate in Chapter 4. Branons are massive brane fluctuations, that are new scalar fields whose coupling to the SM particles is suppressed by the brane tension f. We analyse the minimum detectable flux for a broad range of branon masses. We check the sensitivity of several satellites and Cherenkov telescopes to the prospective secondary gamma-ray flux generated by branon annihilation in different astrophysical sources, as dwarf spheroidal galaxies and the GC itself. The results are in agreement with *no-detection* of further gamma-ray signals with the available combination of observed sources and selected devices. However, the analysis allows to set constraints on the prospective detection of a gamma-ray flux generated from annihilation of branons with masses smaller than ~ 1 TeV.

Secondly, we develop the cross-check of the results obtained for the gamma-ray signal in the GC with additional analyses of other secondary cosmic-ray fluxes, that should be expected from the same DM candidate and distribution. In order to develop these analyses, we need to underline that the secondary gamma-ray flux generated by annihilating thermal TeVDM needs a large astrophysical factor in order to well fit the HESS data at the GC. Motivated by the recent detection of a number of neutrinos of astrophysical origin by the IceCube telescope, we drew conclusions on the possible detection of the neutrino flux emitted by the TeVDM candidate at the GC. We give explicitly the better combination of effective area, resolution angle and exposition time that is required to detect the expected neutrino signal from the GC source. As shown in Chapter 5, this could be of interest for future observations of the region with the current generation of neutrino telescope or next experiments such as KM3NeT.

Moreover, we study the antiproton flux that should be generated from a point-like source

at the GC. In fact, the point-like source represents a good approximation, because of both the angular resolution of the HESS telescope and the angular dimension of the J1745-290 source and the distance of the GC from the observer at the Earth. We consider three different spectra that can be associated with different sources. For all the spectral cases, we found that antiprotons detection from such point-like source at the GC is not promising so far, due to antiproton propagation in the Galaxy and the absence of a detailed description of antiproton diffusion at the inner region of GC. The hypothesis of point-like source is of particular interest for antiproton emission and propagation. In fact, a local enhancement in the DM distribution is conceptually very different with respect to a global boost in the thermal annihilation cross-section. In the latter case, the whole DM halo should be affected. In Chapter 6 we show that in both cases, the antiproton flux generated by a TeVDM particle lies below the diffuse antiproton flux detected by PAMELA. Instead, lighter DM masses around 100 GeV are more constrained by this kind of analysis.

Finally in Chapter 7, we discuss the Monte Carlo event generator uncertainties associated with indirect searches. As usual in the literature, all the previous analyses make use of Monte Carlo simulation of the secondary products of annihilation and decay events. Such simulations can be developed with different codes. `PYTHIA` and `HERWIG` are the most popular ones, both in the two FORTRAN and C++ versions. As an example, we study the gamma-ray flux generated by four codes, namely `PYTHIA` 6.4 and 8 (FORTRAN and C++ version, respectively) and `HERWIG` and `HERWIG++`. The four simulations present differences not only in the spectral form, but also in the multiplicity of the number of emitted photons. The reason can be found in a different implementation and modelization of the QED, QCD and hadronic shower. In this particular case, the different implementation of Bremsstrahlung effect for high-energy leptons is very important. Such uncertainties may affect the estimation of astrophysical factors and/or annihilation cross sections.

This fact and the results presented so far, show that although our TeVDM candidate appears in agreement with gamma-ray, neutrino and antiproton data from indirect searches, more experimental probes are required. In particular, an improvement in the research of heavy particles at colliders and with the direct searches will be fundamental in the next future in order to confirm or reject the TeVDM hypothesis, as we discuss in the conclusions of this thesis (Chapther 8).

Contents

Abbreviations

ATC	**A**tmospheric **C**herenkov **T**elescope
CC	**C**harged **C**urrent
CMB	**C**osmic **M**icrowave **B**ackground
CTA	**C**herenkov **T**elescope **A**rray
DM	**D**ark **M**atter
dof	**d**egree **o**f **f**reedom
EW	**E**lectro**W**eak
FSR	**F**inal **S**tate **R**adiation
GC	**G**alactic **C**enter
GR	**G**eneral **R**elativity
HESS	**H**igh **E**nergy **S**petroscopic **S**ystem
ISM	**I**nter**S**tellar **M**atter
LHC	**L**arge **H**adronic **C**ollider
LSP	**L**ightest **S**upersymmetric **P**article
LKP	**L**ightest **K**aluza-Klein **P**article
MSSM	**M**inimally **S**upersymmetric **S**tandard **M**odel
NC	**N**eutral **C**urrent
NFW	**N**avarro **F**rank **W**hite DM density distribution profile
pMSSM	**p**henomenological **M**inimally **S**upersymmetric **S**tandard **M**odel
PWN	**P**ulsar **W**ind **N**ebulae
QCD	**Q**uantum **C**hromo **D**ynamics
QED	**Q**uantum **E**lectro **D**ynamics
SCM	**S**tandard **C**osmological **M**odel
SM	**S**tandard **M**odel
SNR	**S**uper**N**ovae **R**emnats

SUSY	**SU**per **SY**mmetry
TOA	**T**op **O**f **A**tmosphere
UED	**U**niversal **E**xtra **D**imensions
VHE	**V**ery **H**igh **E**nergy
WIMP	**W**eakly **I**nteracting **M**assive **P**article

Symbols

Affine Connections	$\Gamma^{\mu}_{\alpha\beta}$
Affine Parameter	λ
Altarelli-Parisi splitting function	$P^{\mathrm{MC}}_{i,jk}(z)$
Amplitude (annihilation processes)	$\mathcal{M}$
Angular Resolution	$\Delta\Omega$
Antiproton Diffusion Factors	A_m, S_m, Π_m
Antiproton Diffusion Function	$R_{\bar{p}}(r, E_{\bar{p}})$
Antiproton Diffusion Model Parameters	K_0, Δ
Antiproton Inelastic Annihilation Cross-section	$\sigma^{\mathrm{inel}}_{p\bar{p}}$
Antiproton Momentum	p
Antiproton Monochromatic Function	$Q^{\mathrm{M}}_E(E_{\bar{p}})$
Antiproton Monochromatic Normalization	$Q^{0-\mathrm{M}}_E$
Antiproton Monochromatic Total Emission Normalization	$A^{(\bar{p})}_M$
Antiproton Number Density per Unit Energy	$f_{\bar{p}}(t, \vec{r}, E_{\bar{p}})$
Antiproton Kinetic Energy	$E_{\bar{p}}$
Antiproton Power-law Function	$Q^{\mathrm{PL}}_E(E_{\bar{p}})$
Antiproton Power-law Normalization	$Q^{0-\mathrm{PL}}_E$
Antiproton Power-law Spectral Index	$B^{(\bar{p})}_{\mathrm{PL}}$
Antiproton Power-law Total Emission Normalization	$A^{(\bar{p})}_{\mathrm{PL}}$
Antiproton Primary Source	$\hat{Q}(t, \vec{r}, E_{\bar{p}})$
Antiproton Space Diffusion Coefficient	$K(E)$
Antiproton Spatial Distribution Function	$Q_X(\vec{r})$
Antiproton Spatial Distribution Normalization Constant	Q^0_X
Antiproton Spectral Shape Function	$Q_E(E_{\bar{p}})$
Antiproton Velocity	$v_{\bar{p}}$

Astrophysical factor	$\langle J \rangle$
Bessel Function of n-th Order	J_n
Bessel Function, m-th Order Zero	ζ_m^J
Boost factor	b
Brane Tension Scale	f
Branon Effective Lagrangian	$\mathcal{L}_{Br}$
Branon Field	π^α
CMB Temperature	$T_{\rm CMB}$
Convective Velocity	V_c
Coordinate System	$\vec{x} \equiv \left(x^\alpha, x^\beta, \ldots x^\mu\right)$
Cosmic-ray Background Flux	Φ_{cr-Bg}
Cosmic-ray Flux at the Observer	Φ_{cr}
Cosmic-ray Flux at the Source	Φ_{cr}^0
Cosmic-ray Number	$N^{(cr)}$
Cosmological Constant	Λ
Cosmological Density Parameter: Baryon Matter	Ω_B
Cosmological Density Parameter: Cosmological Constant	Ω_Λ
Cosmological Density Parameter: Curvature	Ω_{k_C}
Cosmological Density Parameter: Dark Matter	$\Omega_{\rm DM}$
Cosmological Density Parameter: Matter	Ω_M
Cosmological Density Parameter: Radiation	Ω_R
Cosmological Scale Factor	$a_C(t)$
Critical Energy Density	ϵ_{cr}
Cut-off Energy	E_{Cut}
Dark Matter Mass	$m_{\rm DM}$
Decay Time	$\tau^{\rm decay}$
Density Distribution	$\rho(r)$
Density Distribution Parameter: Constant density	ρ_s
Density Distribution Parameter: Overall Normalization	A_s
Density Distribution Parameter: Scale Radius	r_s
DM-nucleon Scattering Rate of Events	$\mathcal{R}$
Effective Area	A_{eff}
Einasto's index	n_s

Energy	E
Energy of particle ρi	$E_{\rho i}$
Energy Density	ϵ_C
Energy-Momentum Tensor	$T_{\alpha\beta}$
Exposition time	t_{exp}
Extra Dimension Volume	D_{ex-d}
Fermi's Constant	G_{F}
Fisk Potential	ϕ_F
η-Factor	η_{cr}
κ-Factor	$\kappa_{\bar{cr}}$
Galactic Mass	M
Galactic Halo Half-Hight	L
Galactic Plane Half-Hight	h_D
Galactic Radius	R_D
Gamma-ray Background Fit Parameter	$B^{(\gamma)}$
Gamma-ray Branon DM Fit Parameter	$C^{(\gamma)}$
Gamma-ray DM Signal Fit Parameter	$A^{(\gamma)}$
Hubble Parameter	H
Hubble Parameter Normalized	h
Mass of i-th Specie of Particle	m_i
Metric	$g_{\mu\nu}$
Lensing Angle	$\vec{\alpha}$
Light velocity	$c = 1$
Momentum of Particle i	$p_{\rho i}$
Monte Carlo Evaluation Variable	Q
Monte Carlo Emission Angle	θ_{MC}
Monte Carlo Relative Deviation	ΔMC
Neutrino Mixing Angle	$\alpha^{(\nu)}$
Neutrino Mixing Matrix	U
Neutrino Oscillation Length	L_ν
Neutrino Oscillation Probability Matrix	P
Neutrino Telescope Factor	$Af \equiv A_{\mathrm{eff}} \times t_{\mathrm{exp}}$
Number Density	$n_{\rho i}$

Number of Extra Dimensions	$\mathcal{N}_{\rm SUSY}$
Newton's Constant	G
Partons Energy Fraction	$z_{\rm MC}$
PYTHIA 6.4 Gamma-ray fluxes Parameters	a_1, $b_{1,2}$, $c_{1,2}$, $d_{1,2}$, j_1, $n_{1,2}$, p_1, q_1, l_1
Power-law Amplitude Gamma-ray	Φ_0
Power-law Amplitude Neutrino	A_ν^0
Power-law Spectral index Gamma-ray	Γ
Power-law Spectral Index Neutrino	B_ν^0
Planck scale	M_{Pl}
Pressure Density	p_C
Quantum Fundamental Gravity Scale in Extra Dimensions	$M_\star$
Relativistic Degrees of Freedom	$g_\star$
Ricci Tensor	$\mathrm{R}_{\alpha\beta}$
Ricci Scalar	R
Rotation velocity	v_ω
Scalar field	Π
Speed of Light	c
Solid Angle	Ω
Spatial Curvature	k_C
Spherical Harmonic Functions	$Y_{lm}\left(\theta,\phi\right)$
Spherical Harmonic Coefficients	a_{lm}
Strong Interaction Coupling Constant	α_s
Surface Density	$\Sigma(\xi)$
Target nuclei number	N_T
Temperature	T
Temperature at Freeze-out	T_f
Temperature at the Equilibrium	T_0
Thermally Averaged Cross-Section	$\langle\sigma v\rangle$
Transverse Momentum	p_T
(Missing) Transverse Momentum	$\not{p}_T$
ζ-Factor	ζ_a

Dedicated to my family and my friends,

to Napoli and Madrid,
and in memory of Davide...

Chapter 1

Introduction

The discovery of the nature of Dark Matter (DM) is a new frontier in the cosmology and particle physics of the XXI Century. In the last decades, many gravitational probes have shown the existence of a new kind of matter. Such a new component has escaped any type of detection as particle and also any theoretical description as modified gravity so far. Embarked on the caravel of indirect detection, *astroparticle physics* is a possible track to follow, in order to reach such new territory of physics, and explore it. This doctoral thesis is a travel journal on the route of this search. We will carry the reader on the indirect caravels not far from the direct and the theoretical ones. We are going to look at the ocean of standard cosmology and to follow a guiding star, towards its frontiers. That is a dark candle (possibly) made of a heavy matter at the Galactic Center.

In the Section 1.1 of the Introduction to this thesis, we will briefly present the history of the discoveries of the last centuries in astrophysics, astroparticle and cosmology, and focus on the history of the Universe in Section 1.2. The pillars of modern cosmology are introduced in Section 1.3, while in Section 1.4 we will present to the observational probes about the existence of DM. The prospective nature of DM as a particle is then introduced in Section 1.5. Finally, in Section 1.6 we will trace out the state of the art in the observational and theoretical aspects of the research in DM.

1.1 The Discovery Timeline.

Astroparticle physics was born in 1912, from the marriage between *particle physics* and *astrophysics*. The ceremony was celebrated by V. F. Hess in a balloon at altitudes of up 5 km. There, the terrestrial component of ionizing radiation met the extraterrestrial partner. In the same period, A. Einstein was celebrating the alliance between *space* and

time and their children were called *special* and *general relativity*. Casually, two different solar eclipses were testimonies of both events. One of the solar eclipses was 1919; it signed the first experimental probe of general relativity: the *gravitational lensing*.
In 1921, A. Einstein received the Nobel Prize not for the general relativity theory but for the quantum-mechanic interpretation of the photoelectric effect. In his Nobel Lecture discussed two years later, in 1923, he spoke about "Fundamental Ideas and Problems of the Theory of Relativity".
In 1929, E. Hubble observed the redshift of spectral lines, demonstrating that the Universe was expanding. The doors of *cosmology* had yet been opened. But at that time, the Nobel Prize in Physics did not recognize work done in astronomy. Hubble spent the latter part of his career attempting to have astronomy considered as an area of physics. Shortly after his death (1953), the Nobel Prize Committee decided that astronomical work would be eligible for the physics prize. However, the prize can not be awarded posthumously.
V. F. Hess was awarded with the Nobel Prize in 1936 *for his discovery of cosmic radiation*. In his Nobel Lecture he mentioned the other solar eclipse: *"... at the time of a nearly complete solar eclipse on the 12th April 1912,...was able to observe no reduction in ionization during the eclipse I decided that, essentially, the sun could not be the source of cosmic rays, at least as far as undeflected rays were concerned"* and *"....It is likely that further research into "showers" and "bursts" of the cosmic rays may possibly lead to the discovery of still more elementary particles, neutrinos and negative protons, of which the existence has been postulated by some theoretical physicists in recent years"*.
The Nobel Prize in Physics in the 1978 was divided in two half parts. One of them awarded A. Penzias and R. W. Wilson *for their discovery of cosmic microwave background radiation*, one of he pillars of the standard cosmological model.
The Nobel Prize of 2006 to John C. Mather and George F. Smoot *for their discovery of the blackbody form and anisotropy of the cosmic microwave background radiation*. Such a precise blackbody spectrum had never been observed before.
Recently, the 2011 Nobel Prize in cosmology was received by S. Perlmutter, B. P. Schmidt and A. G. Riess *for the discovery of the accelerating expansion of the Universe through observations of distant supernovae*. It was a pleasure for me listen to the Prof. Schmidt's talk at Universidad Autónoma de Madrid (Spain) a couple of years later.

Moreover, some others important discoveries allowed the development of the current generation of research in cosmology and particle and astroparticle physics.
We refer for example to 1958, when P. A. Cherenkov, I. M. Frank and I. Y. Tamm were awarded *for the discovery and the interpretation of the Cherenkov effect*, that allowed the construction of the current generation of Cherenkov telescopes for astroparticle research.

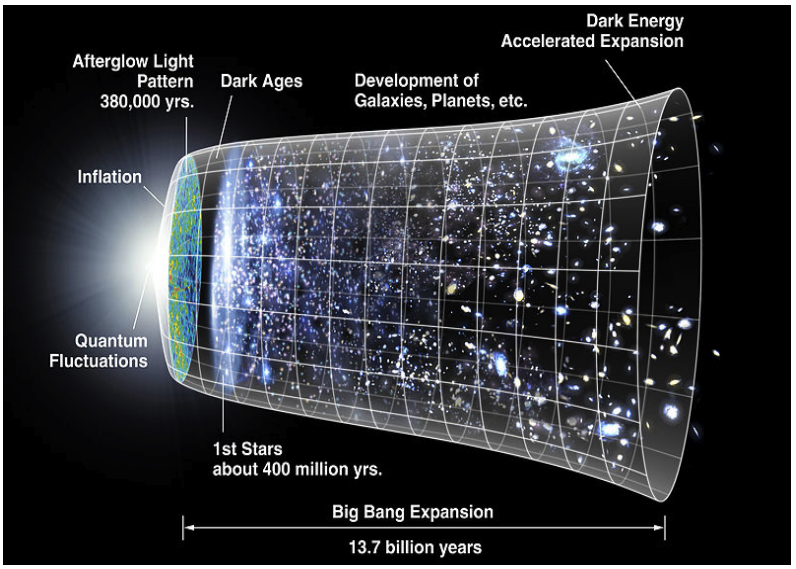

FIGURE 1.1: From NASA webpage [1]. Conceptual illustration of the Cosmological timeline.

The 1984 is marked by C. Rubbia and S. van der Meer *for their decisive contributions to the large project, which led to the discovery of the field particles W and Z, communicators of weak interaction.* This fact is also directly related with DM search.
The 1995 signed M. L. Perl *for the discovery of the tau lepton* and F. Reines *for the detection of the neutrino.* Nowadays, neutrino telescope represents a new eye to look at the sky.
The Nobel Prize in Physics 2013 was awarded to F. Englert and P. W. Higgs *for the theoretical discovery of a mechanism that contributes to our understanding of the origin of mass of subatomic particles, and which recently was confirmed through the discovery of the predicted fundamental particle, by the ATLAS and CMS experiments at CERN's Large Hadron Collider.*

1.2 The Cosmological Timeline

The Cosmological Timeline in Fig. 1.1 [1] flows in some sense backwards with respect to the Discovery Timeline.

Approximately 13 billion years ago the Universe began its expansion from a hot, dense state. It has been postulated that in the first 10^{-34} seconds it underwent a brief period of accelerated expansion, known as **inflation**. On the one hand, this period is related with the homogeneity and isotropy we see today, on the other, quantum mechanical fluctuations present during this process were imprinted as density fluctuations, which

later seeded the formation of structure.
After inflation, the early Universe was a soup of matter and energy, in which particle/antiparticle pairs were constantly creating and annihilating. As the Universe cooled, the different species decouple from the primordial plasma. When this process happens for a particular species of particle, that particle is said to have **frozen-out**. Throughout a process called baryogenesis, the asymmetry between matter and antimatter that we see today was produced.
During the first 10 minutes or so, various light elements such as deuterium, helium-3, helium-4, and lithium-7 were created by the combination of free protons and neutrons present after baryogenesis. This process of light-element formation is called Big Bang **nucleosynthesis**.
After about 10^5 years, the Universe finally cools to a few thousand Kelvin, cold enough for free nuclei and electrons to begin to combine into atoms. This process occurs during a time period called the era of recombination. Before recombination, the Universe was opaque to electromagnetic radiation. After the formation of atoms, the Universe becomes transparent. It becomes possible for light to travel large distances, across the visible Universe. The light released at this time is perceived today as the **Cosmic Microwave Background (CMB)**, the afterglow of the Big Bang's heat. By this time, **DM** (unaffected by the behavior of the baryonic matter) had already begun to collapse into halos.
Galaxies and stars began to form after a few hundred million years, when the baryonic gas and dust collapsed to the center of the pre-existing (Cold) DM halos.
Measurements of cosmic distances of galaxies through the use of supernovae type Ia (SNe Ia) as standard candles show the acceleration of the Universe expansion. This requires that the Universe should contain part of its energy density in a substance that goes under the name of dark energy.
Nowadays there is very strong observational evidence that the Universe is isotropic about the position occupied by the Earth. The distribution of different backgrounds like galaxies, radio sources and the CMB itself are pretty isotropic around our position on large scale. Such observed isotropy (rotation invariance about each point) and homogeneity (translation invariance) is in agreement with the assumptions of the **cosmological principle**.

Such **Standard Cosmological Model (SCM)** or **ΛCDM** (SCM with the dark contribution given by the cosmological constant Λ and the Cold-DM component) is based on Einstein's **General Relativity (GR)**, as we will illustrate in the next Section.

1.3 The Fundamentals of Cosmology

In the following section we will explain in detail the concepts introduced so far, the state of art and open questions of modern cosmology.

1.3.1 General Relativity

The cornerstone to include the effects of gravitation in his theory of special relativity is the *Equivalence Principle*: the gravitational and inertial masses entering respectively in the first (principium of inertia) and second Newton's law do not differ. This fact has been proved experimentally at the level of one part in 10^9. Einstein published the theory of GR in 1915 [2]. A consequence of such a principle is that the gravitational force as experienced locally while standing on a massive body is actually the same as the pseudo-force experienced by an observer in a non-inertial (accelerated) frame of reference. In an inertial frame of reference bodies and light obey Newton's first law, moving at constant velocity in straight lines. Analogously, in a curved spacetime the worldline of an free-falling particle or pulse of light is as straight as possible (in space and time). Such a worldline is called a geodesic. The fact that non-trivial metrics affect geodesics is completely independent of GR. The first GR contribution to such description is that gravitation can be described by a metric. Given a metric $g_{\alpha\beta}$, the geodesic equation is:

$$\frac{\mathrm{d}^2 x^\mu}{\mathrm{d}\lambda^2} = -\Gamma^\mu_{\alpha\beta}\frac{\mathrm{d}x^\alpha}{\mathrm{d}\lambda}\frac{\mathrm{d}x^\beta}{\mathrm{d}\lambda}. \tag{1.1}$$

where x^α are the space-time coordinates, λ the affine parameter and the affine connection components $\Gamma^\mu_{\alpha\beta}$ depend on the metric:

$$\Gamma^\mu_{\alpha\beta} = \frac{1}{2}g^{\mu\nu}\left(g_{\nu\alpha,\beta} + g_{\nu\beta,\alpha} - g_{\alpha\beta,\nu}\right). \tag{1.2}$$

The spatial part of Eq. (1.1) returns the path of a light ray, for example in gravitational lensing (Section 1.4). The second contribution is that the metric of the Universe is related to its constituents as matter and energy. This second part is contained in the Einstein's equations:

$$\mathrm{R}_{\alpha\beta} - \frac{1}{2}g_{\alpha\beta}R = 8\pi\mathrm{G}T_{\alpha\beta} + \Lambda g_{\alpha\beta}. \tag{1.3}$$

The geometry of space-time, described by the Ricci tensor $\mathrm{R}_{\alpha\beta}$, which depends on the metric $g_{\alpha\beta}$ and its derivatives as:

$$\mathrm{R}_{\alpha\beta} = \mathrm{R}^\lambda_{\alpha\lambda\beta} = \partial_\lambda\Gamma^\lambda_{\beta\alpha} - \partial_\beta\Gamma^\lambda_{\lambda\alpha} + \Gamma^\lambda_{\lambda\eta}\Gamma^\eta_{\beta\alpha} - \Gamma^\lambda_{\beta\eta}\Gamma^\eta_{\lambda\alpha} \tag{1.4}$$

The scalar curvature R (Ricci scalar, $R \equiv g^{\alpha\beta}\mathrm{R}_{\alpha\beta}$), is related to its source given by the energy-momentum tensor $T_{\alpha\beta}$ and the constant term Λ. G is the Newton's constant. The value of Λ is a debated point in cosmology. Firstly it was introduced to obtain the Einstein's static cosmological solution. After the discovery of the expansion of the Universe by E. Hubble and long theoretical efforts, Λ was removed from the equations. Finally, it reappeared later as a natural explanation of the present acceleration of the Universe [3]. Details on GR and its cosmological application may be found in [4].

1.3.2 The Cosmological Principle and Equations

The Cosmological Principle might be considered as the application on large scale of the *Copernican Principle*. Copernicus believed that the Sun, not the Earth was the center of the Universe. Later on, it was discovered that neither the Sun nor the Milky Way occupy a special place in the Universe. This means that the Earth do not occupy a special place in the Universe. Therefore, the isotropy we observe all around should be also seen from any position in the Universe, that is the Universe is homogeneous.
The best-known observational probe of the isotropy of the Universe is the CMB radiation (Section 1.4.3). The explanation of the radio noise of about 3K isotropically distributed was given by B. Dicke, P. Peebles, P. Roll and D. Wilkinson. Such discovery is also a cornerstone of the Big Bang Model. The existence of the CMB together with the expansion of the Universe discovered by E. Hubble and V. Slipher imply a hot early phase, which becomes hotter and denser as we go backwards in time. The Cosmological Principle is a pillar to apply the Einstein's equations (1.3) to describe the dynamic of the expanding Universe. The kinematic framework for cosmological models is the Friedman-Robertson-Walker (FRW) metric. In such a frame, the spatial coordinates are comoving and the expansion of the Universe itself appears as a change in the spatial components of the metric and not as a difference in the relative position of two points, for example two galaxies. The cosmological time coordinate is the elapsed time since the Big Bang according to a clock of a comoving observer and is a measure of cosmological time. Such a metric can be written as:

$$\mathrm{d}s^2 = \mathrm{d}t - a_C^2(t)\left[F(\mathrm{r})\mathrm{d}\mathrm{r}^2 + r^2\mathrm{d}\Omega^2\right] \tag{1.5}$$

with $\mathrm{d}\Omega^2 = \mathrm{d}\theta^2 + \sin^2\theta\mathrm{d}\phi^2$. The scale factor $a_C(\mathrm{t})$ describe the dynamic of the Universe. Applying the Cosmological Principle of translation (homogeneity) and rotation (isotropy) invariance, the function $F(\mathrm{r})$ is determined [4] as:

$$F(\mathrm{r}) = \frac{1}{1 - k_C \mathrm{r}^2} \tag{1.6}$$

Here, k_C depends on the spatial curvature: the Universe is open if $k_C = -1$, flat for $k_C = 0$ and close if $k_C = 1$.

Fixed the cosmological metric in a comoving frame, the cosmological equation are obtained from the Eq. (1.3) through the calculation of the affine connection and Ricci tensor and scalar in such a frame of reference and the energy conservation law for the energy-momentum tensor [4]. In such a way, we obtain the Cosmological Equations system:

$$\begin{aligned} \text{Energy conservation :} \quad & \frac{\partial \left(a_C^3 \epsilon_C\right)}{\partial t} + p_C \frac{\partial a_C^3}{\partial t} = 0 \\ \text{I field equation :} \quad & \left(\frac{\dot{a}_C}{a_C}\right)^2 + \frac{k_C}{a_C^2} = \frac{\Lambda}{3} + \frac{8\pi \mathrm{G}}{3}\epsilon_C \\ \text{II field equation :} \quad & \frac{\ddot{a}_C}{a_C} = \frac{\Lambda}{3} - \frac{4\pi \mathrm{G}}{3}\left(\epsilon_C + 3p_C\right) \end{aligned} \tag{1.7}$$

where ϵ_C and p_C are the energy and pressure density respectively measured by a comoving observer. The various species entering the cosmological model are assumed to satisfy linear equations of state as $p_C = w\epsilon_C$, with $w_\Lambda = -1$ for the cosmological constant, $w_M = 0$, for cold non relativistic matter and $w_R = 1/3$ for radiation component, that is photons in the CMB or ultrarelativistic plasma. Moreover, the density parameters for each species are defined as $\Omega_i = 8\pi \mathrm{G}\epsilon_i / 3H_0^2$, where $\epsilon_{cr} = 3H_0^2/8\pi \mathrm{G}$ is the critical density corresponding to the flat Universe ($k_C = 0$) and $H_0 = (\dot{a}_C/a_C)_0$ is the Hubble parameter today. With such assumption and the additional definition of the density parameters for the cosmological constant ($\Omega_\Lambda = \Lambda/3H_0^2$) and the curvature ($\Omega_{k_C} = -k_C/a_{C_0}^2 H_0^2$), the Friedman equation can be rewritten as:

$$\Omega_M + \Omega_R + \Omega_\Lambda + \Omega_{k_C} = 1. \tag{1.8}$$

The $\Omega_M = \sum_i \Omega_i$ is the sum of the different contributions from matter species filling the Universe, as baryons or non relativistic DM could be, and Ω_R is the radiation content. In Big Bang models, $\Omega_{k_C}(t) \to 0$ as $t \to 0$ and the Universe is nearly flat at early times. The observational constraints to such density parameters are given by observation of the CMB from satellites experiments such as the Cosmic Background Explorer (COBE), the Wilkinson Microwave Anisotropy Probe (WMAP) and the recent PLANCK surveyor. [5], as we will discuss in the Section 1.4.

1.3.3 The Matter Content Ω_M

After inflation, the Universe was made of a hot plasma of particles in thermal equilibrium. In the case of particle species that are in equilibrium through pair annihilation processes $1+2 \leftrightarrow 3+4$ the abundance of each species is described by the Boltzmann equation:

$$a_C^{-3}\frac{\mathrm{d}\left(n_{\rho 1}a_C^3\right)}{\mathrm{d}t} = n_{\rho 1}^{(0)} n_{\rho 2}^{(0)} \langle\sigma v\rangle \left\{\frac{n_{\rho 3}n_{\rho 4}}{n_{\rho 3}^{(0)} n_{\rho 4}^{(0)}} - \frac{n_{\rho 1}n_{\rho 2}}{n_{\rho 1}^{(0)} n_{\rho 2}^{(0)}}\right\}, \tag{1.9}$$

where a_C is the scale factor, $n_{\rho i}$ and $n_{\rho i}^{(0)}$ the number density of the $i-$th species and its value at equilibrium. Interactions are included in the right-hand side of the equation. We are supposing that annihilation is the only process affecting the abundance of these species. The thermally averaged cross-section is:

$$\begin{aligned}\langle\sigma v\rangle \equiv\ & \frac{1}{n_{\rho 1}^{(0)} n_{\rho 2}^{(0)}} \int \frac{\mathrm{d}^3 p_{\rho 1}}{(2\pi)^3\, 2E_{\rho 1}} \int \frac{\mathrm{d}^3 p_{\rho 2}}{(2\pi)^3\, 2E_{\rho 2}} \int \frac{\mathrm{d}^3 p_{\rho 3}}{(2\pi)^3\, 2E_{\rho 3}} \int \frac{\mathrm{d}^3 p_{\rho 4}}{(2\pi)^3\, 2E_{\rho 4}} e^{-(E_{\rho 1}+E_{\rho 2})/T} \\ & \times (2\pi)^4\, \delta^3\left(p_{\rho 1}+p_{\rho 2}-p_{\rho 3}-p_{\rho 4}\right) \delta\left(E_{\rho 1}+E_{\rho 2}-E_{\rho 3}-E_{\rho 4}\right) |\mathcal{M}|^2 ,\end{aligned} \tag{1.10}$$

where $p_{\rho i}$ and $E_{\rho i}$ are the momentum and the energy of the particles.The amplitude $\mathcal{M}$ is determined by the fundamental physics of the process in question. As the size of the Universe increases and the temperature decreases, the different species decouple from the thermal equilibrium. In general, a species decouples when the interaction rate $n_{\rho 1}^{(0)} \langle\sigma v\rangle$ of the particle becames smaller than the expansion rate of the Universe. In Eq. (1.9) we are assuming that the distribution of various species is the Bose-Einstein or Fermi-Dirac ones, because in the condition of kinetic equilibrium scattering happens very rapidly. With such an assumption, the number density of a massive species ($m_i >> T$) becomes exponentially suppressed $n_{\rho i} \sim (m_i T)^{3/2} e^{-m_i/T}$. That means, the number density falls to zero if the species does not freezes-out. If the interaction of the massive species freezes-out, that is the particle decouples, at a temperature comparable to its mass, the species can have a significant relic abundance today. Otherwise, for $m_i << T$ the particles are relativistic and the reactions proceeds rapidly so that $n_{\rho i} \sim T^3$. For the first second the Universe was so hot that atomic nuclei could not form. Space was filled with a hot soup of protons, neutrons, electrons and photons. When the Universe cooled off, these high-energy photons became rare enough that it became possible for deuterium to survive. These deuterium nuclei could keep sticking to more protons and neutrons, forming nuclei of helium-3, helium-4, lithium, and beryllium. Elements heavier than

helium were created later in the stars. This process of element-formation is called nucleosynthesis. There is only a small window of time in which nucleosynthesis can take place, and the relationship between the expansion rate of the Universe (related to the total radiation density Ω_R) and the density of protons and neutrons (the baryonic matter density Ω_B) determines how much of each of these light elements are formed in the early Universe. As the Universe expands, however, the density of protons and neutrons decreases and the process slows down. After a few minutes, therefore, the free unstable neutrons will decay and nucleosynthesis will stop. At the temperature of 1 MeV, the cosmic plasma consists of relativistic particles (photons, electrons and positrons), decoupled relativistic particles (neutrinos) and non relativistic particles (baryons). At the temperature of ~ 1 eV there is very little neutral hydrogen. In fact, the high photon/baryon ratio ensures that any hydrogen atom produced is instantaneously ionized. When the temperature drops far below the neutral hydrogen binding energy (13.6 eV), appreciable recombination take place. Recombination is directly tied to decoupling of photons from matter (CMB radiation). According to nucleosynthesis data and CMB analysis baryonic matter makes up $\sim 4\%$ of the critical cosmological density, corresponding to $\Omega_B h^2 \approx 0.02205 \pm 0.00028$ whit $H_0 = 100h\,\mathrm{km\,s^{-1}Mpc^{-1}}$. Only a small fraction, less than 10%, of the baryonic matter is condensed to visible stars, planets and other compact objects. Most of the baryonic matter is in the intergalactic matter, it is concentrated also in hot X-ray coronas of galaxies and clusters. The remaning part of the Universe matter contents is DM.

1.3.3.1 Dark Matter

Because of the aim of this thesis, we are particularly interested in the decoupling of DM particles. The purpose is to determine fundamental properties, such as the mass and the cross-section of this species, fixed the well-know relic abundance $\Omega_{DM}h^2 \approx 0.1199 \pm 0.0027$ as measured by PLANCK [9] and we will discuss in Section 1.4.
As for baryonic matter, depending on the DM mass at decoupling, we have non-relativistic (cold) DM for $m_{DM} >> T_f$, otherwise the DM particles are relativistic. The case of semi-relativistic DM correspond to $m_{DM} \approx T_f$. The non-relativistic case is favoured by standard theory of large-scale structures. In the cold DM model, structure grows hierarchically (bottom-up), with small objects collapsing under their self-gravity first and merging in a continuous hierarchy to form larger and more massive objects. In the hot DM paradigm, structure forms by fragmentation (top-down), with the largest superclusters forming first subsequently fragmenting into smaller pieces as galaxies. The predictions of the hot DM theory disagree with observations of large-scale structures,

whereas the cold DM paradigm is in general agreement with the observations [6]. However, several discrepancies between the predictions of the particle cold DM paradigm and observations of galaxies and their clustering have also arisen. Firstly, the cuspy halo problem: the density distributions of DM halos in cold DM simulations are much more peaked than what is observed in galaxies by investigating their rotation curves. Secondly, the missing satellites problem: cold DM simulations predict much larger numbers of small dwarf galaxies than are observed around galaxies like the Milky Way. Thirdly, the disk of satellites problem: dwarf galaxies around the Milky Way and Andromeda galaxies are observed to be orbiting in thin, planar structures whereas the simulations predict that they should be distributed randomly about their parent galaxies. Some solutions have been proposed for these problems, but it remains unclear whether they can be solved without abandoning the cold DM paradigm [7].
Depending on the annihilation rate, we get thermal or non-thermal DM. For large thermal cross-section, DM is in both kinetic and chemical equilibrium with the plasma before decoupling. In this case, the initial abundance is irrelevant for the final relic density as shown in Fig. 1.2. The latter depends only on the DM abundance at freeze-out. In the case of a not-full equilibrium the final abundance is determined by the annihilation rate as well as the initial abundance. If the initial abundance is small, the dominant production occurs at $m_{DM} \lesssim T$ and the relic abundance is freeze-in. In the freeze-out scenario the final abundance is inversely proportional to the annihilation rate, in the freeze-in case it is directly proportional [8]. In the case of small annihilation rate, DM particles are produced already decoupled from the thermal bath. In this case the no-thermal relic density does not depend on the thermal production but only on the initial abundance.

The Weakly Interacting Massive Particles (WIMPs) are the most plausible DM candidate so far (see Section 1.5). In the generic WIMP scenario, two heavy particles can annihilate producing two lighter particle $\mathrm{DM}\,\mathrm{DM} \to P\bar{P}$. The light particles are assumed to be in equilibrium with the cosmic plasma, with $n_{\rho P} = n^{(0)}_{\rho P}$. In such a scenario, the only unknown variable in the Boltzmann equation 1.9 is the WIMP's number density $n_{\rho\mathrm{DM}}$:

$$a_C^{-3}\frac{\mathrm{d}\left(n_{\rho\mathrm{DM}}a_C^3\right)}{\mathrm{d}t} = \langle\sigma v\rangle\left\{\left(n^{(0)}_{\rho\mathrm{DM}}\right)^2 - n^2_{\rho\mathrm{DM}}\right\}, \tag{1.11}$$

To determine the present-day abundance of DM relics, we need to solve the previous equation (1.11). The DM energy density ϵ_{DM} at the freeze-out is proportional to the ratio between the DM mass and temperature at freeze-out (m_{DM}/T_f), the temperature of the plasma at equilibrium T_0 and is inversely proportional to the value of the annihilation cross-section $\langle\sigma v\rangle$ (particles with larger cross-section freeze-out later) and decreases with the Universe expansion $\sim a_C^{-3}$ [4]:

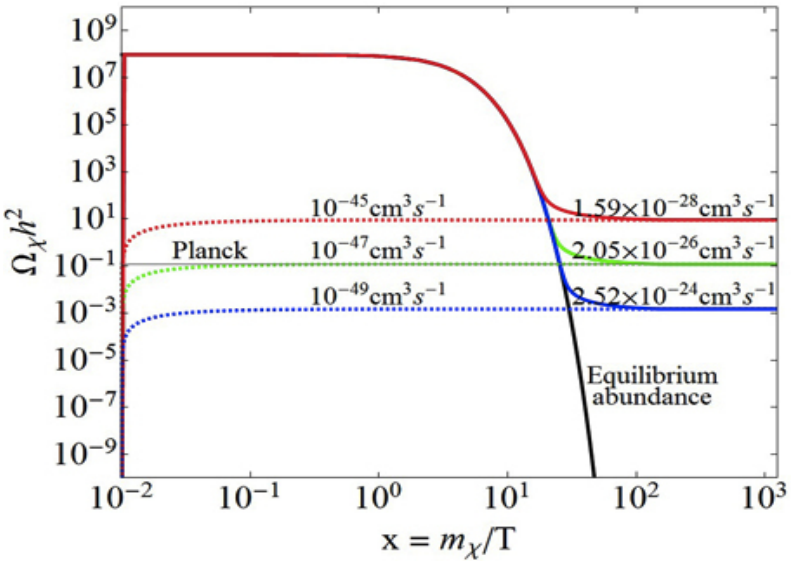

FIGURE 1.2: From P. S. B. Dev, A. Mazumbar, S. Qutub [8]. Here, $\Omega_\chi \equiv \Omega_{\rm DM}$ and $m_\chi \equiv m_{\rm DM}$. The picture show the DM relic density in the both freeze-out (full lines) and freeze-in (dotted lines) scenario. As we explain in the text, in the former the relic abundance depends on the species density at the freeze-out temperature, while in the latter only depend on the initial abundance.

$$\epsilon_{\rm DM} \approx \frac{H(m_{\rm DM}) m_{\rm DM} T_0^3 / T_f}{m_{\rm DM}^2 \langle \sigma v \rangle} \tag{1.12}$$

where the Hubble expansion rate $H(m_{\rm DM})$ at the temperature $T = m_{\rm DM}$ depend on the effective number of relativistic degrees of freedom $g_\star(m_{\rm DM})$, that is a function of the DM mass. The estimation of the fraction of critical density today contributed by DM is $\Omega_{DM} \approx 10^{-26}{\rm cm^3 s^{-1}} / \langle \sigma v \rangle$ [9]. This is the value expected for $T_f \sim 100$ GeV. At such temperatures, $g_\star(m_{\rm DM}) \sim 100$ because of the contribution from all the particles of the SM (quarks, leptons, photons, gluons, weak bosons and Higgs) while $m_{\rm DM}/T_f \sim 20$. The typical value of the annihilation cross section required to get $\Omega_{\rm DM} \approx 0.31$ is then upon $\langle \sigma v \rangle \approx 10^{-3} {\rm G_F}$, where $\rm G_F$ is the Fermi's constant, related to the weak interactions. This fact is called the *WIMP's miracle*.

1.3.4 Inflation

Despite the numerous achievements of the SCM, such a description of the evolution of the Universe presents some inconsistencies. The first one is the *horizon* problem: the CMB radiation is isotropic even for angular scales corresponding to regions that were not causually connected at decoupling time. The second is the *flatness* of the Universe: the solutions of the Einstein's equations with $k_C = 0$ are unstable and therefore the curvature of the Universe today requires a very fine adjustment of the initial conditions. The third

problem is the *structure formation*: the existence of large scale structures in the Universe as galaxies and galaxy clusters can be explained as amplification of primordial density perturbations, but the SCM does not provide a mechanism for generating such initial perturbations. In 1980, A. Guth realized that such inconsistencies could be resolved hypothesizing a phase of exponential expansion in the primordial Universe [10]. Such a theory solves the horizon problem because the inflation could enlarge the causally connected region. The flatness would be reached during the inflation period itself and the large scale structures should been originated from primordial quantum fluctuation that stretched to larger scales.

1.4 Dark Matter evidence

The existence of DM is hypothesized because of discrepancies between the mass of large astronomical objects determined from their gravitational effects and the mass calculated from the luminous matter. While examining the Coma galaxy cluster in 1933, F. Zwicky was the first to use the virial theorem to infer the existence of unseen matter, which he referred to as non-luminous matter. He calculated the gravitational mass of the galaxies within the cluster and obtained a value at least 400 times greater than expected from their luminosity, which means that most of the matter must be dark [11]. Such discrepancy is evident also in rotational curves of spiral galaxies and in gravitational lensing effects as observed in the Bullet Cluster (see Section 1.4.2). Moreover, observational data of satellite experiments such as COBE, WMAP and PLANCK are well reproduced by a SCM that accounts for the 26.8% of DM of the total amount of mass-energy in the Universe [9].

1.4.1 Galactic Rotation Curves

The Galaxy rotation curve problem represents one of the first probes of the existence of DM. At large distances from the Galactic Center (GC) the gravitational potential should be that produced by a central point mass and, in the absence of forces other than gravitation, it should be expected that $GM/r^2 = v_\omega^2/r$ (G, universal gravitation constant; M, galactic mass; r, galactocentric radius; v_ω, rotation velocity), therefore $v_\omega \propto r^{-1/2}$. As shown in Fig. 1.3, the Keplerian decline was not observed, but rather, flat rotation curves with v_ω=cte were obtained [12]. The DM hypothesis interprets this result in the sense that the Keplerian regime holds at much greater distances than those at which we obtain observations. There should be a large amount of DM extending far beyond the visible matter in a more or less spherically symmetric DM halo. If

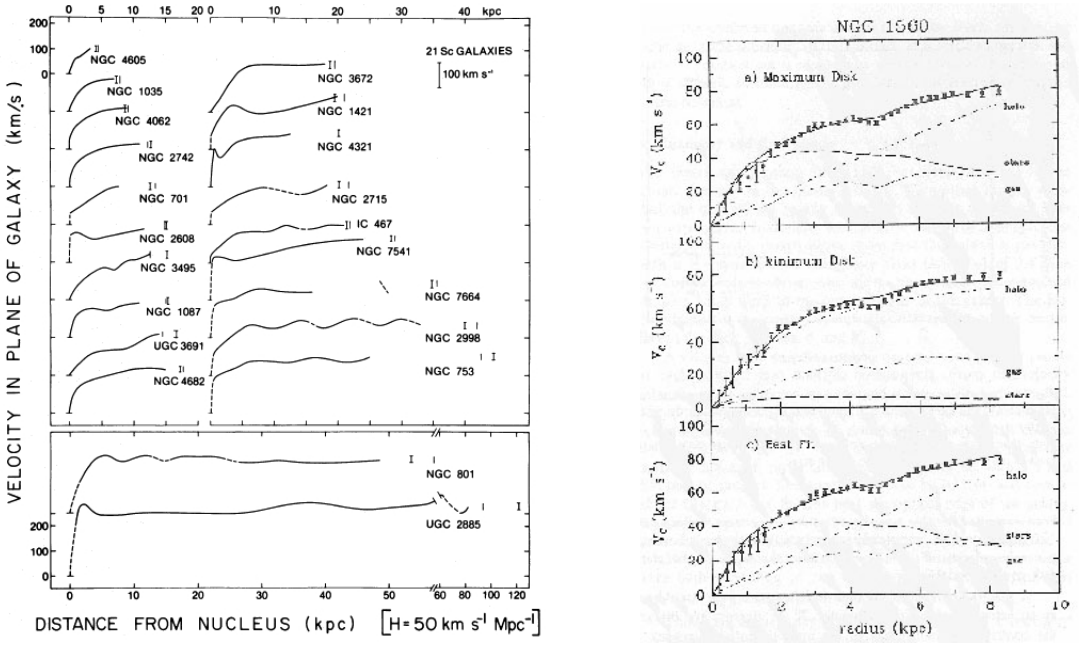

FIGURE 1.3: *(Left–panel)* From: V.C. Rubin, W.K. Ford and N. Thonnard [12]. The observations of the almost flat rotation curve in several spiral galaxy was one of the first motivation to hypothesize the existence of DM. *(Right–panel)* From: A. H. Broeils [12]. Here, $V_c = v_\omega$The observed rotation curve with different disk-halo models.The dotted and dashed lines indicate the gas and stellar disks. The dot-dashed line shows the rotational velocities of the halo; the full line is the contribution of all the components.

its distribution is spherically symmetric, the mass interior to a sphere of radius $r_{\rm sphere}$ would be $M(r_{\rm sphere}) \propto r_{\rm sphere}$, so that we obtain a first rough model of DM density distribution: $\rho(r) = (1/4\pi r^2)dM/dr = v_\omega/4\pi G r^2$, i.e. $\rho(r) \propto r^{-2}$, for distances far beyond the visible radius. This model is obviously over simplified. Detailed models have been proposed so far. Cored profiles, such as Isothermal or Burkert profile are motivated by the observations of galactic rotation curves, but are in conflict with the results of numerical N-body simulations that suggest the Navarro-Frank-White (NFW) or Einasto profile as the better choice [13]. A very recent work also demonstrated the presence of DM in the inner part of the Milky Way, including the solar system [14].

The NFW profile, peaked as r^{-1} at the GC, is a traditional benchmark choice for the DM density distribution on the Milky Way, while the Einasto profile better describes DM distribution in some dwarf spheroidal galaxies (dSphs). Their formal expressions are:

$$\begin{aligned} \rho_{\rm NFW}(r) &= \frac{A_s}{r(r+r_s)^2} \\ \rho_{\rm Einasto}(r) &= \rho_s \exp\left\{-2n\left[\left(\frac{r}{r_s}\right)^{1/n} - 1\right]\right\} \end{aligned} \tag{1.13}$$

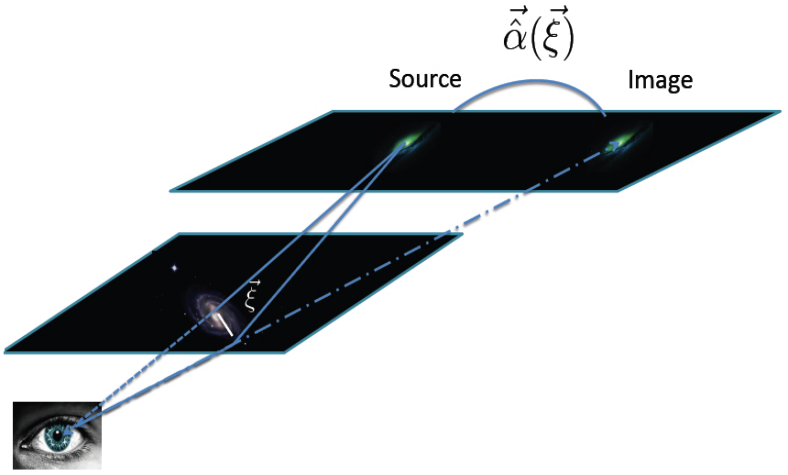

FIGURE 1.4: A light ray passes through the lens plane, it is deflected by an angle $\vec{\hat{\alpha}}(\vec{\xi})$ proportional to the lens mass. $\vec{\xi}$ is a 2-dimensional vector in the lens plane.

where A_s is the overall normalization, r_s the scale radius, ρ_s a constant density and n_s is the Einasto index.
Recently, N-body simulations that try to include the effects of baryons on DM distribution have found modified profiles that are steeper in the center with respect to the DM only simulations [15], as we discuss in the Section 2.3.

1.4.2 The Gravitational Lensing

On larger scales, DM affects gravitational lensing observations. As we underline in the timeline of the main cosmological discoveries, the light deflection was the first experimental proof of Einstein's GR Theory. The gravitational field of a massive object will extend far into space, and cause light rays passing close to that object (and thus through its gravitational field) to be bent and refocused somewhere else. Gravitational lensing happens on all scales. The more massive the object, the stronger its gravitational field and hence the greater the bending of light rays. The gravitational field of galaxies and clusters of galaxies can lens light, but so can smaller objects such as stars and planets. The kind of lensing that cosmologists are interested in is on the large scales of galaxies and clusters of galaxies. Light rays coming from more distant galaxies that passe close to a cluster may be distorted by its mass. It is the DM in the cluster that does almost all of the lensing. The effects can be very strong and very strange; the images of the distant, lensed galaxies (usually elliptical or spiral shaped) are stretched and pulled into arcs as the light passes close to the foreground cluster. The effects in the image depends on the lens, its mass and the position of the source with respect to the observer and the lens itself. Without entering into the formalism of gravitational lensing, we would just

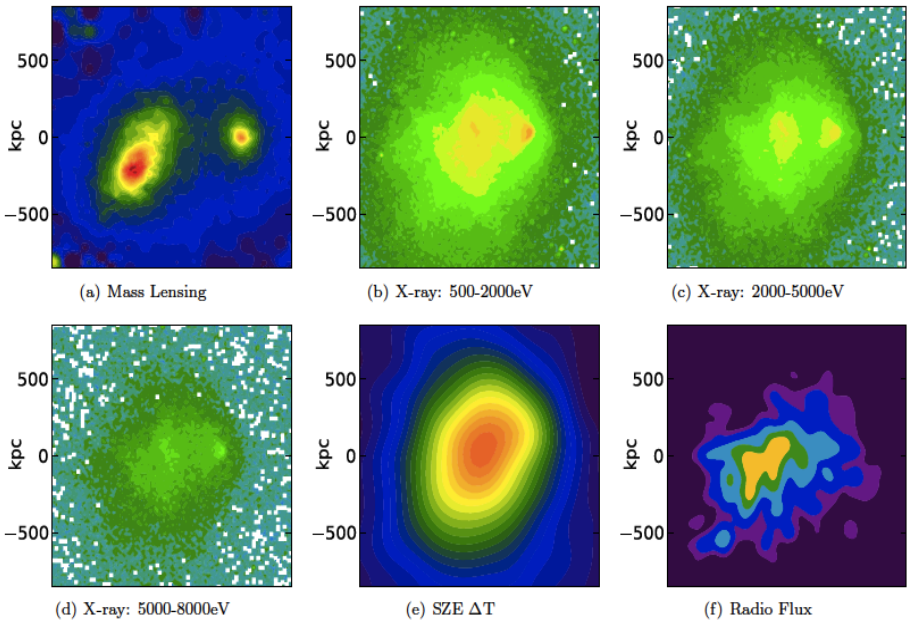

FIGURE 1.5: From C. Lage and G. Farrar [16]. Six observational data set of the Bullet Cluster. The mass distribution calculated with the gravitational lensing (figure (a)) does not match the luminous matter distribution showed in the other figures.

point out that for lensing analyses we are interested in the spatial part of the geodesic equation (1.1) to solve the path of the light ray. As illustrated in Fig. 1.4 the light ray emitted from a distant source is distorted as it passes an overdense region. At all times, the position of the ray can be characterized by a 2D vector specifying its angular distance from the center of the lens. In the first thin lens approximation the deflection of the light ray is proportional to the lens mass:

$$\hat{\alpha}\left(\xi\right) = \frac{4\mathrm{G}M\left(\xi\right)}{\xi} \tag{1.14}$$

where $M\left(\xi\right)$ is the mass embedded in the radius ξ

$$M\left(\xi\right) = 2\pi \int_0^{\xi} \Sigma\left(\xi'\right) \xi' \mathrm{d}\xi' \tag{1.15}$$

with the surface density $\Sigma\left(\xi'\right)$ given by the projection on the 2D lens plane of the 3-dimensional mass density distribution of the lens itself:

$$\Sigma\left(\xi\right)\xi = \int \rho\left(\vec{\xi}, z\right) \mathrm{d}z \tag{1.16}$$

where z is the direction along the line of sight. The strong gravitational lensing causes dramatic distortions as multiple images, arcs and rings. The weak lensing effect produces small but statistically coherent distortions of the background sources. When multiple images can not been resolved, we have micro lensing effects.

The best-known system with which to test the DM hypothesis is the Bullet Cluster (1ES 0657-558), where both strong and weak lensing effects are observed [16]. The gravitational lensing analysis shows that the most part of the mass of the system is actually distributed in two interacting galaxy clusters, that are not detectable as luminous matter (Fig. 1.5). The hot gas in this collision was slowed by a drag force, similar to air resistance. In contrast, the DM was not slowed by the impact, because it does not interact directly with itself or the gas except through gravity. This produced the separation of the dark and normal matter seen in the data. If hot gas was the most massive component in the clusters, as proposed by alternative gravity theories [17], such a separation would not have been seen. Instead, DM is required.

1.4.3 The Cosmic Microwave Background

As we introduced in the Section 1.3, the existence of the CMB and the expansion of the Universe imply a hot early phase, which becomes hotter and denser as we go backwards in time. In this epoch, the Universe is a plasma containing more and more species of particles as we go backwards in time and new channels are opened for pair production to the increasingly energetic photons. In this way, when the photons are cold enough, the baryons and electrons recombine to form neutral hydrogen and helium atoms, and the photons are free to propagate: the Universe become transparent. The CMB is the footprint of the last scattering surface, beyond (looking backward in time) which the Universe becomes optically thick. The first measurement developed by COBE reveal that the CMB corresponds to a blackbody radiation at $T_{\rm CMB} = 2.725 \pm 0.001$K [5]. After that, improved experiments such as WMAP and PLANCK showed that in different directions the black body temperature exhibits small deviations from $T_{\rm CMB}$. The anisotropy depends on the cosmological parameters and on the model of inflation. Such variations of the blackbody temperature depend on the angular scale, as showed in Fig. 1.6 [18]. Such a picture is the result of a spherical harmonics expansion of the temperature fluctuations:

$$T(\theta,\phi) = \sum_{lm} a_{lm} Y_{lm}(\theta,\phi)\,. \tag{1.17}$$

Such an expansion introduces the dependence on the two angles of the observed sphere θ, ϕ: $\theta \propto 180°/l$, so that $l = 100 \rightarrow \theta \approx 2°$ degrees of sky.

The position and height of each peak in Fig. 1.6 is determined by a particular combination of cosmological density parameter $\Omega_{i,k_C,\Lambda}$, defined in Section 1.3.2. The monopole term is the blackbody temperature. The dipole term is associated with the Doppler

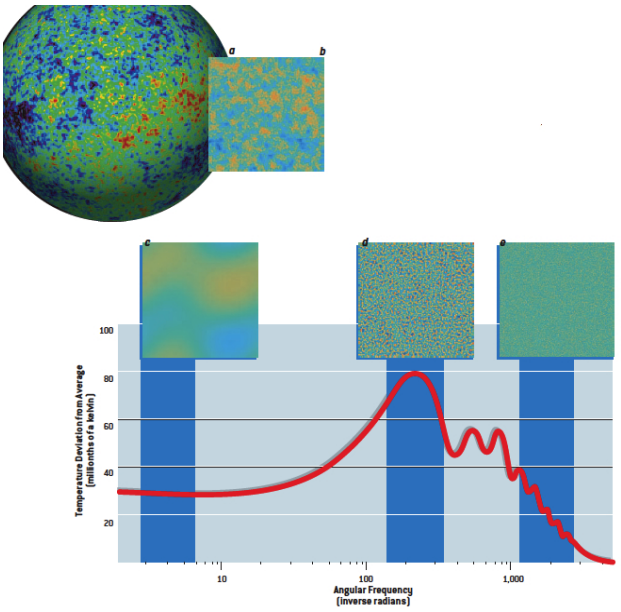

FIGURE 1.6: From W. Hu and M. White [18]. Representation of the CMB power spectrum. The 3K blackbody spectra is actually a more complicated figure. Multipole terms are associated with different angular scales. The comparison on the first three peaks gives an estimation of matter contents of the Universe (see text).

shift of 3.346 ± 0.017mK introduced by the Solar system motion relative to the CMB. The almost scale invariant spectrum of density perturbation at $l \leq 100$ is associated to angular scales bigger than the Hubble radius at decoupling. The existence of such a Sachs-Wolfe plateau is a generic prediction of the inflation. The information on the Universe contents is associated with $100 < l \leq 1000$. The position of the first acoustic peak at $l \simeq 220$ results in a flat Universe with $\Omega_{k_C} = 0.0001^{+0.0054}_{-0.0052}$. The comparison of the relative height of the firsts three peaks gives an estimation of the baryonic and DM content of the Universe. The second peak not so high as the first one because the baryons feel the radiation pressure, while DM does not. Recent data from PLANCK [9] set $\Omega_M = 0.315 \pm 0.017$. Of such 31% of matter contents, the 26% is DM while just the 5% is baryonic matter. The missing 69% is dark energy. The harmonic expansion of order $l > 1000$ corresponds to angular scales smaller than $5'$ of arc and shows damping tail due to baryon diffusion effects.

1.5 Dark Matter candidates

Despite the gravitational evidence of the existence of DM, there is still no consensus on what it is composed of, as we introduced in the previous section. The properties of large scale structures observed in our Universe imply that DM is fairly cold and its particles are relatively slow-moving. If DM were composed of relativistic particles as neutrinos, it would not clump under its own gravity on small scales, as predicted in the

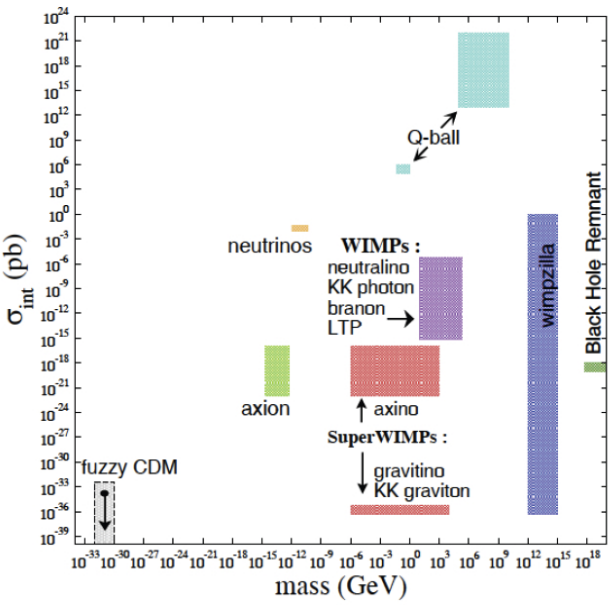

FIGURE 1.7: From S. Gardner and G. Fuller [19]. Summary of the DM particle zoo candidate. Each model cover a different area of the $\sigma - m_{\rm DM}$ parameter space.

structure formation model. It turns out that a massive cold stable particle interacting via the weak force will leave just about the right amount of remnants to account for the observed DM density.

Specific WIMP theories include Supersymmetry and Extra dimensions. Another DM candidate is the Axion. Though axions are far lighter than WIMPs (often 1 eV or much less), they can be created in the right amount by a non-thermal process which also naturally leaves them slow-moving. In addition to the candidates above, many other particles have been suggested, such as WIMPzillas, Q-balls, gravitinos, etc. In most of the cases, this DM appears in models that are motivated by other problems in physics. As shown in Fig. 1.7, each DM candidate covers an allowed range of masses and cross-sections that needs to be compared with observations [19]. In this section we will introduce the details of some candidates of particular interest for this thesis.

1.5.1 Supersymmetry, Extra-dimensions, Axions.

So far the most popular DM candidate can be found in Supersymmetric models. Supersymmetry (SUSY) predicts that each particle in the SM has a heavier ($\mathcal{N}_{\rm SUSY} = 1$ supersymmetry) SUSY partner of different spin but similar interactions. It can improve the hierarchy problem, making the weak scale stable under electroweak radiative corrections in a natural manner and consistent with precision electroweak measurements, while provide all the ingredients needed for successful electroweak baryogenesis. At the same time, it provides a suitable candidate for DM and allow gauge coupling unification

to occur at very high energy scale.

The Minimally Supersymmetric Standard Model (MSSM) [20] is one of the most popular among others. In this model, baryon number and lepton number are no longer conserved by all of the renormalizable couplings in the theory. R-parity forbids these couplings. All Standard Model particles have R-parity of +1 while supersymmetric particles have R-parity of −1. While the constraints on single couplings are reasonably strong, if multiple couplings are combined together, they lead to proton decay. With R-parity being preserved, the Lightest Supersymmetric Particle (LSP) cannot decay. Typically the LSP as DM candidate of the MSSM is an admixture of the electroweak gauginos and Higgsinos and is called a neutralino. In extensions to the MSSM, it is possible to have a sneutrino be the DM candidate. Another possibility is the gravitino, which only interacts via gravitational interactions and does not require strict R-parity [21]. The MSSM could solve many problems in cosmology and particle physics [20] and it is able to generate electroweak symmetry breaking radiatively, in contrast to the SM in which it is put ad hoc. The unconstrained MSSM has more than 100 parameters in addition to the SM parameters. This makes any phenomenological analysis impractical. Nevertheless, in the phenomenological MSSM (pMSSM) the additional parameters are reduced to 19. The pMSSM is designed taking into account that no new source of CP-violation and no flavour changing neutral currents have been observed in low-energy observables and direct searches (Section 2.2).

Despite the successes of SUSY, alternative models for physics beyond the SM may solve the hierarchy problem and the DM puzzle in the WIMP framework. Among others, physics in extra-dimensions is a possibility. Extra-dimension theories suggest that our Universe may have more spatial dimensions than the three we are familiar with. In the Universal Extra-Dimensions (UED) scenario, all the fields of the SM are allowed to probe the extra dimensions. In this model, there is a conserved quantum number known as KK-parity, under which all the odd-numbered KK modes are charged. KK-parity is analogous to R-parity in supersymmetric models. The conservation of KK-parity has the consequence that KK particles can only be produced in pairs, and hence, experimental constraints are reduced. In the Kaluza-Klein theory [22] every multidimensional field corresponds to a tower of four-dimensional particles with increasing masses. At low energies, only the lightest particles ($E < 1/\mathrm{D}_{ex-d}$) can be produced, whereas at $E \sim 1/D_{ex-d}$ extra-dimensions will show up. Here, D_{ex-d} is the dimension of the D^n_{ex-d} volume in which n extra-dimensions are compactified. Such a volume dilutes the strength of gravity from the fundamental scale $M_\star$ to the Planck scale $\mathrm{M}^2_{Pl} = \mathrm{M}^{2+n}_\star \mathrm{D}^n_{ex-d}$. The Lightest Kaluza-Klein Particle (LKP) is often stable if KK-parity is conserved. The allowed range of masses for the LKP (KK photon) and LSP (neutralino) is between tens of GeV and few TeV [23]. If the extra-dimension model contains branes, their fluctuation called *branon* are also a new particle for the effective four-dimensional phenomenology.

In the next Section, we will describe in more detail branons as DM candidates, referring to the bibilography for a detailed discussion of other WIMPs [19–23].

Nevertheless, non-WIMPs are also DM candidates, of which axions are an example. Axions arise from attempts to explain why the strong interaction seems to obey the CP symmetry. Among other things, CP symmetry would prevent the neutron from having a large electric dipole moment, otherwise it should has yet been detected. The best explanation for this strong CP problem predicts a new light neutral particle called the axion. The axion has a much longer time life than the age of the Universe in many theories, and can also be produced in the early Universe. However, axions represents a too low-mass DM candidates for the aim of this thesis. Because of that, we will not discuss this candidate in detail.

1.5.2 Brane World Theory

In the framework of extra-dimensions, branon is a natural DM candidate also at the TeV scale. It has been found that massive brane fluctuations (branons) are interesting candidates for DM in brane-world models with low tension [24]. From the point of view of the 4-dimensional effective phenomenology, massive branons are new pseudo-scalar fields which can be understood as the pseudo-Goldstone bosons corresponding to the spontaneous breaking of translational invariance in the bulk space produced by the presence of the brane [25, 26]. They are prevented from decaying into SM particles by parity invariance on the brane. The SM-branon low-energy effective Lagrangian [25, 26] can be written as

$$\mathcal{L}_{Br} = \frac{1}{2} g^{\mu\nu} \partial_\mu \pi^\alpha \partial_\nu \pi^\alpha - \frac{1}{2} m_{\mathrm{DM}}^2 \pi^\alpha \pi^\alpha + \frac{1}{8f^4} \left(4 \partial_\mu \pi^\alpha \partial_\nu \pi^\alpha - m_{\mathrm{DM}}^2 \pi^\alpha \pi^\alpha g_{\mu\nu} \right) T^{\mu\nu} \quad (1.18)$$

where $\alpha = 1 \ldots N$, with N the number of branon species.

One can see in Eq. (1.18) that branons interact by pairs with the SM energy-momentum tensor $T^{\mu\nu}$ and that the coupling is suppressed by the brane tension f^4. Limits on the model parameter from tree-level processes in colliders are given in Fig. 1.8 by present restrictions coming from HERA, Tevatron, LEP-II and LHC [27], but also prospects for future colliders such as ILC or CLIC can be found in [26–30]. Additional bounds from astrophysics and cosmology were obtained in [24].

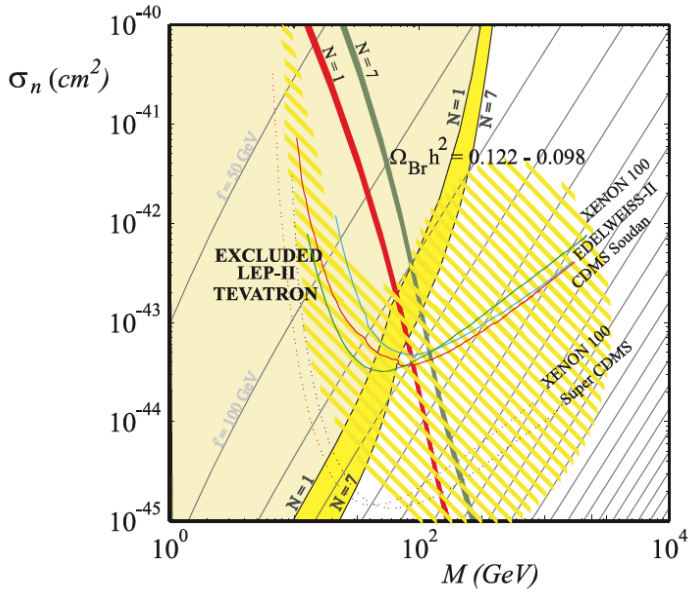

FIGURE 1.8: From J. A. R. Cembranos, J. L. Diaz-Cruz, L. Prado [27]. Constraints on Brane-World DM from TEVATRON and LEP.

1.6 State of the art: models and observations

Several decades after the first hypothesis about the existence of DM by Zwicky in 1933 and V. Rubin in 1980, such dark component remains still undiscovered. Although the possible existence of DM rises from astrophysical evidences such as the galactic rotation curves and the gravitational lensing, the need for new physics is also motivated at microscopic scales. Physics beyond the SM of particle, such as supersymmetry or extra-dimensions have been developed in order to solve problems at these small scales. Interestingly, they also provide new candidates for this new kind of matter. In spite of numerous efforts, no conclusive results have been obtained so far about the nature of DM. A natural candidate is a WIMP which is expected to have non-vanishing annihilation and interaction cross-sections with SM particles. As we will discuss in next Chapter, the experimental possibility of detecting such interactions completes the effort of searching for a DM footprint.

Chapter 2

Searching for Dark Matter.

In spite of the numerous gravitational probes and theoretical models discussed in the previous sections, a conclusive identification of the dark component of matter has not yet been found. Although there are many plausible origins for this component [31], DM is usually assumed to be in the form of thermal relics that naturally freeze-out with the right abundance in many extensions of the SM of particles [32]. In order to confirm its nature, DM searches have followed different directions. On the one hand, DM particles can be produced in laboratory experiments such as high-energy particle colliders [33]. On the other hand, local DM can be detected in a direct or indirect way [34–40]. As illustrated in Fig. 2.1, each direction of investigation addresses to a different kind of way to explore the interaction between DM and SM particles. In colliders DM particles should be generated through the interaction of two SM particles SM SM $\rightarrow$ DM DM with cross-section $\sigma_{\text{SM-SM}}$ (Section 2.1). The direct search focuses on the non-zero coupling of DM particles with heavy nuclei $\sigma_{\text{DM-SM}}$ in the process DM SM $\rightarrow$ DM SM (Section 2.2). Finally, the indirect search allows to set constraints on the annihilation cross-section between two DM particles $\sigma_{\text{DM-DM}}$ (as during the freeze-out epoch) to produce SM particles DM DM $\rightarrow$ SM SM (Section 2.3).

2.1 Searches at Colliders

To understand the nature of DM as a particle it is necessary to determine the interaction to the rest of known particles. Colliders are fundamental tool in this respect. The simplest way to assure that DM particles are stable over the lifetime of the Universe is to assume that they carry a new conserved quantum number that is not shared by the SM particles. As we discussed in the Introduction, DM models typically consider a DM particles of mass of $\sim$ 100 GeV in thermal equilibrium in the early stage of the Universe.

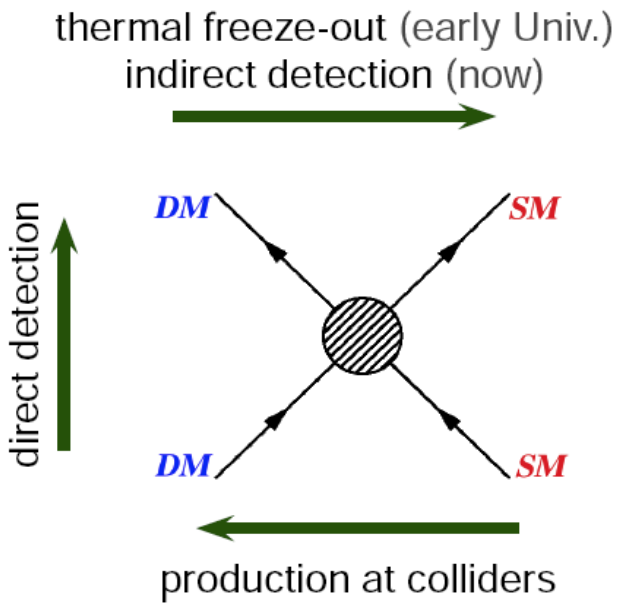

FIGURE 2.1: DM detection [40]. Direct detection address the annihilation (or decay) rate of DM particles in astrophysical or primordial sources. The inverse process of DM production is investigated in underground colliders experiment, while the DM scattering with SM-nuclei is object of the direct sector.

Therefore, on one hand, the annihilation cross section $\sigma_{\text{DM-DM}}$ needs to be compatible with the relic abundance Ω_{DM}. The DM mass and the annihilation cross section allow to estimate the DM pair-production cross section $\sigma_{\text{DM-SM}}$ in colliders. The majority of DM searches at colliders is related with supersymmetric models. In these models, the DM particle is only the lightest in a complete spectrum of new particles with the conserved discrete quantum number. The pair-production of particles with QCD colour has a large cross-section and the heavy coloured particles then decay down throughout the new particle spectrum, emitting quarks and leptons with a large transverse momenta p_T and a missing transverse momentum $\not{p}_T$ carried away by the unobserved lightest particle, the DM. In this technique the problem is the estimation of the background of heavy SM particles as W, Z and t in association with a number of jets from QCD radiation. In order to get an estimate of the DM mass, the sum of $\not{p}_T$ and highest-p_T jets gives a distribution m_{eff}

$$m_{\text{eff}} = \not{p}_T + \sum_i p_{T_i} \tag{2.1}$$

that peaks at the position correlated with the mass difference between the mass of the primary coloured particle and the DM mass $m_{\text{eff}} \approx 2\,(m_P - m_{\text{DM}})$. Indeed, the search at colliders depends on the masses of the primary particles produced. Depending on the model parameters the spectrum of SUSY particles can extend up to masses of 1 TeV and above. Unfortunately, it is unlikely that masses and couplings of such particles

could be measured with the same accuracy as for particles of lower masses, and some of these particles may not be visible at all at the next generation of colliders [23]. As we will discuss later, this fact represents an important limitation for the direction of investigation of this thesis. So far the Large Hadronic Collider (LHC) [41] put the strongest limit on lower DM masses. In 2012 the ATLAS and CMS experiments at the LHC at CERN have claimed the discovery of the Higgs mechanism, contributing to the understanding of the origin of the mass of subatomic particles [42]. So far, such Higgs boson has the properties of a SM particle. The present run of the LHC, started in the spring of 2015, will investigate deviations from the SM predictions and search for heavier Higgs bosons. The measurements of the Higgs boson coupling to the top quark and to the muon may reveal some substructure inside this Higgs boson, or provide some other evidence for physics beyond the SM.

2.2 Direct Detection

Weakly interacting DM candidates are predicted to have non-zero coupling with baryons generically and may be discovered through searches for nuclear recoil events in DM-nucleus scattering. For each event, the relative phonon, scintillations and ionization signals (or a combination of them) need to be discriminated from background events. Direct detection experiments usually operate in deep underground laboratories to reduce the background from cosmic rays. The majority of present experiments use one of three detector technologies: cryogenic detectors, such as CDMS, CRESST, EDELWEISS, EURECA, operating at temperatures below 100mK, detect the heat (phonons) produced when a particle hits an atom in a crystal absorber such as germanium. Noble liquid detectors detect the flash of scintillation light produced by a particle collision in liquid xenon or argon. Noble liquid experiments include ZEPLIN, XENON, DEAP, ArDM, WARP, DarkSide, PandaX, and the Large Underground Xenon (LUX) detector [43]. Finally, ionization channel is also used for discrimination. Among others, the CoGeNT experiment uses high-purity germanium crystal cooled to liquid nitrogen temperatures in its measurements, with a very low energy threshold (~ 0.5 keV). Such kind of DM detection depends on: the DM model, via the assumed DM-Nucleon cross-section $\sigma_{(DM-N)}$; the DM density distribution in the Galaxy, via the number density $\rho_{\odot}$, its velocity $\vec{v}$ and velocity distribution $f(\vec{v})$ at the solar system frame; finally, on the instrumental limitation via the nuclear response to the particular interaction [19, 43]. Recently, model independent analysis have been developed via elastic DM-nucleon scattering in frameworks of effective field theory. These theories are of great interest because they allow to identify a full set of operators that describe the potential interactions of DM particles, and relate them to nuclear response functions allowing to extract more information

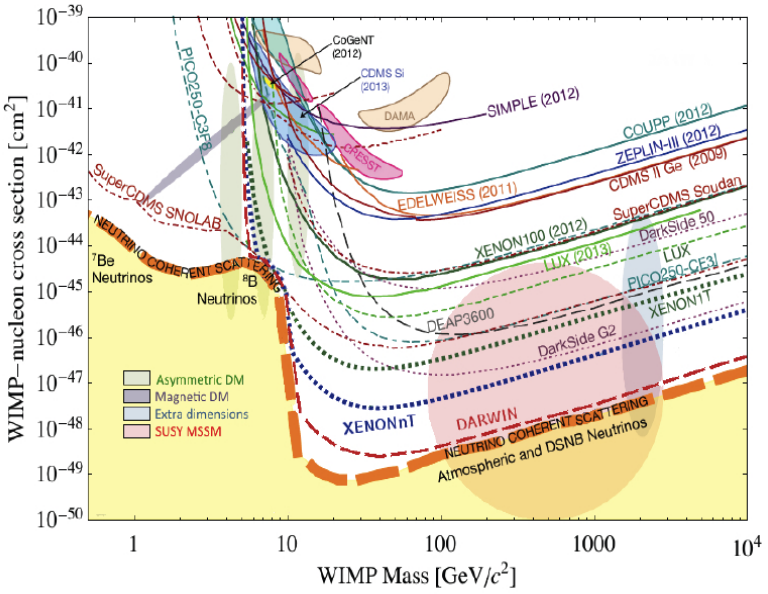

FIGURE 2.2: From L. Baudis [43]. Summary of current constraints (full lines), hits for DM signal (shaded closed contours) and next expectation limits (broken lines) on SI DM-nucleon cross-section form direct detection.

from direct detection experiments [44]. The differential rate of events can be expressed as [23, 43]:

$$\frac{\mathrm{d}\mathcal{R}}{\mathrm{d}E_{\mathcal{R}}} = \mathrm{N_T}\frac{\rho_{\odot}}{m_{\mathrm{DM}}}\int_{v_{\mathrm{min}}}^{v_{\mathrm{max}}} \mathrm{d}\vec{v} f\left(\vec{v}\right)\frac{\mathrm{d}\sigma_{(DM-N)}}{\mathrm{d}E_{\mathcal{R}}} \tag{2.2}$$

where $\mathrm{N_T}$ is the number of target nuclei, m_{DM} is the DM mass and the recoil energy $E_{\mathcal{R}} = m_r^2 v^2 \left(1 - cos\Theta\right)/m_{\mathrm{N}}$. The scattering angle in the center-of-mass frame is Θ, m_{N} and m_r are the nuclear and reduced mass respectively. The minimum velocity is defined ad $v_{\mathrm{min}} = \left(m_{\mathrm{N}}E_{\mathrm{th}}/2m_r^2\right)^{1/2}$ with E_{th} the energy threshold of the detector and v_{max} the escape velocity in the Earth frame. The $\sigma_{\mathrm{DM\text{-}N}}$ scattering cross-section is actually a combination of a spin-independent (SI) and spin-dependent (SD) components. Without entering in details, the contribution to the SI or SD component depends on the DM candidate [23]. In Fig. 2.2, we show an overview of the exclusion limits of DM-Nucleus SI cross-section versus the DM mass of current and next generation of direct search experiments for WIMPs DM. The next generation of experiments such as DarkSide-50, LUX, XENON1T and DARWIN [45] among others are designed to probe the entire parameter region for WIMP mass above $\sim$ 6 GeV to the TeV scale and until the neutrino background dominates the recoil spectrum.

2.3 Indirect Detection

As we discussed in Section 1.4, astrophysical and cosmological probes tell us that the 26.8% of the content of the Universe is DM [9]. Such DM is distributed from small to large scale. On the one hand, the Milky Way rotation curve shows that DM is inside the Galaxy [14] and the dSphs are some of the most DM-dominated objects known [46]. On the other hand, gravitational lensing by galaxy clusters also allows to establish the presence of DM on larger scales. For these reasons, searching for DM signals in astrophysical sources is well motivated. If a DM component dominates in such systems, DM particles may annihilate or decay into SM particles and the signature of the final products of such processes may be detected taking into account the uncertainties in the astrophysical background component. Because of this kind of interaction, we can perform DM model independent searches. In DM-DM→SM-SM events the SM annihilation/decay spectra for a given channel is independent by the DM model if internal Bremsstrahlung can be neglected, while it depends only on the energy of the event, that is proportional to the DM mass. The probability of annihilation or decay in different channels of the SM, then gives information about the DM nature. This fact allows to perform a broad study on DM searches and give new prospects for physics beyond the SM. However, this kind of research is affected by numerous uncertainties due to the DM density distribution, the background estimation and the simulation of the produced secondary flux of SM particles with Monte Carlo events generator code (Chapter 7). This section is dedicated to review the physics of indirect search of DM and to introduce the pillar equations that will be useful in the rest of this thesis.

The multimessenger astroparticle approach to the study of the final products of DM-DM→SM-SM process is fundamental for DM detection [47]. The final flux observed at the Earth for different cosmic rays has some common characteristics so as some differences, depending on the physics of emission, propagation and detection. We give a single equation in order to join the common part and discuss the differences between different cases. The secondary products of annihilation and decay of DM particles contribute to the cosmic-ray differential flux at the Earth as

$$\frac{d\Phi_{\text{cr-DM}}}{dE} = \eta_{\text{cr}} \cdot \sum_{a=1}^{2} \sum_{i}^{\text{SM channels}} \frac{\zeta_i^{(a)}}{a} \frac{dN_i^{(\text{cr})}}{dE} \cdot \frac{\kappa_{\text{cr}}^{(a)}}{4\pi\ m_{\text{DM}}^{a}}, \tag{2.3}$$

where:

- η_{cr} depends on the secondary particle (cosmic-ray) of interest and the physics of its propagation. In particular, $\eta_\gamma = 1$ for gamma-ray secondary flux (Chapter 3 and 4). In Chapter 5 we show that for neutrinos $\eta_{\nu_f} \equiv \sum_{p=1}^{3} P_{fp}$, where p is the

neutrino flavor at the source and f at the observer and the matrix P for astrophysical neutrinos depends on the mixing angle and neutrino oscillation. Finally, $\eta_{\rm cr}$ depends on the *charged* particle velocity as described in Chapter 6 for antiprotons.

- The total flux is given by decay ($a = 1$) and annihilation ($a = 2$) events of DM particles into the i-th SM particle (decay/annihilation channel). The ζ factor discerns between these two cases: $\zeta_i^{(1)} = \langle 1/\tau_i^{\rm decay} \rangle$ and $\zeta_i^{(2)} = \langle \sigma_i v \rangle$ are respectively the averaged of the inverse of the decay time and the medium thermal averaged annihilation cross section times velocity. The probability that DM annihilates or decays into the i-th channel depends on the nature of DM. In Chapter 4 we will give same applications to Branon DM.

- The differential number $dN_i^{\rm (cr)}/dE$ of cosmic-rays produced at the source by subsequent events of annihilation or decay of SM particles is simulated by means of Monte Carlo events generator codes, such as `PYTHIA` or `HERWIG`. Some uncertainties may be introduced in the evaluation of both the ζ_i and $\kappa_{\rm cr}$ factor due to the choice of the Fortran or C++ versions of `PYTHIA` or `HERWIG` code, as discussed in Chapter 7 for the particular case of gamma rays.

- For galactic sources, the $\kappa_{\rm cr}$ factor depends on the astrophysics of DM distribution as well as on the cosmic-ray propagation. Such κ-factor will be discussed in detail in the next Section 2.3.1.

- $m_{\rm DM}$ is the DM mass. Usually, it represents one of the free parameters that needs to be fitted with experimental data.

2.3.1 κ-factor.

As introduced, the κ-factor includes the properties of DM distribution (astrophysical factor) and cosmic-rays propagation (diffusion factor) depending on whether we are dealing with secondary flux of *neutral* or *charged* particles. *Neutral* particles as gamma rays and neutrinos propagate almost in straight line, without interaction with the magnetic field or the Interstellar Medium (ISM). In this case, we can determine with a certain precision the source of the observed flux. This is not the case of *charged* particles which interact with both the galactic and solar magnetic fields in addition to the ISM. In this case, we get a diffuse flux of particles coming from all the points of the Galaxy. In this section we discuss the two cases in detail.

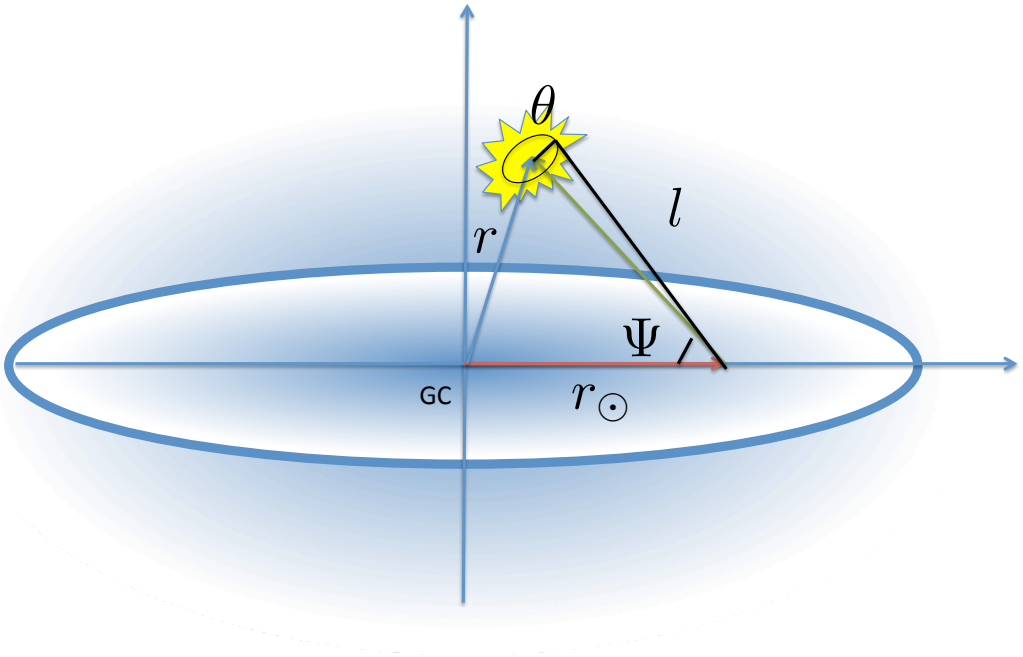

FIGURE 2.3: Geometry of the Milky Way coordinate system related to the astrophysical factor estimation. The yellow form represents a generic DM substructure in the Galactic halo, located at distance r from the GC. The astrophysical factor depends on the distance l of the structure with respect to the observer at the Earth (located at $r\odot = 8.5$ Kpc from the same GC), and on the angle Ψ. The ability to resolve the dimension of the source depends on the detector angular resolution θ. The numerical value of the astrophysical factor depends also on the local DM distribution.

2.3.1.1 Astrophysical factor

When the secondary particle of interest is *neutral*, that is the case of gamma rays and neutrinos, we can neglect the effects of particle diffusion in the Galaxy. The particle travels along an almost straight line from the source to the observer, so that the final flux observed on the Earth depends only on the flux emitted at the source and the DM distribution $\rho(r)$. In any case, the precision in the determination of the position and the angular dimension of the emitting source depends on the angular resolution of the device. In this case, the κ-factor is the astrophysical factor:

$$\kappa_{\gamma,\nu} \equiv \langle J_{(a)} \rangle_{\Delta\Omega} = \frac{1}{\Delta\Omega} \int_{\Delta\Omega} \mathrm{d}\Omega \int_0^{l_{max}(\Psi)} \rho^a[r(l)] dl(\Psi) \,. \tag{2.4}$$

In Eq. (1.13) we gave two expressions for the DM distribution $\rho(r)$. For $a = 1$, 2 DM decay or annihilate respectively. As illustrated in Fig. 2.3, in the case of the Milky

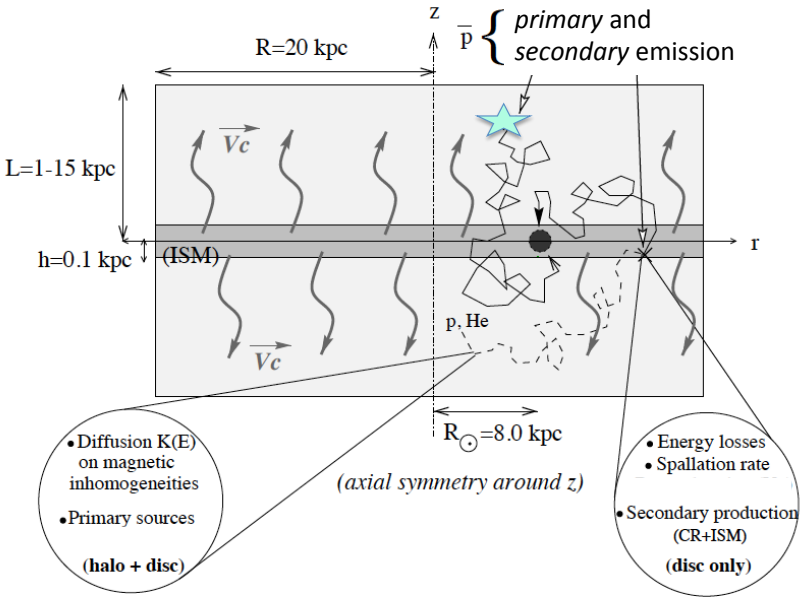

FIGURE 2.4: Barrau et al. [48]. Because of the propagation and diffusion of charged particles in the Galaxy, directional observation are not achievable. The antiprotons produced in a point of the Galaxy (green star) are received as a diffuse flux at the Earth (black spot). This is because of the interaction with magnetics field and ISM (see Section 2.3.1.2 and Chapter 6).

Way, l is the distance from the Sun to any point in the Galaxy disk and halo. The radial distance r of any point in the halo is measured from the GC, and is related to l by $r(l,\Psi)^2 = l^2 + r_\odot^2 - 2r_\odot l\cos\Psi$, where $r_\odot \simeq 8.5$ kpc is the distance from the Sun to the center of the Galaxy. The distance from the Sun to the edge of the halo in the direction Ψ from the GC is $l_{max} = r_\odot\cos\Psi + \sqrt{r^2 - r_\odot^2\sin\Psi}$. Then, for *un-charged* particles, *directional* observations are feasible. The astrophysical factor depends on solid angle of the detector, that is typically of order of $\Delta\Omega = 2\pi(1-\cos\theta)$, being θ the angular resolution or open angle of the telescope. The scale parameters of the DM density distribution such that in Eq. (1.13) are fixed so that $\rho_{\rm DM}(r_\odot) = 0.3\,{\rm GeVcm}^{-3}$ approximately as by cosmological constraints.

2.3.1.2 Diffusion factor

Charged cosmic-ray propagation in the Galaxy is a complex process affected by many different physical phenomena, such as the interaction with both the Galactic magnetic field and wind, and the ISM. For this reason *directional* observations are *not* achievable.

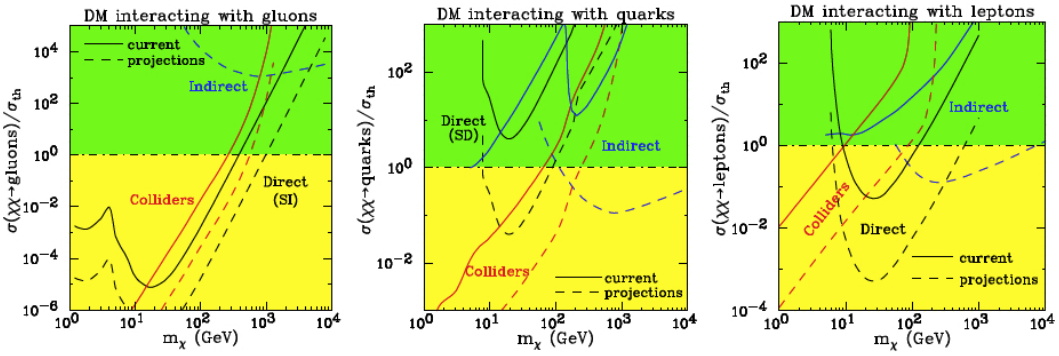

FIGURE 2.5: From D. Bauer et al. [51]. Current (full line) and expected (broken line) constraints for direct, indirect and collider search of DM annihilating in (from the left to the right) gluons, quarks and leptons channel.

In fact, on the one hand, the signal detected on the Earth is a combination of the signal emitted in all the points of the Galactic halo, propagated and diffused all around. On the other hand, the signal produced from a Galactic source is spread and reaches the Earth in different points (Fig. 2.4). Propagation parameters are set by boron-to-carbon (B/C) and subiron-to-iron (sub-Fe/Fe) cosmic-ray nuclei data analyses. Different configurations of parameters may be compatible with both sets of data [48, 49]. In this case the κ-factor is a diffusion term that takes into account the effects mentioned before:

$$\kappa_{\bar{\text{cr}}} \equiv R_{\bar{\text{cr}}}(r_\odot, E). \tag{2.5}$$

The diffusion factor at the position of the sun $R_{\bar{\text{cr}}}(r_\odot, E)$ for a generic *charged* cosmic-ray $\bar{\text{cr}}$ is the solution of a diffusion equation that depends on the particle of interest and on the DM source and distribution. As an example, we will review in the Chapter 6 the general case for antiproton production and diffusion. Similar equations have been developed in literature for electron, positron, deuteron and so on. They can been found for example in [50].

2.4 State of the art: experimental search

In this chapter we have introduced the experimental techniques that are used for DM searches. Although weakly interacting, DM particles are expected to have a non-vanishing annihilation and interaction cross-sections with SM particles. As illustrated in Fig. 2.5, direct, indirect and collider searches cover different areas of the $\sigma - m_{DM}$ parameter space. The figure shows the state of the art of the current and next generation of DM experiments [51]. In spite of numerous efforts, no conclusive results have been obtained so far. Recently, LHC got important results in the physics of the SM with the

discovery of the Higgs particle, but no signal of physics beyond the SM. In 2008, the working group of DAMA/LIBRA underground laboratory claimed for a DM signal at low DM masses, but such an observation has not been confirmed yet by other experiments [52]. Important limits seem to be associated with direct and collider experiments at high energy. In this Chapter, we focused in particular on the indirect search. We have reviewed in detail the equations for several cosmic-ray secondary fluxes. We have illustrated the similarities in the general form of the equations for different cosmic rays and discussed the differences in the η and κ factors. Current cosmic-ray observations allow to set constraints on DM masses and models [53]. In the following Chapters of this thesis we will investigate a particular astrophysical source, the GC. We will show that data from current generation of gamma-ray, neutrino and antiproton experiments suggest the possibility of a TeVDM candidate. Such an energy scale is actually unconstrained by direct research and colliders experiments and represents a new frontier for particle physics.

Chapter 3

Gamma-ray Flux from the Galactic Center

In the framework of indirect searches, the observation of gamma-ray fluxes from astrophysical sources represents one of the main approaches to solve the DM puzzle. If DM annihilates into SM particles, the subsequent chains of decay and hadronization of unstable products produce gamma-ray photons generically. The observation of this signal is highly affected by astrophysical uncertainties in the gamma-ray backgrounds and in the DM densities and distribution (see Chapter 7). On the other hand, depending on both astrophysical and particle physics models of DM, the signature could be distinguishable from the background. Appealing targets for gamma-ray observations of annihilating DM are mainly selected according to the abundance of DM in the source and their distance. Galaxy clusters, dSphs or the GC of the Milky Way are traditional targets of interest. Galaxy clusters are very rich in DM, but they are very distant objects. DSphs are also characterized by high DM densities but at much shorter distances. In any case, despite their proximity, observations of dSphs have not been able to detect any gamma-ray flux signature over the background so far [54, 55]. On the other hand, the GC represents a very close target, but the complexity of the region, due to the high concentration of sources, makes the analysis quite involved.

In this Chapter, we will focus on the analysis of very high energy (VHE) gamma rays coming from the GC. Different observations from the GC have been reported by several collaborations such as CANGAROO [56], VERITAS [57], HESS [58, 59], MAGIC [60] and FERMI-LAT [55, 61]. In particular, we will analyze the data collected by the HESS collaboration during the years 2004, 2005, and 2006 associated with the HESS J1745-290 GC source [59]. The interpretation of these fluxes as DM signal has been widely

discussed in the literature from the very early days of the publication of the observed data [62–65]. It was concluded that the spectral features of these gamma rays disfavored the DM origin [65, 66]. However, in recent studies [36, 67], it has been pointed out that these fluxes are compatible with the spectral signal of DM annihilation provided it is complemented with a simple background. This background of gamma rays can be originated by radiative processes generated by particle acceleration in the vicinity of Sgr A East supernova and the supermassive black hole [68]. We present a systematic study of this assumption: In Section 3.1, we show an analysis of the source. A brief review of the Eq. (2.3) in the case of gamma rays from annihilating DM is presented in Section 3.2. The fit of the HESS data with a total fitting function given by the combination of the background power law component with an annihilating DM signature is discussed in Section 3.3. In Section 3.4, we show that the fit to HESS data is also compatible with FERMI-LAT data from the same region. We summarize the main results of this Chapter in Section 3.5. Finally, the Appendix A provides useful details for reproducing the statistical study performed. This Chapter is based on [36] and [69].

3.1 HESS J1745-290 data

DM is expected to be clumped in the central region of standard galaxies. In this sense, the central part of the Milky Way could be an important source of gamma rays produced in the DM annihilation processes. Because of its closeness, the GC represents a very appealing target for the indirect search of DM, but the complex nature of this area makes the identification of the sources quite difficult. Several sources have been detected not only in the gamma-ray, but also in the infrared and X-ray ranges of the spectrum. The absence of variability in the collection of HESS J1745-290 data in the TeV scale, during the years 2004, 2005 and 2006, suggests that the emission mechanism and emission regions differ from those invoked in the variable infrared and X-ray emissions [70]. The significance of the signal reduces to few tenths of degree [59], but the angular distribution of the VHE gamma-ray emission shows the presence of an adjunctive diffuse component. The fundamental nature of this source is still unclear. These gamma rays could have been originated by particle propagation [68, 71] in the neighborhood of the Sgr A East supernova remnant and the supermassive black hole Sgr A, both located at the central region of our galaxy [66, 72]. If it was originated by the DM distribution, the morphology of the source requires a very compressed DM structure. In fact, it has been claimed [15, 73] that baryonic gas could account for similar effects when falling to the central region, modifying the gravitational potential and increasing the DM density in the center (see however [74, 75]). If this is the case, the DM annihilating fluxes are expected to

be enhanced by an important factor with respect to DM alone simulations, such as the classical NFW profile [15].

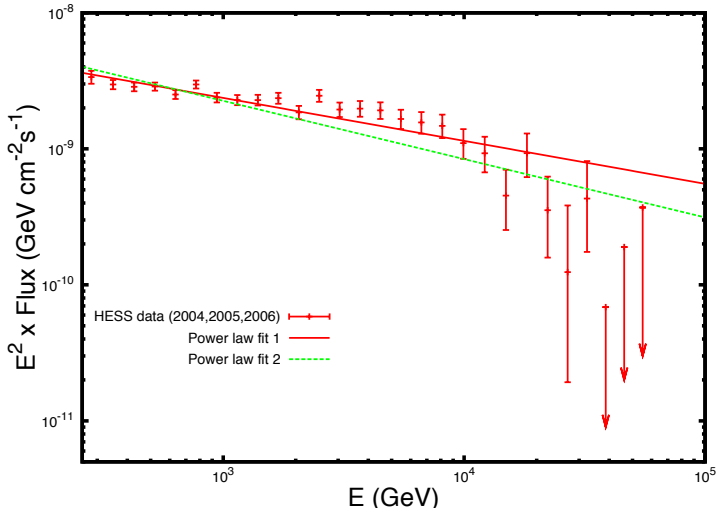

	Power law 1	Power law 2
Φ_0	20.9 ± 5.1	43.5 ± 14.8
Γ	2.32 ± 0.03	2.43 ± 0.05
$\chi^2/\,\mathrm{dof}$	2.48(57/23)	5.30(137/26)

FIGURE 3.1: Collection of the HESS data (2004,2005 and 2006) fitted with two simple power law background. The full line (Power law 1) shows the fit with 23 dof, without take into account the upper limit constraints on the flux given by the last three points. They are included in the Power law 2 fit with 26 dof (dotted line). The parameters of the fit can be found in the table. Because of the poorness of both the fits ($\chi^2/dof = 2.48$ with $\Gamma = 2.32 \pm 0.03$ for Power law 1, and $\chi^2/dof = 5.30$ with $\Gamma = 2.43 \pm 0.03$ for Power law 2), they represent just an upper limit of the flux. These results are consistent with previous studies [59, 72].

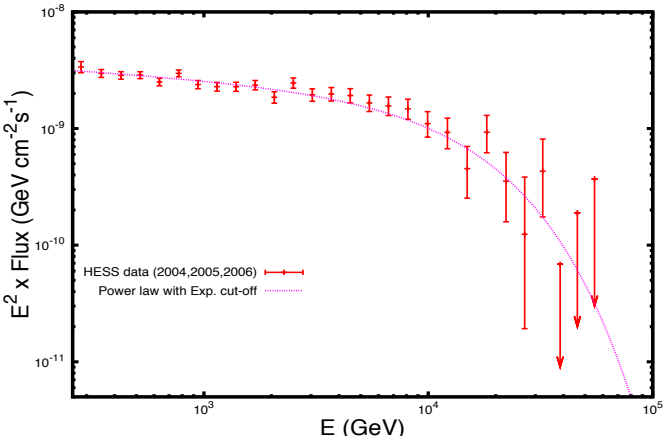

	$Exp_{Cut-off}$ law
Φ_0	6.24 ± 1.53
Γ	2.12 ± 0.04
E_{Cut}	13.8 ± 2.3
$\chi^2/\,\mathrm{dof}$	0.87(21/25)

FIGURE 3.2: The same as in Fig. 3.1, but the power law is modified with an exponential energy cut-off. The signal is well fitted in this case with the results given in the attached table.

In previous works [59, 72], important deviations from a power law spectrum have been already reported, and a cut-off at several tens of TeVs has been proved as a distinctive feature of the spectrum. For instance, the observed data were compared to a simple power law:

$$\frac{d\Phi_{\gamma-Bg}}{dE} = \Phi_0 \cdot \left(\frac{E}{\mathrm{GeV}}\right)^{-\Gamma} , \tag{3.1}$$

and a power law with high energy exponential cut-off:

$$\frac{d\Phi_{\gamma-Bg}}{dE} = \Phi_0 \cdot \left(\frac{E}{\text{GeV}}\right)^{-\Gamma} \cdot e^{-\frac{E}{E_{cut}}} , \tag{3.2}$$

where Φ_0 is the flux normalization, Γ is the spectral index and E_{cut} is the cut-off energy. The measured spectrum for the three-year dataset ranges from 260 GeV to 60 TeV. We have reproduced these analyses with the results that can be found in Figs. 3.1 and 3.2. They are consistent with previous works [59, 72], since the spectrum is well described by a power law with exponential cut-off (Fig. 3.2), while a simple power law is clearly inconsistent (Fig. 3.1).

3.2 Gamma-rays from Dark Matter Annihilation

If the signal observed from the GC is a combination of gamma-ray photons from annihilating DM and a background, the total fitting function for the observed differential gamma-ray flux will be:

$$\frac{d\Phi_{\gamma-Tot}}{dE} = \frac{d\Phi_{\gamma-Bg}}{dE} + \frac{d\Phi_{\gamma-DM}}{dE}. \tag{3.3}$$

We will assume a simple power law background parameterized as:

$$\frac{d\Phi_{\gamma-Bg}}{dE} = B^{(\gamma)\,2} \cdot \left(\frac{E}{\text{GeV}}\right)^{-\Gamma}. \tag{3.4}$$

On the other hand, the differential gamma-ray flux originated from DM annihilation in galactic structures and substructures can be written generically as the Eq. (2.3) with $a = 2$, that means $\zeta_i^{(2)} = \langle \sigma_i v \rangle$ the thermal averaged annihilation cross-sections of two DM particles into SM particles (also labeled by the subindex i), $\eta = 1$ and $\kappa = \kappa_\gamma = \langle J_{(2)} \rangle_{\Delta\Omega}$:

$$\frac{d\Phi_{\gamma-\text{DM}}}{dE} = \sum_i^{\text{channels}} \frac{\langle \sigma_i v \rangle}{2} \cdot \frac{dN_i^{(\gamma)}}{dE} \cdot \frac{\Delta\Omega \, \langle J_{(2)} \rangle_{\Delta\Omega}}{4\pi m_{\text{DM}}^2} \tag{3.5}$$

We are assuming that the DM particle is its own antiparticle. m_{DM} is the mass of the DM particle, and the number of photons produced in each annihilating channel $dN_i^{(\gamma)}/dE$, involves decays and/or hadronization of unstable products such as quarks and leptons. Because of the non-perturbative QCD effects, the calculation of $dN_i^{(\gamma)}/dE$ requires Monte Carlo events generators such as `PYTHIA` [76]. In our analysis, we will focus

on gamma rays coming from external bremsstrahlung and fragmentation of SM particle-antiparticle pairs produced by DM annihilation. We will ignore DM decays, the possible production of monoenergetic photons, N-body annihilations (with $n > 2$), or photons produced from internal bremsstrahlung, that are model dependent. In particular and in order to simplify the discussion and provide useful information for a general analysis, we will consider DM annihilation in each single channel of SM particle-antiparticle pairs, i.e.

$$\frac{d\Phi^i_{\gamma-\mathrm{DM}}}{dE} = A_i^{(\gamma)\,2} \cdot \frac{dN_i^{(\gamma)}}{dE} \,, \tag{3.6}$$

where

$$A_i^{(\gamma)\,2} = \frac{\langle \sigma_i v \rangle \, \Delta\Omega \, \langle J_{(2)} \rangle_{\Delta\Omega}}{8\pi m^2_{\mathrm{DM}}} \tag{3.7}$$

is a new constant to be fitted together with the DM particle mass m_{DM}, and the background parameters $B^{(\gamma)}$ and Γ. The astrophysical factor $\langle J_{(2)} \rangle_{\Delta\Omega}$ of Eq. (3.5) will be also indirectly fitted by means of the parameter $A_i^{(\gamma)}$. The dark halo in the GC is usually modelled by the NFW profile [77] (the first of Eq.s (1.13)). This profile is in good agreement with non-baryonic cold DM simulations of the GC. In this case and accounting for just annihilating DM, the astrophysical factor is: $\langle J^{\mathrm{NFW}}_{(2)} \rangle \simeq 280 \cdot 10^{23}$ GeV^{2}cm^{-5}, value that we will use as standard reference.

3.3 Single-channel fits

As commented before, the particle model part of the differential gamma-ray flux expected from the GC is simulated by means of Monte Carlo event generators, such as `PYTHIA` [76]. However, the fact that simulations have to be performed for fixed DM mass implies that we cannot obtain explicit m_{DM} dependence for the photon spectra. In order to overcome this limitation, the simulated spectra of each annihilation channel has been reproduced with the analytic fitting functions provided in Ref. [38] in terms of the WIMP mass, by means of mass dependent parameters. The combination of such simulated spectra with a power law background (Eq. (3.3)) is finally fitted. We assume a typical experimental resolution of 15% ($\Delta E/E \simeq 0.15$) and a perfect detector efficiency.

For quarks (except the top) electron and τ leptons, the most general formula needed to reproduce the behaviour of the differential number of photons in an energy range may be written as:

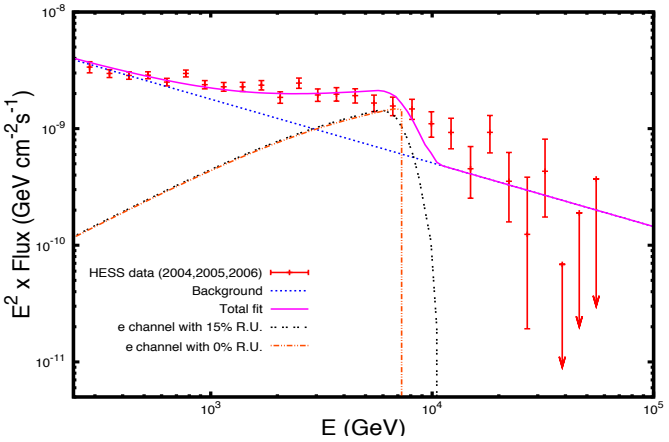

Channel	e^+e^-
$m_{\rm DM}$	7.51 ± 0.11
$A^{(\gamma)}$	8.12 ± 0.73
$B^{(\gamma)}$	2.78 ± 0.79
Γ	2.55 ± 0.06
$\chi^2/\,{\rm dof}$	2.09
$\Delta\chi^2$	32.6
b	111 ± 20

e^-e^+	$m_{\rm DM}$	$A^{(\gamma)}$	$B^{(\gamma)}$	Γ
$m_{\rm DM}$	1			
$A^{(\gamma)}$	-0.385	1		
$B^{(\gamma)}$	-0.044	0.512	1	
Γ	-0.070	0.583	0.991	1

FIGURE 3.3: $m_{\rm DM}$(TeV), $A^{(\gamma)}(10^{-7}\,{\rm cm}^{-1}{\rm s}^{-1/2})$, $B^{(\gamma)}(10^{-4}\,{\rm GeV}^{-1/2}{\rm cm}^{-1}{\rm s})$. Best fit to the HESS J1745-290 collection of data (years 2004,2005, and 2006 [59]) in the case that the DM contribution came entirely from annihilation into e^+e^-. The full line shows the total fitting function. The poor quality of the fit is evident ($\chi^2/dof = 2.09$). The dotted line shows the simple power law background component with spectral index $\Gamma = 2.55 \pm 0.06$, while the DM component with a 15% of resolution uncertainity (R. U.) is given by the double-dotted line with a normalization parameter $A^{(\gamma)}$. The dotted-dashed line shows the contribution of annihilating DM into electron-positron pairs without taking into account such a resolution. On the top right table, we present a summary of the best fitting parameters. $\Delta\chi^2$ correponds to the difference with respect to the best fit channel ($d\bar{d}$). On the bottom right table, we show the correlation matrix elements of this statistical analysis.

$$\frac{dN^{(\gamma)}}{dE} = \Big[a_1 \exp\left(-b_1 \left(\frac{E}{m_{\rm DM}}\right)^{n_1} - b_2 \left(\frac{E}{m_{\rm DM}}\right)^{n_2} - \frac{c_1}{\left(\frac{E}{m_{\rm DM}}\right)^{d_1}} + \frac{c_2}{\left(\frac{E}{m_{\rm DM}}\right)^{d_2}} \right) + q_1 \left(\frac{E}{m_{\rm DM}}\right)^{1.5} \ln\left[p_1 \left(1 - \left(\frac{E}{m_{\rm DM}}\right)\right)\right] \frac{\left(\frac{E}{m_{\rm DM}}\right)^2 - 2\left(\frac{E}{m_{\rm DM}}\right) + 2}{\left(\frac{E}{m_{\rm DM}}\right)} \Big] E^{-1.5} m_{\rm DM}^{0.5}. \quad (3.8)$$

The value of the different parameters change with the SM particle annihilation channel and in some cases, with the range of the WIMP mass. The cases of interest are described below and the value of the parameters reported in Appendix A.

In the case of the electron-positron channel, the only contribution to the gamma-ray flux

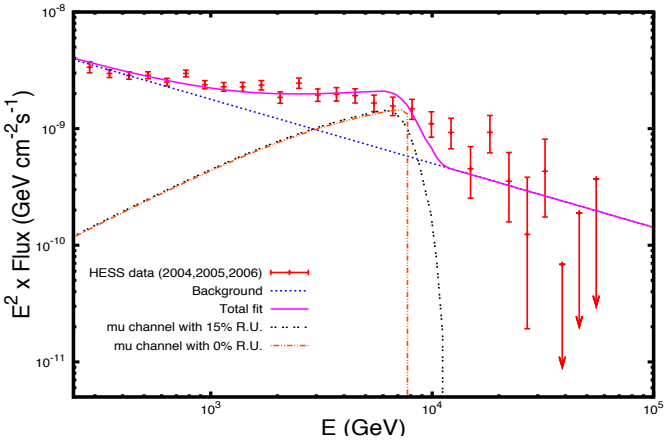

Channel	$\mu^+\mu^-$
$m_{\rm DM}$	7.89 ± 0.21
$A^{(\gamma)}$	21.2 ± 1.92
$B^{(\gamma)}$	2.81 ± 0.53
Γ	2.55 ± 0.06
$\chi^2/\,{\rm dof}$	2.04
$\Delta\chi^2$	31.4
b	837 ± 158

$\mu^+\mu^-$	$m_{\rm DM}$	$A^{(\gamma)}$	$B^{(\gamma)}$	Γ
$m_{\rm DM}$	1			
$A^{(\gamma)}$	-0.431	1		
$B^{(\gamma)}$	-0.052	0.515	1	
Γ	-0.081	0.584	0.991	1

FIGURE 3.4: The same as Fig. 3.3 in the case of the $\mu^+\mu^-$ annihilation channel. The fit is only slightly better than for the e^+e^- case.

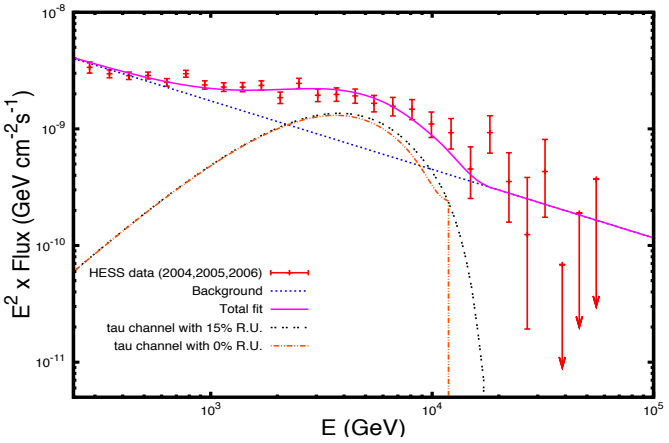

Channel	$\tau^+\tau^-$
$m_{\rm DM}$	12.4 ± 1.3
$A^{(\gamma)}$	7.78 ± 0.69
$B^{(\gamma)}$	3.17 ± 0.62
Γ	2.59 ± 0.06
$\chi^2/\,{\rm dof}$	1.59
$\Delta\chi^2$	20.6
b	278 ± 76

$\tau^+\tau^-$	$m_{\rm DM}$	$A^{(\gamma)}$	$B^{(\gamma)}$	Γ
$m_{\rm DM}$	1			
$A^{(\gamma)}$	-0.613	1		
$B^{(\gamma)}$	0.042	0.487	1	
Γ	-0.004	0.552	0.993	1

FIGURE 3.5: The same as Fig. 3.3 in the case of the $\tau^+\tau^-$ annihilation channel. This channel provides the best leptonic fit, although it is not enough to be consistent with data.

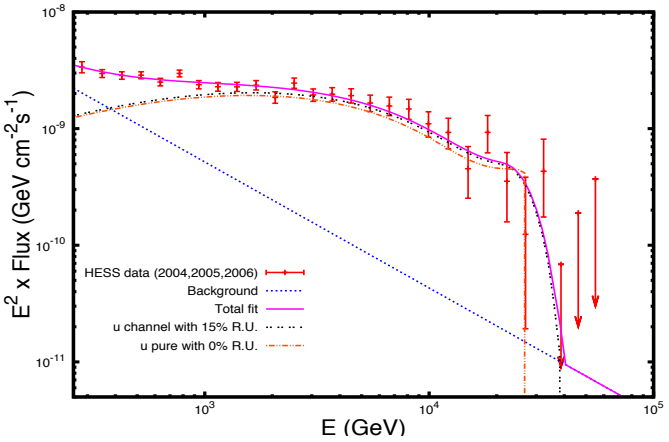

Channel	$u\bar{u}$
$m_{\rm DM}$	27.9 ± 1.8
$A^{(\gamma)}$	6.51 ± 0.46
$B^{(\gamma)}$	9.52 ± 9.47
Γ	3.08 ± 0.35
$\chi^2/\,\mathrm{dof}$	0.78
$\Delta\chi^2$	1.2
b	987 ± 189

$u\bar{u}$	M	$A^{(\gamma)}$	$B^{(\gamma)}$	Γ
$m_{\rm DM}$	1			
$A^{(\gamma)}$	-0.772	1		
$B^{(\gamma)}$	-0.291	0.768	1	
Γ	-0.315	0.792	0.999	1

FIGURE 3.6: The same as Fig. 3.3 in the case of the $u\bar{u}$ annihilation channel. The cut-off in the energy spectrum of this hadronic channel reproduces the cut-off in the data, giving good consistency.

comes from the bremsstrahlung of the final particles. Therefore, in the previous expression (3.8) the exponential contribution is absent, $q_1 = \alpha_{\rm QED}/\pi$, and $p_1 = (m_{\rm DM}/m_{e^-})^2$. This choice of the parameters corresponds to the well-known Weizsäcker-Williams approximation (Fig. 3.3).

In the case of the $\mu^+\mu^-$ channel, the exponential contribution in the expression above (3.8) is also absent. A proper fitting function for such a channel can be written as:

$$\frac{\mathrm{d}N^{(\gamma)}}{\mathrm{d}E} = q_1 \left(\frac{E}{m_{\rm DM}}\right)^{1.5} \ln\left[p_1\left(1-\left(\frac{E}{m_{\rm DM}}\right)^{l_1}\right)\right] \frac{\left(\frac{E}{m_{\rm DM}}\right)^2 - 2\left(\frac{E}{m_{\rm DM}}\right) + 2}{\left(\frac{E}{m_{\rm DM}}\right)} E^{-1.5} m_{\rm DM}^{0.5}. \quad (3.9)$$

All the parameters are here mass dependent and their expression for a range of mass $10^3\,\mathrm{GeV} \lesssim m_{\rm DM} \lesssim 5\times10^4$ GeV are reported in Tab. A.1. The best fit for the μ lepton is shown in Fig. 3.4.

The $\tau^+\tau^-$ spectrum needs the entire Eq. (3.8) for an accurate analysis. The value of the mass independent parameter and the expression of the mass dependent ones used in this work are reported in Tab. A.2. The best fit for the τ lepton is shown in Fig. 3.5.

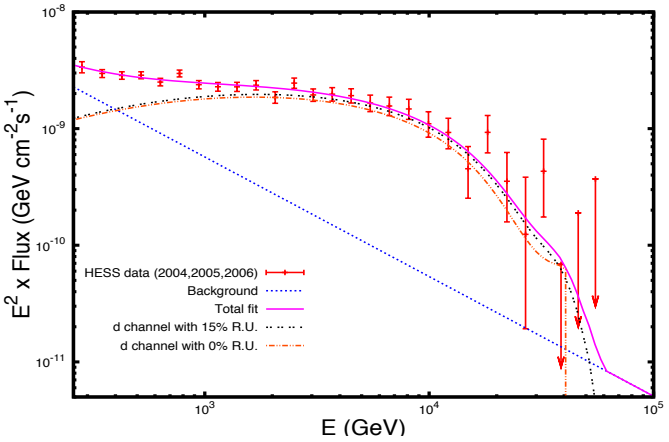

Channel	$d\bar{d}$
$m_{\rm DM}$	42.0 ± 4.4
$A^{(\gamma)}$	4.88 ± 0.48
$B^{(\gamma)}$	8.26 ± 7.86
Γ	3.03 ± 0.34
$\chi^2/\,\mathrm{dof}$	0.73
$\Delta\chi^2$	0.0
b	1257 ± 361

$d\bar{d}$	$m_{\rm DM}$	$A^{(\gamma)}$	$B^{(\gamma)}$	Γ
$m_{\rm DM}$	1			
$A^{(\gamma)}$	-0.883	1		
$B^{(\gamma)}$	-0.435	0.764	1	
Γ	-0.468	0.793	0.998	1

FIGURE 3.7: The same as Fig. 3.3 in the case of the $d\bar{d}$ annihilation channel. The χ^2/dof value associated with this analysis is the lowest one obtained in this work and it has been taken as reference to compute $\Delta\chi^2$.

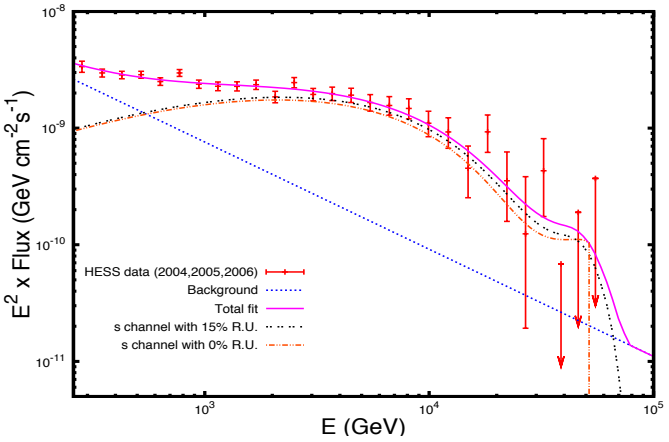

Channel	$s\bar{s}$
$m_{\rm DM}$	53.9 ± 6.2
$A^{(\gamma)}$	4.85 ± 0.57
$B^{(\gamma)}$	6.59 ± 5.43
Γ	2.92 ± 0.29
$\chi^2/\,\mathrm{dof}$	0.90
$\Delta\chi^2$	4.1
b	2045 ± 672

$s\bar{s}$	$m_{\rm DM}$	$A^{(\gamma)}$	$B^{(\gamma)}$	Γ
$m_{\rm DM}$	1			
$A^{(\gamma)}$	-0.852	1		
$B^{(\gamma)}$	-0.410	0.784	1	
Γ	-0.444	0.812	0.998	1

FIGURE 3.8: The same as Fig. 3.3 in the case of the $s\bar{s}$ annihilation channel.

The value of the mass independent parameter and the expression of the mass dependent ones in (3.8) for the $u\bar{u}$ channel are reported in Tab. A.3. The analytic fitting function is given for mass values up 8000 GeV, because of limitations in the Monte Carlo event generator `PYTHIA` code. An extrapolation up to larger values of the mass has been performed. In this case the best fit is shown in Fig. 3.6. The parameters for the $d\bar{d}$ channel are given in Tab. A.4. This channel provides the best fit (See Fig. 3.7) of all those considered in the paper and is used as a reference for comparison with other channels. The parameters for the $s\bar{s}$, $c\bar{c}$ and $b\bar{b}$ are reported in Tabs. A.5, A.6 and A.7. The best fit of these hadronic channels are shown in Figs. 3.8, 3.9 and 3.10.

The $t\bar{t}$ needs a different fitting function:

$$\frac{dN^{(\gamma)}}{dE} = a_1 \exp\left(-b_1 \left(\frac{E}{m_{\rm DM}}\right)^{n_1} - \frac{c_1}{\left(\frac{E}{M}\right)^{d_1}} - \frac{c_2}{\left(\frac{E}{m_{\rm DM}}\right)^{d_2}}\right) \times \left\{\frac{\ln\left[p_1\left(1-\left(\frac{E}{m_{\rm DM}}\right)^{l_1}\right)\right]}{\ln p_1}\right\}^{q_1} E^{-1.5} m_{\rm DM}^{0.5} \,. \tag{3.10}$$

The value of the mass independent parameter and the expression of the mass dependent ones (in the selected range of mass) are reported in Tab. A.8. The best fit for the $t\bar{t}$ channel by using Eq. (3.10) is shown in Fig. 3.11.

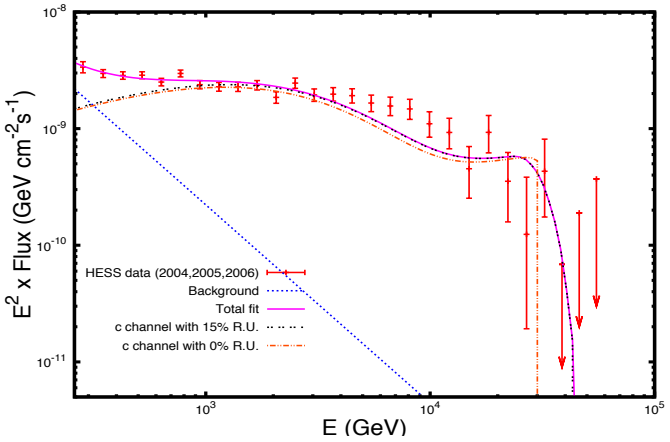

Channel	$c\bar{c}$
$m_{\rm DM}$	31.4 ± 6.0
$A^{(\gamma)}$	6.90 ± 1.06
$B^{(\gamma)}$	53.0 ± 157
Γ	3.70 ± 1.07
$\chi^2/\,\mathrm{dof}$	1.78
$\Delta\chi^2$	25.0
b	1404 ± 689

$c\bar{c}$	$m_{\rm DM}$	$A^{(\gamma)}$	$B^{(\gamma)}$	Γ
$m_{\rm DM}$	1			
$A^{(\gamma)}$	-0.970	1		
$B^{(\gamma)}$	-0.738	0.845	1	
Γ	-0.754	0.860	0.999	1

FIGURE 3.9: The same as Fig. 3.3 but for the $c\bar{c}$ channel. This is the quark channel most disfavored by the HESS data.

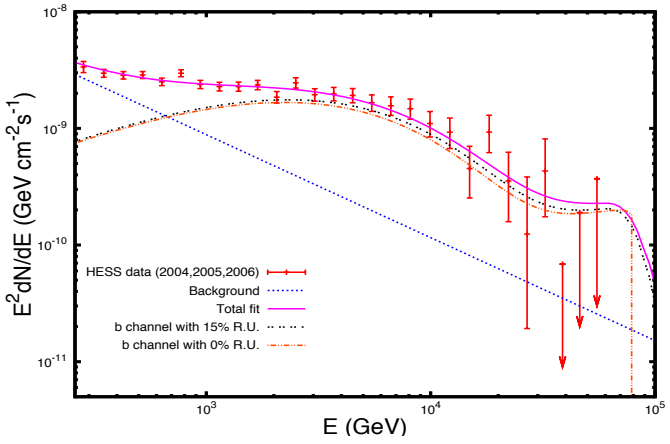

Channel	$b\bar{b}$
$m_{\rm DM}$	82.0 ± 12.8
$A^{(\gamma)}$	3.69 ± 0.61
$B^{(\gamma)}$	6.27 ± 6.07
Γ	2.88 ± 0.35
$\chi^2/\,\mathrm{dof}$	1.32
$\Delta\chi^2$	14.2
b	2739 ± 1246

$b\bar{b}$	$m_{\rm DM}$	$A^{(\gamma)}$	$B^{(\gamma)}$	Γ
$m_{\rm DM}$	1			
$A^{(\gamma)}$	-0.864	1		
$B^{(\gamma)}$	-0.499	0.834	1	
Γ	-0.529	0.857	0.999	1

FIGURE 3.10: The same as Fig. 3.3 for the $b\bar{b}$ annihilation channel. Together with the $c\bar{c}$ channel, is the only hadronic channel disfavored by the HESS data.)

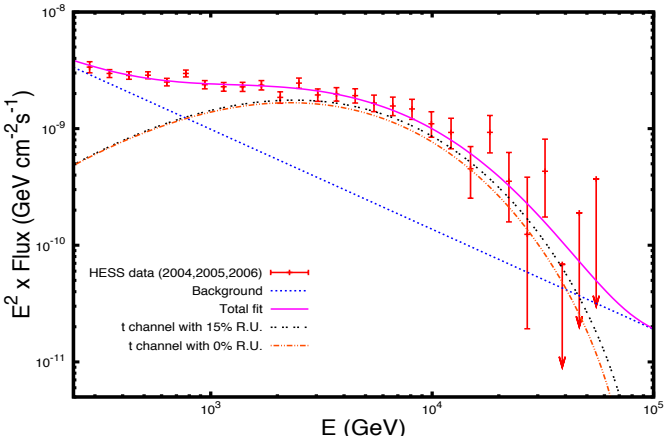

Channel	$t\bar{t}$
$m_{\rm DM}$	87.7 ± 8.2
$A^{(\gamma)}$	3.68 ± 0.34
$B^{(\gamma)}$	6.07 ± 3.34
Γ	2.86 ± 0.19
$\chi^2/\,\mathrm{dof}$	0.88
$\Delta\chi^2$	3.6
b	3116 ± 820

$t\bar{t}$	$m_{\rm DM}$	$A^{(\gamma)}$	$B^{(\gamma)}$	Γ
$m_{\rm DM}$	1			
$A^{(\gamma)}$	-0.748	1		
$B^{(\gamma)}$	-0.175	0.721	1	
Γ	-0.216	0.756	0.998	1

FIGURE 3.11: The same as Fig. 3.3 in the case of the $t\bar{t}$ annihilation channel. The qualitative features of this channel are more similar to the electroweak annihilations (see following figures) than to the hadronic ones (as it is shown in the previous figures). The quality of the fit is also good.

For the W and Z gauge bosons the parametrization is:

$$\frac{dN^{(\gamma)}}{dE} = a_1 \exp\left(-b_1\left(\frac{E}{m_{\rm DM}}\right)^{n_1} - \frac{c_1}{\left(\frac{E}{m_{\rm DM}}\right)^{d_1}}\right)\left\{\frac{\ln\left[p_1\left(j_1 - \frac{E}{m_{\rm DM}}\right)\right]}{\ln p_1}\right\}^{q_1} E^{-1.5} m_{\rm DM}^{0.5}\,, \tag{3.11}$$

where the value of the parameters used in this study are reported in Tab. A.9. The best fits for the W^+W^- and ZZ channels are shown in Figs. 3.12 and 3.13.

The best fit is provided by the $d\bar{d}$ channel with $\chi^2/dof = 0.73$ for a total of 24 degrees of freedom (dof). In any case, other hadronic channels such as $u\bar{u}$ (see Fig. 3.6) or $s\bar{s}$, also provide very good fits within 1σ. In the same way, softer spectra as the one provided by $t\bar{t}$ (see Fig. 3.11), W^+W^- (Fig. 3.12) or ZZ (Fig. 3.13) channels are consistent with data without statistical significance difference. On the contrary, leptonic channels (not only e^+e^-, or $\mu^+\mu^-$ but also $\tau^+\tau^-$, Figs. 3.3, 3.4 and 3.5), $c\bar{c}$ and $b\bar{b}$ channels (Fig. 3.9 and 3.10) are ruled out with more than 99% confidence level when compared to the best channel. It is interesting to note that taking into account all the channels that provide

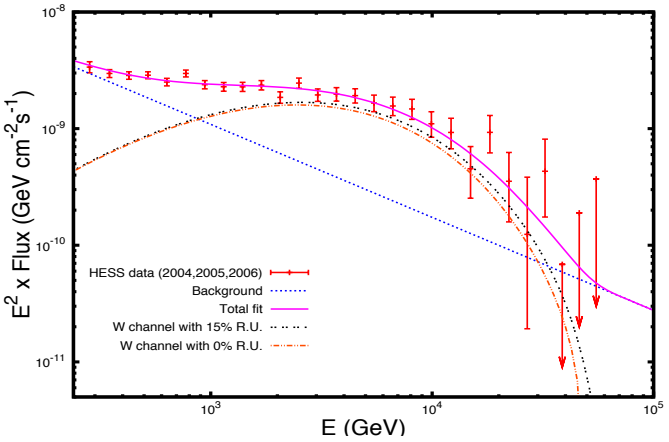

Channel	W^+W^-
$m_{\rm DM}$	48.8 ± 4.3
$A^{(\gamma)}$	4.98 ± 0.40
$B^{(\gamma)}$	5.18 ± 2.23
Γ	2.80 ± 0.15
$\chi^2/\,\mathrm{dof}$	0.84
$\Delta\chi^2$	2.6
b	1767 ± 419

W^+W^-	$m_{\rm DM}$	$A^{(\gamma)}$	$B^{(\gamma)}$	Γ
$m_{\rm DM}$	1			
$A^{(\gamma)}$	-0.687	1		
$B^{(\gamma)}$	-0.038	0.681	1	
Γ	0.008	0.636	0.997	1

FIGURE 3.12: The same as Fig. 3.3 for the W^+W^- annihilation channel.

a good fit, the DM mass is constrained to 15 TeV $\lesssim m_{\rm DM} \lesssim$ 110 TeV within 2σ. The lighter values are consistent with hadronic annihilations ($u\bar{u}$) and the heavier ones with the annihilation in $t\bar{t}$, that is more similar to electroweak channels. All the parameters fitted for the single annihilation channels are summarized in Tab. 3.1.

3.4 FERMI 1FGL J1745.6-2900 data

It has been argued that the FERMI-LAT source 1FGL J1745.6-2900 and the previously considered HESS source J1745-290 are spatially coincident [78]. In [71] data from the first 25 months of observations of the mentioned FERMI-LAT source have been analyzed. It has been shown that the observed spectrum in the range 100 MeV- 300 GeV can be very well described by a broken power law with a break energy of $E_{br} = 2.0^{+0.8}_{-1.0}$ GeV, and slopes $\Gamma_1 = 2.20 \pm 0.04$ and $\Gamma_2 = 2.68 \pm 0.05$ for lower and higher energies than E_{br} respectively. Notice that the fitted value of Γ_2 from FERMI-LAT data is in very good agreement with the spectral index of the diffuse background obtained from HESS data in our previous analyses. Indeed, at the 95% confidence level, the allowed range for the spectral index of the diffuse background is $2.6 \lesssim \Gamma \lesssim 3.7$. In this case, the lower values are consistent with all the allowed channels, but the higher values are only accessible to

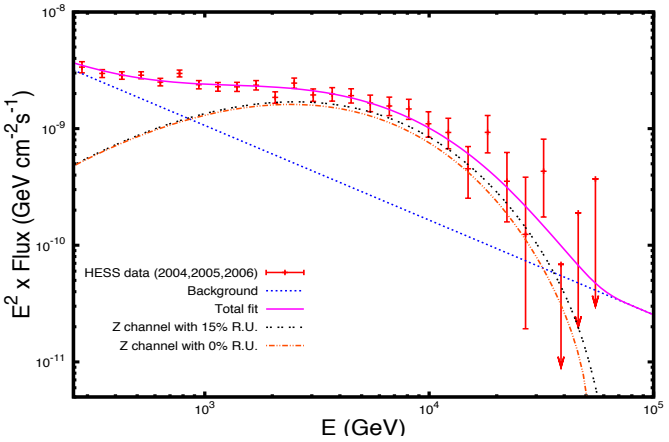

Channel	ZZ
$m_{\rm DM}$	54.5 ± 4.9
$A^{(\gamma)}$	4.73 ± 0.40
$B^{(\gamma)}$	5.38 ± 2.45
Γ	2.81 ± 0.16
$\chi^2/\,\mathrm{dof}$	0.85
$\Delta\chi^2$	2.9
b	1988 ± 491

ZZ	$m_{\rm DM}$	$A^{(\gamma)}$	$B^{(\gamma)}$	Γ
$m_{\rm DM}$	1			
$A^{(\gamma)}$	-0.704	1		
$B^{(\gamma)}$	-0.042	0.660	1	
Γ	-0.088	0.703	0.997	1

FIGURE 3.13: The same as Fig. 3.3 in the case of the ZZ annihilation. The results for the ZZ channel are very similar to the W^+W^- one. Both electroweak channels are consistent with the data.

Channel	$m_{\rm DM}$ (TeV)	$A^{(\gamma)}\,(10^{-7}\,\mathrm{cm^{-1}s^{-1/2}})$	$B^{(\gamma)}\,(10^{-4}\,\mathrm{GeV^{-1/2}cm^{-1}s^{-1/2}})$	Γ	$\chi^2/\,\mathrm{dof}$	$\Delta\chi^2$	b
e^+e^-	7.51 ± 0.11	8.12 ± 0.73	2.78 ± 0.79	2.55 ± 0.06	2.09	32.6	111 ± 20
$\mu^+\mu^-$	7.89 ± 0.21	21.2 ± 1.92	2.81 ± 0.53	2.55 ± 0.06	2.04	31.4	837 ± 158
$\tau^+\tau^-$	12.4 ± 1.3	7.78 ± 0.69	3.17 ± 0.62	2.59 ± 0.06	1.59	20.6	278 ± 76
$u\bar{u}$	27.9 ± 1.8	6.51 ± 0.46	9.52 ± 9.47	3.08 ± 0.35	0.78	1.2	987 ± 189
$d\bar{d}$	42.0 ± 4.4	4.88 ± 0.48	8.26 ± 7.86	3.03 ± 0.34	0.73	0.0	1257 ± 361
$s\bar{s}$	53.9 ± 6.2	4.85 ± 0.57	6.59 ± 5.43	2.92 ± 0.29	0.90	4.1	2045 ± 672
$c\bar{c}$	31.4 ± 6.0	6.90 ± 1.06	53.0 ± 157	3.70 ± 1.07	1.78	25.0	1404 ± 689
$b\bar{b}$	82.0 ± 12.8	3.69 ± 0.61	6.27 ± 6.07	2.88 ± 0.35	1.32	14.2	2739 ± 1246
$t\bar{t}$	87.7 ± 8.2	3.68 ± 0.34	6.07 ± 3.34	2.86 ± 0.19	0.88	3.6	3116 ± 820
W^+W^-	48.8 ± 4.3	4.98 ± 0.40	5.18 ± 2.23	2.80 ± 0.15	0.84	2.6	1767 ± 419
ZZ	54.5 ± 4.9	4.73 ± 0.40	5.38 ± 2.45	2.81 ± 0.16	0.85	2.9	1988 ± 491

TABLE 3.1: In this table, the four parameters of the annihilating DM into a single channel fit are presented: The fitted value of the mass (TeV) of the annihilating WIMPs, normalization factor of the signal $A^{(\gamma)}\,(10^{-7}\,\mathrm{cm^{-1}s^{-1/2}})$, normalitazion factor of the gamma ray diffuse emission background $B^{(\gamma)}\,(10^{-4}\,\mathrm{GeV^{-1/2}cm^{-1}s^{-1/2}})$, and spectral index Γ of the same background. The χ^2 per degree of freedom (dof), and the value of its variation $\Delta\chi^2 \equiv \chi^2 - \chi^2_{d\bar{d}}$ with respect to the best one ($\chi^2_{d\bar{d}}$) is also provided (In the case of four parameters, values of $\Delta\chi^2 = 4.72\,, 9.70$ and 13.3 correspond to $68.3\%\,, 95.4\%$ and 99.0% confidence level, respectively). Finally, the astrophysical factor is computed by assuming $\langle\sigma v\rangle = 3 \cdot 10^{-26}\ \mathrm{cm^3 s^{-1}}$, and presented in units of the the astrophysical factor associated with a NFW profile: $b \equiv \langle J_{(2)}\rangle / \langle J^{\rm NFW}_{(2)}\rangle$, where $\langle J^{\rm NFW}_{(2)}\rangle \simeq 280 \cdot 10^{23}\ \mathrm{GeV^2 cm^{-5}}$.

the light quark channels. In any case all the channels that provide a good fit to HESS data are also consistent with the spectral index observed by FERMI-LAT.

In Fig. 3.14, we show the case of the W^+W^- channel to illustrate this consistency. Both the signal and background parameters are compatible with the W^+W^- channel fit without the FERMI-LAT data. With the new data, the analysis even improves to $\chi^2/dof = 0.75$. This interpretation implies that the FERMI-LAT telescope is able to detect just the background component of the total energy spectrum of the gamma-ray emission associated with DM.

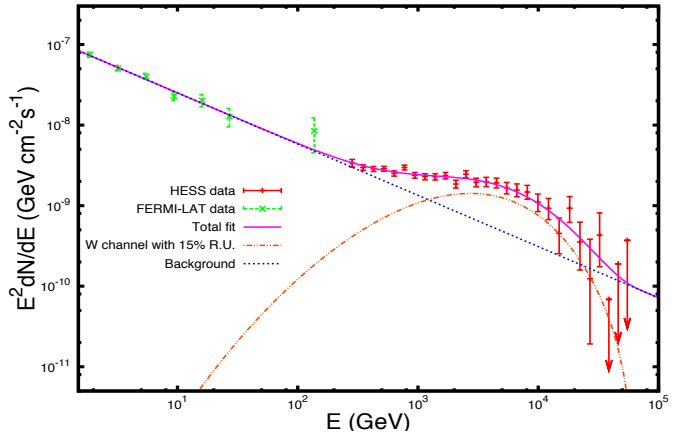

(FERMI-LAT Data)	W^+W^-
$m_{\rm DM}$	51.7 ± 5.2
$A^{(\gamma)}$	4.44 ± 0.34
$B^{(\gamma)}$	3.29 ± 1.03
Γ	2.63 ± 0.02
$\chi^2/$ dof	0.75

	$m_{\rm DM}$	$A^{(\gamma)}$	$B^{(\gamma)}$	Γ
$m_{\rm DM}$	1			
$A^{(\gamma)}$	-0.879	1		
$B^{(\gamma)}$	-0.206	0368	1	
Γ	-0.481	0.718	0.840	1

FIGURE 3.14: The same as in Fig. 3.12 but taking into account the FERMI-LAT data between 2 GeV $\lesssim E \lesssim$ 100 GeV [71], that extends the dof to 27. The background parameters fitted by these data are $A^{(\gamma)} = (4.44 \pm 0.34) \cdot 10^{-7} \mathrm{cm}^{-1}\mathrm{s}^{-1/2}$ and $\Gamma = 2.63 \pm 0.02$, in agreement with the spectral index for this spectral region already found when the FERMI-LAT data are fitted with a broken power law [71]. The quality of the fit is evident with a $\chi^2/dof = 0.75$. From this interpretation of the data, FERMI-LAT instruments are sensitive just to the background component of the signal.

With the fit of the parameter $A^{(\gamma)}$ (Eq. (3.7)) and by assuming a standard thermal cross section of $\langle \sigma v \rangle = 3 \cdot 10^{-26}$ cm^{3}s^{-1}, we can get an estimation of the astrophysical factor $\langle J \rangle$. We find $10^{25}\,\mathrm{GeV}^2\,\mathrm{cm}^{-5} \lesssim \langle J^{\rm NFW} \rangle \lesssim 10^{26}\,\mathrm{GeV}^2\,\mathrm{cm}^{-5}$. It implies that the boost factors $b \equiv \langle J \rangle / \langle J^{\rm NFW} \rangle$ spread on a range between two and three orders of magnitude. It is interesting to note that the enhancement of the distribution of DM required to fit the data is compatible with the expectation of N-body simulations when the effect of the baryonic matter in the inner part of GC are taken into account [15].

3.5 Conclusions

In this Chapter, we have analyzed the possibility of explaining the gamma-ray data observed by HESS from the central part of our galaxy by being partially produced by DM annihilation. The complexity of the region and the ambiguous localisation of the numerous emitting sources inside this region, seems to validate the hypothesis of a background component. We have proved that even DM annihilations into single channels of the SM provide good fits if the DM signal is complemented with a diffuse background compatible with Fermi LAT observations. The fits returns a DM mass between 15 TeV $\lesssim m_{\rm DM} \lesssim$ 110 TeV and a background spectral index between $2.6 \lesssim \Gamma \lesssim 3.7$ within 2σ. Some channels are clearly preferred with respect to others, such as the $d\bar{d}$ for the quark channels with $\chi^2/dof = 0.73$, or the W^+W^- and ZZ channels with $\chi^2/dof = 0.84$ and $\chi^2/dof = 0.85$. On the contrary, the leptonic channels are seriously disfavored. However, for a particular DM candidate, several channels can actually contribute. In this situation, the single channel analysis presented in this work can be helpful as a guide but it is necessary to know that a combination of channels can work in a qualitatively different way. In any case, it is important to take into account that in severals models, only one channel dominates the annihilation and the single channel approximation works with high accuracy.

The morphology of the signal is consistent with compressed dark halos by taking into account baryonic contraction with boost factors of $b \sim 10^3$ for typical thermal cross sections. We would like to comment that the boost factors values presented in the tables are computed under the assumption of standard thermal annihilating DM. In a general approach, i.e. for decaying DM or for dark matter candidates, whose abundances are not reached by thermal freeze-out decoupling, the boost factors do not apply. However, thermal annihilating DM is a well motivated framework, and it is interesting to interpret the amount of gamma rays observed by HESS in terms of such a hypothesis. We have adopted this approach in order to present our results. In this sense, it is important to note that the observed source of gamma rays is very localized. It implies that if they are produced by annihilation or decay of DM, they have to be related to a very dense substructure or to a compressed halo. The latter case has been obtained in different simulations that take into account baryonic effects. Indeed it has been claimed [15, 73] that when baryonic gas is taken into account, it falls to the central region, modifying the gravitational potential. This fact increases the central DM density and produces typical enhancements of $b \sim 10^3$ in gamma ray fluxes [15].

On the other hand, the DM particle that may have originated these data needs to be heavier than $\sim$ 10 TeV. These large DM masses required for fitting the HESS data are not in contradiction with the unitarity limit for thermal relic annihilation. For

example, this limit is around 110 TeV for scalar DM particles annihilating in s-wave (for $\Omega_{\rm DM}h^2 = 0.11$) [36, 79]. On the contrary, these heavy DM particles are practically unconstrained by direct detection experiments or particle colliders [80]. An interesting example of such type of DM candidates which could have high enough mass and account for the right amount of DM in the form of a thermal relic, is the branon [37, 81]. We will discuss this possibility in the next chapter.

Chapter 4

Gamma-ray search of Brane-World Dark Matter

In this Chapter, we will focus on the particular case of Brane Word Theory as a framework for DM candidates, and the possibility to detect secondary products of annihilation of two branons throughout the indirect search of gamma rays. Firstly, in Section 4.1 we discuss the gamma-ray flux expected from decay or annihilation of branon DM. Then in Section 4.2, we present the hypothesis that the gamma-ray flux observed by the HESS telescope at GC, discussed in the previous Chapter 3, may be originated by branon DM annihilation events. Finally, we will check the compatibility of such hypothesis with available constraints given by Cherenkov and Satellite telescope observations of dSphs Galaxies and GC in Section 4.3. This Chapter is based on [37] and [69].

4.1 Brane-World Dark Matter

In order to compute the final spectrum of cosmic rays coming from branon, we need to know the total annihilation cross section and the corresponding branching ratios into SM particles. For branons, these cross sections only depend on the spin and mass of the particle, and the expressions for branons thermal average annihilations $\langle \sigma_i v \rangle$ in different SM particles channels, i.e., in Dirac fermions, massive gauge field, massless gauge field and complex scalar field were calculated in [82]. For instance, the s-wave for non-relativistic branons annihilating into a Dirac fermion ψ with mass m_ψ, is given by:

$$\langle \sigma_\psi v \rangle \;=\; \frac{1}{16\pi^2 f^8} m_{\rm DM}^2 m_\psi^2 \left(m_{\rm DM}^2 - m_\psi^2\right) \sqrt{1 - \frac{m_\psi^2}{m_{\rm DM}^2}}\,; \tag{4.1}$$

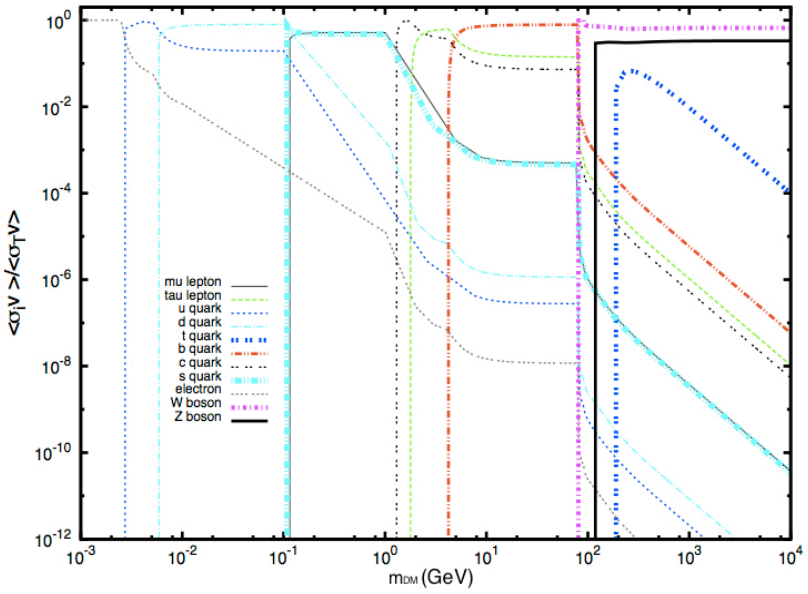

FIGURE 4.1: Branon annihilation branching ratios into SM particles. In the case of heavy branons the main contribution to the photon flux comes from branon annihilation into W^+W^- and ZZ. The contribution from heavy fermions, i.e. annihilation into top-antitop can be shown to be subdominant. On the contrary, if $m_{\rm DM} < m_{W,Z}$, the annihilation into W or Z bosons is kinematically forbidden and it is necessary to take into account the rest of channels, mainly annihilation into the heaviest possible quarks.

For a massive gauge field Z, of mass m_Z, it reads:

$$\langle \sigma_Z v \rangle \;=\; \frac{1}{64\pi^2 f^8} m_{\rm DM}^2 \left(4\, m_{\rm DM}^4 - 4\, m_{\rm DM}^2\, {m_Z}^2 + 3\, {m_Z}^4\right) \sqrt{1 - \frac{{m_Z}^2}{m_{\rm DM}^2}}\,; \tag{4.2}$$

whereas for a massless gauge field γ, the s-wave is zero:

$$\langle \sigma_\gamma v \rangle \;=\; 0; \tag{4.3}$$

and, finally, for a (complex) scalar field Π with mass m_Π:

$$\langle \sigma_\Pi v \rangle \;=\; \frac{1}{32\pi^2 f^8} m_{\rm DM}^2 \left(2\, m_{\rm DM}^2 + {m_\Pi}^2\right)^2 \sqrt{1 - \frac{{m_\Pi}^2}{m_{\rm DM}^2}}\,. \tag{4.4}$$

It is worth noting that there would be a gamma ray line from direct annihilation into photons since branons couple directly to them, producing a monochromatic signal at the energy equal to the branon mass. However, this annihilation takes place in d-wave channel and it is highly suppressed. The annihilation branching ratios into SM channels are shown in Fig. 4.1.

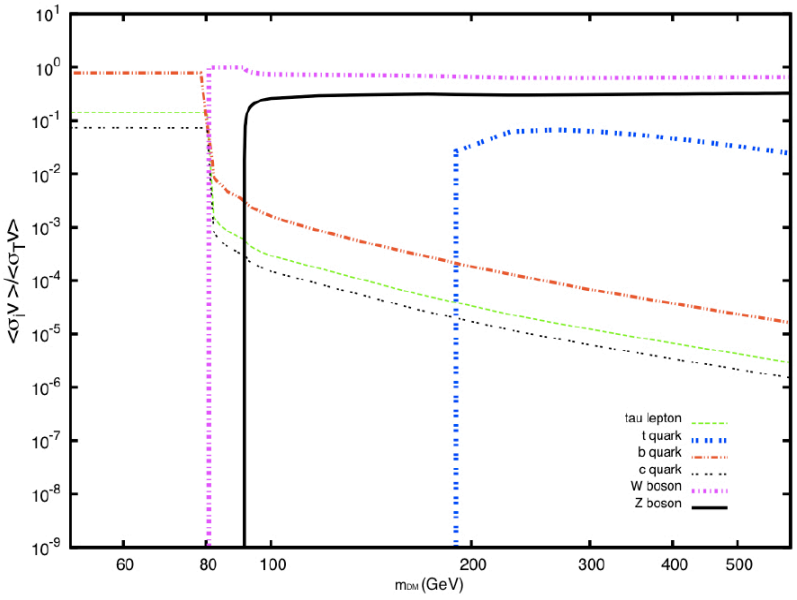

FIGURE 4.2: The same as in Fig. 4.1 for heavy branon with $m > 50$ GeV.

4.2 Branon DM hypothesis for HESS J1745.6-290 gamma-ray source.

For a particular DM candidate, several channels can actually contribute to the final flux of secondary cosmic rays. In this situation, the analysis of the gamma-ray fluxes showed in Chapter 3 can be helpful as a guide but not determinant, since a combination of channels can work in a different way.

In the case of heavy branons, the main contribution to the photon flux comes from branon annihilation into ZZ and W^+W^- (Fig. 4.2). The contribution from heavy fermions, i.e., annihilation into top-antitop can be shown to be subdominant [82]. In this case, the produced high-energy gamma photons could be in the range detectable by Atmospheric Cherenkov Telescopes (ACTs) such as MAGIC [83, 84], that is between 30 GeV-10 TeV.

On the contrary, if $m_{\rm DM} < m_{W,Z}$, the annihilation into W or Z bosons is kinematically forbidden and it is necessary to take into account the rest of channels, mainly annihilation into the heaviest possible quarks [85] as can be seen in Fig. 4.1. In this case, the photon fluxes would be in the range detectable by space-based gamma ray observatories [82] such as EGRET [86] and FERMI [87, 88], with better sensitivities around 30 MeV-300 GeV.

For masses over 1 TeV, the main contribution to the photon spectra comes from branons annihilating into gauge bosons ZZ, and W^+W^-. They produce approximately the same

Branons	$m_{\rm DM}$ (TeV)	$C^{(\gamma)}$ (10^{-2} GeV cm^{-1}s$^{-1/2}$)	$B^{(\gamma)}$ (10^{-4} GeV$^{-1/2}$cm^{-1}s$^{-1/2}$)	Γ	χ^2/ dof	$\Delta\chi^2$	b
W+Z	50.6 ± 4.5	1.57 ± 0.13	5.27 ± 2.32	2.80 ± 0.15	0.84	2.6	4843 ± 1134

TABLE 4.1: Best fit parameters for branon annihilation. The dominant channels contributing are W^+W^- and ZZ. In the second column $C^{(\gamma)\,2} \equiv \Delta\Omega\,\langle J_{(a)}\rangle_{\Delta\Omega}/(8\pi m_{\rm DM}^2)$. b is computed with the model fitted cross-section to WMAP data [89]: $\langle\sigma v\rangle = (1.14 \pm 0.19)\cdot 10^{-26}$ cm^{3}s^{-1}. Rest of parameters are as in Table I.

amount of Z, W^+ and W^- since $\langle\sigma_{W^+W^-}v\rangle \simeq 2\langle\sigma_{ZZ}v\rangle \simeq m_{\rm DM}^6/(8\pi^2 f^8)$, where f is the brane tension scale (and we are assuming only one branon species [81]). As the rest of channels can be neglected, and the W and Z channels produce very similar photon fluxes, the results for the fit with the branon model lead to very similar results to those obtained by considering both channels individually (see Table 3.1). In this case, as there is a particle model behind, we can deduce the coupling that leads to the DM abundance consistent with WMAP observations [89]: $f = 27.5 \pm 2.4$ TeV, and we can compute the thermal averaged cross-section: $\langle\sigma v\rangle = \sum_{i=W,Z}\langle\sigma_i v\rangle = (1.14\pm0.19)\cdot 10^{-26}$ cm^{3}s^{-1}, that agrees with the expected order of magnitude.

4.3 Detectability of Branon DM via gamma rays.

If branon represent the right candidate for the heavy DM particle, able to justify the gamma-ray flux observed by the HESS telescope from the J1745-290 source at the GC, a gamma-ray flux generated by annihilation of branon particles is expected to be observed by different types of telescopes from several astrophysical structures. Nevertheless, the prospective observation of a gamma-ray signal depends on both the detector and DM distribution in the galactic or extragalactic sources. Here we focus on both satellite and ground-based detectors of gamma-ray photons observing some dSphs galaxies and the GC.

4.3.1 Satellite experiments

Among others experiments, we will analyze EGRET and FERMI-LAT as an example of satellite telescope.

EGRET

EGRET (Energetic Gamma-Ray Experiment Telescope) has detected gamma rays in the interval 0.02 to 30 GeV. This telescope was carefully calibrated at SLAC with a quasi mono-energetic beam in the energy range of 0.02 to 10 GeV. Although the energy

range was extended up to higher energies (30 GeV) by using Monte Carlo simulations, we have used only data below 10 GeV [86] due to the associated larger uncertainty at high energy. The angular resolution was energy dependent, with a 67% confinement angle of 5.5° at 100 MeV, falling to 0.5° at 5 GeV on axis. The energy resolution of EGRET was 20-25% over most of its range of sensitivity. Absolute arrival times for photons were recorded with approximately 50 μs accuracy. The overall normalization error is usually quoted as 15 % [86].

FERMI

The Large Area Telescope (LAT) is the principal scientific instrument on the FERMI Gamma Ray Space Telescope spacecraft, originally called the Gamma-Ray Large Area Space Telescope (GLAST). The LAT is an imaging high-energy gamma ray telescope covering the energy range from about 20 MeV to more than 300 GeV [87]. The LAT's field of view covers about 20% of the sky at any time, and it scans continuously, covering the whole sky every three hours. The LAT measures the tracks of the electron and positron that result when an incident gamma ray undergoes pair-conversion, preferentially in a thin, high-Z foil, and measures the energy of the subsequent electromagnetic shower that develops in the telescope calorimeter. The development of the reconstruction relies heavily on the Monte Carlo simulation of the events. The background model for this device includes cosmic rays and Earth's albedo gamma rays within the energy range 10 MeV to 1 GeV. Particles that might either make non astrophysical gamma rays and/or need to be rejected as background are included. The model does not include X-rays nor soft gamma rays that might cause individual detectors within the LAT to be activated [87, 88]. Several investigations [90] have looked for potential DM subhalos targets for ACTs and FERMI at energies higher than 100 GeV claiming that multi-wavelength observations could play an essential role in DM indirect searches.

4.3.2 Ground-based experiments

The measurement of very high-energy gamma rays using very large ground-based Cherenkov telescopes is an important addition to the variety of experiments at the interface between particle physics, astrophysics and cosmology.

MAGIC

The MAGIC experiment for ground-based gamma ray astronomy is the largest of the third generation Cherenkov telescope experiments, located at the La Palma (Canary

Islands) observatory, 2200 m above sea level. Presently, it consists of a system of two telescopes operating in a stereoscopic mode. The stereoscopic system allows for improved background rejection specially at low energies (and therefore high sensitivity), improved energy and angular resolution, and a low energy threshold. However, in our study, we are interested in current constraints from analyses already performed with observed data. This data were collected with the initial setup (MAGIC-I) consisting of a single telescope (focal length of 17 m). The threshold for gamma detection is around 60-70 GeV with classical photomultiplier tubes (PMTs); future high-quantum efficiency red-extended PMTs are expected to achieve a lower threshold. MAGIC has the best light collection that has been attempted so far: the largest mirror with an active surface of 234 m^2, combined with the best available photomultiplier tubes that can be obtained, of a quantum efficiency around 30%. As a result, MAGIC is more sensitive to electromagnetic showers of lower energy, and does much to close the gap existing between satellite gamma ray detectors (that can go up to 10 GeV energy) and Cherenkov telescopes (that presently start at energies higher than 100 GeV). MAGIC-I has a threshold trigger energy of ~ 50 GeV, and an analysis threshold of ~ 70 GeV at small zenith angle, which also permits to observe sources with higher redshift than in the past [83, 84].

CTA

We are also interested in estimating the prospects for future experiments as the Cherenkov Telescope Array (CTA) project, that is an initiative to build the next generation of ground-based very high energy gamma-ray instruments. Current systems of Cherenkov telescopes use at most four telescopes, providing best stereo-imaging of particle cascades over a very limited area, with most cascades viewed by only two or three telescopes. An array of many tens of telescopes will allow the detection of gamma-ray induced cascades over a large area on the ground, increasing the number of detected gamma rays dramatically, while at the same time providing a much larger number of views of each cascade. This results in both improved angular resolution and better suppression of cosmic-ray background events. The CTA will explore our Universe in depth at gamma rays of Very High Energy (VHE), i.e., $E > 10$ GeV and investigate cosmic non-thermal processes, in close cooperation with observatories operating at other wavelength ranges of the electromagnetic spectrum, and those using other messengers such as cosmic rays and neutrinos. The design foresees a factor of $5 - 10$ improvement in sensitivity in the current VHE gamma ray domain of about 100 GeV to some 10 TeV, and an extension of the accessible energy range from well below 100 GeV to above 100 TeV [91].

Draco dSph				
Experiment	EGRET	FERMI	MAGIC-I*	CTA
A_{eff}	$10^3(*)$ 1.5×10^3	10^4	5×10^8	10^{10}
$\Delta\Omega$	10^{-3}	$9\times10^{-5}(*)$ 10^{-5}	10^{-5}	10^{-5}
t_{exp}	1 yr		40 h	50 h
Φ_{Bg}	$3.3\times10^{-7}(*)$ 6.7×10^{-7}		$1.9\times10^{-7}(**)$	$\sim10^{-7}(**)$
$\Phi_\gamma^{(5)}$	$1.04\times10^{-6}(*)$ 9.15×10^{-7}	$1.14\times10^{-6}(*)$ 8.55×10^{-6}	1.00×10^{-7}	1.25×10^{-8}
$\Phi_\gamma^{(2)}$	$2.78\times10^{-7}(*)$ 2.84×10^{-7}	$2.97\times10^{-7}(*)$ 1.75×10^{-6}	3.54×10^{-8}	4.83×10^{-9}
$\langle J\rangle_{\Delta\Omega}$	0.1	7.2		
$N_{(5)}^{(\gamma)}\langle\sigma v\rangle/m_{\rm DM}^2$	$1.31\times10^5(*)$ 1.15×10^5	$1.98\times10^3(*)$ 1.49×10^4	1.75×10^2	21.8
$N_{(2)}^{(\gamma)}\langle\sigma v\rangle/m_{\rm DM}^2$	$3.49\times10^4(*)$ 3.57×10^4	$5.19\times10^2(*)$ 3.06×10^3	61.8	8.42

TABLE 4.2: $\Phi_\gamma^{(5)}$ or $\Phi_\gamma^{(2)}$ ($\mathrm{cm^{-2}s^{-1}sr^{-1}}$), where superscripts (5) and (2) denote the estimated minimum detectable flux at 5σ or 2σ, for different detectors: EGRET, FERMI, MAGIC-I and CTA associated with Draco. The first three are current constraints, whereas the last one is a prospect for its sensitivity. A_{eff} ($\mathrm{cm^2}$) denotes the typical effective area, $\Delta\Omega$ (sr) the angular acceptance, t_{exp} (s) the exposure time and Φ_{Bg} ($\mathrm{cm^{-2}s^{-1}sr^{-1}}$) the estimated total background flux. In order to obtain $N_{(2)}^{(\gamma)}\langle\sigma v\rangle/m_{\rm DM}^2$ ($\mathrm{cm^3s^{-1}}$), we have used Eq. (3.5) with the astrophysical factor $\langle J\rangle_{\Delta\Omega}(10^{23}\mathrm{GeV^2cm^{-5}sr^{-1}})$ given in [93] assuming a NFW profile for the DM distribution. Most part of the data are taken from [93], except for the values marked with a single asterisk (*) which are obtained from Ref. [94]. The Φ_{Bg} signed with double asterisk (**) is calculated by means of the Eq.(4.7) with $\epsilon = 0.01$ for both MAGIC-I and CTA projects [93, 94].

4.3.3 Analysis and results

Among other possibilities, the GC and dSphs are the best targets for DM indirect search. The astrophysical part $\kappa_{\gamma,\nu} \equiv \langle J_{(a)}\rangle_{\Delta\Omega}$ of the gamma-ray flux (2.3) ($\eta_\gamma = 1$, $a = 1$ and $\zeta_i = \langle\sigma_i v\rangle$) of each target depends upon the DM density. This factor is not very well known and introduces the most important uncertainties in these indirect detection analyses. A classic approach uses a NFW profile. This profile is in good agreement with cold DM simulations and it allows an easy comparison with previous studies since it has been used by many authors. For this reason, we have assumed this profile (see Eq. (1.13)) for the Draco, Sagittarius and Canis Major dSphs and for the GC [77].

On the other hand, we have assumed for SEGUE 1 an Einasto profile (Eq. (1.13)) with scale density $\rho_s = 1.1\times10^8 M_\odot\,\mathrm{Kpc}^{-3}$, scale radius $r_s = 0.15\,\mathrm{Kpc}$ and index $n_s = 3.3$, since it is more consistent with observations [83]: Very recent observations [92] of SEGUE

Sagittarius dSph			
Experiment	EGRET	FERMI	CTA
A_{eff}	1.5×10^3	10^4	10^{10}
$\Delta\Omega$	10^{-3}	$\sim 10^{-5}$	10^{-5}
t_{exp}	1 yr		100 h
Φ_{Bg}	3.18×10^{-6}		2.7×10^{-4}(**)
$\Phi_\gamma^{(5)}$	1.59×10^{-6}	1.04×10^{-5}	1.25×10^{-6}
$\Phi_\gamma^{(2)}$	5.62×10^{-7}	2.74×10^{-6}	4.83×10^{-9}
$\langle J \rangle_{\Delta\Omega}$	1.3	36.9	
$N_{(5)}^{(\gamma)} \langle \sigma v \rangle / m_{\rm DM}^2$	1.53×10^4	3.53×10^3	4.25
$N_{(2)}^{(\gamma)} \langle \sigma v \rangle / m_{\rm DM}^2$	5.44×10^3	9.33×10^2	1.64

TABLE 4.3: The same as Table 4.2 for the observation of Sagittarius. The first two columns related to EGRET and FERMI are current constraints whereas the last one corresponding to CTA is an estimation of its possible sensitivity.

Canis Major dSph			
Experiment	EGRET	FERMI	CTA
A_{eff}	1.5×10^3	10^4	10^{10}
$\Delta\Omega$	10^{-3}	$\sim 10^{-5}$	10^{-5}
t_{exp}	1 yr		100 h
Φ_{Bg}	3.87×10^{-6}		2.7×10^{-4}(**)
$\Phi_\gamma^{(5)}$	1.71×10^{-6}	1.08×10^{-5}	1.25×10^{-8}
$\Phi_\gamma^{(2)}$	6.15×10^{-7}	2.94×10^{-6}	4.82×10^{-9}
$\langle J \rangle_{\Delta\Omega}$	8.3	139.9	
$N_{(5)}^{(\gamma)} \langle \sigma v \rangle / m_{\rm DM}^2$	2.60×10^3	9.68×10^2	1.12
$N_{(2)}^{(\gamma)} \langle \sigma v \rangle / m_{\rm DM}^2$	9.32×10^2	2.64×10^2	0.43

TABLE 4.4: The same as Table 4.3 for the observation of Canis Major.

1 (considered by many authors as possibly the most DM dominated satellite galaxy known in our galaxy) by MAGIC found no significant gamma-ray emission above the background when taking into account the spectral features of the gamma-ray spectrum of specific DM models in a supersymmetric scenario.

In any case, both the modification of the density profile and the introduction of substructures just include an additional constant in the analysis that is easy to update. With our assumptions, the values of the astrophysical factor for each source are reported in Tables 4.2-4.6.

4.3.4 Minimun detectable flux

We can estimate the minimum detectable flux Φ_γ taking into account the total number of observed gamma rays. Due to the uncertainties of these kind of analysis, it is usual to demand a significance of at least 5σ. For an observed target presenting: exposure time of t_{exp} seconds, instrument of effective area A_{eff} and angular acceptance $\Delta\Omega$, the significance of the detection exceeding 5σ (or alternatively 2σ) is:

$$\frac{\Phi_\gamma \sqrt{\Delta\Omega\, A_{eff}\, t_{exp}}}{\sqrt{\Phi_\gamma + \Phi_{Bg}}} \geq 5\ (2). \tag{4.5}$$

The DM annihilation flux Φ_γ and the background flux Φ_{Bg} are given in $\mathrm{cm}^{-1}\mathrm{s}^{-1}\mathrm{sr}^{-1}$ [93]. The evaluation of the background Φ_{Bg} and its value depends both on the experiment and on the source. In the case of satellite experiments, the diffuse gamma-ray flux from astrophysical sources is the only contribution to the background depending on the location of the source [93]. The background for FERMI is assumed to be the same as for EGRET [93–95]:

$$\frac{\mathrm{d}N_{Bg-a}}{\mathrm{d}E} \approx \mathcal{N}\,\mathrm{GeV}^{-1}\mathrm{cm}^{-2}\mathrm{s}^{-1}\mathrm{sr}^{-1} \times \left(\frac{100\,\mathrm{GeV}}{E_{Bg}}\right)^{2.1}, \tag{4.6}$$

and the exposition time $t_{exp} = 1$ yr, common for the satellite experiments. We have chosen the spectral index 2.1 since it is the most conservative value (see [93] or [95] for the particular values of $\mathcal{N}$ for the particular targets). In reality, the effective area of any detector depends on the particular energy at which it operates. Eq. (4.5) assumes a constant value and it is the main approximation of this equation. We will assume a typical effective area for EGRET of 1.5×10^3 cm^2, whereas we will use $A_{eff} = 10^4$ cm^2 for FERMI. On the contrary, the angular acceptance is much larger for EGRET: $\Delta\Omega = 10^{-3}$ sr, than for FERMI: $\Delta\Omega = 10^{-5}$ sr [86–88, 94].

In the case of ground-based experiments, besides the above diffuse gamma-ray flux, there are two other sources of background: the hadronic and the cosmic-ray electrons. In any case, the hadronic source dominates at high energies for which the ground-based experiments are sensitive. Taking into account the data observed by the Whipple 10 m telescope, it is possible to find a estimation for this background rate [94, 96]:

$$\frac{\mathrm{d}\Phi_{Bg-h}}{\mathrm{d}E} \approx \epsilon \times 10^{-5}\,\mathrm{GeV}^{-1}\mathrm{cm}^{-2}\mathrm{s}^{-1}\mathrm{sr}^{-1} \times \left(\frac{100\,\mathrm{GeV}}{E_{Bg}}\right)^{2.7}, \tag{4.7}$$

where we have integrated above the 100 GeV threshold of MAGIC, estimating its effective area as $A_{eff} = 5 \times 10^8\,\mathrm{cm}^2$ and its angular acceptance by $\Delta\Omega = 10^{-5}$sr. The

Galactic Center			
Experiment	EGRET	FERMI	CTA
A_{eff}	1.5×10^3	10^4	10^{10}
$\Delta\Omega$	10^{-3}	$\sim 10^{-5}$	10^{-5}
t_{exp}	1 yr		100 h
Φ_{Bg}	1.2×10^{-4}		2.7×10^{-4}(**)
$\Phi_\gamma^{(5)}$	8.23×10^{-6}	3.51×10^{-5}	1.25×10^{-8}
$\Phi_\gamma^{(2)}$	3.23×10^{-6}	1.30×10^{-5}	4.82×10^{-9}
$\langle J \rangle_{\Delta\Omega}$	26	280	
$N_{(5)}^{(\gamma)} \langle \sigma v \rangle / m_{\rm DM}^2$	3.98×10^3	1.57×10^3	0.56
$N_{(2)}^{(\gamma)} \langle \sigma v \rangle / m_{\rm DM}^2$	1.56×10^3	5.83×10^2	0.21

TABLE 4.5: The same as Table 4.3 for the observation in the direction of the Galactic Center.

SEGUE 1		
Experiment	MAGIC-I	CTA
A_{eff}	$\sim 10^8$	10^{10}
$\Delta\Omega$	10^{-5}	10^{-5}
t_{exp}	29.4 h	50 h
Φ_{Bg}	1.9×10^{-7}(**)	10^{-7}
$\Phi_\gamma^{(5)}$	3.61×10^{-7}	1.25×10^{-8}
$\Phi_\gamma^{(2)}$	1.06×10^{-7}	4.83×10^{-9}
$\langle J \rangle_{\Delta\Omega}$	11.4	
$N_{(5)}^{(\gamma)} \langle \sigma v \rangle / m_{\rm DM}^2$	3.97×10^2	13.8
$N_{(2)}^{(\gamma)} \langle \sigma v \rangle / m_{\rm DM}^2$	1.16×10^2	5.32

TABLE 4.6: The same as Table 4.2 for the observation of SEGUE 1. The first column corresponds to MAGIC-I and establishes the present constraint from this target whereas the second one estimates the CTA prospects. SEGUE 1 is the only target for which we have assumed an Einaisto profile for the DM distribution [83].

parameter ϵ which corresponds to the fraction of hadronic shower which is misidentified as electromagnetic is set to the order of 1% for MAGIC [83, 84, 94].

We are also interested in estimating the sensitivity of the next generation of ground-based VHE gamma-ray CTA instruments. Although there are still many details of the CTA project to be fixed, an important improvement in the effective area is expected thanks to the large number of telescopes in the array. We will assume a typical effective area of $A_{eff} \sim 1$ km^2, whereas the improvement in angular acceptance and background discrimination will be typically of order one [91]. In Tables 4.2-4.6 we report the technical details of each experiment, the background estimations and the resulting values of the

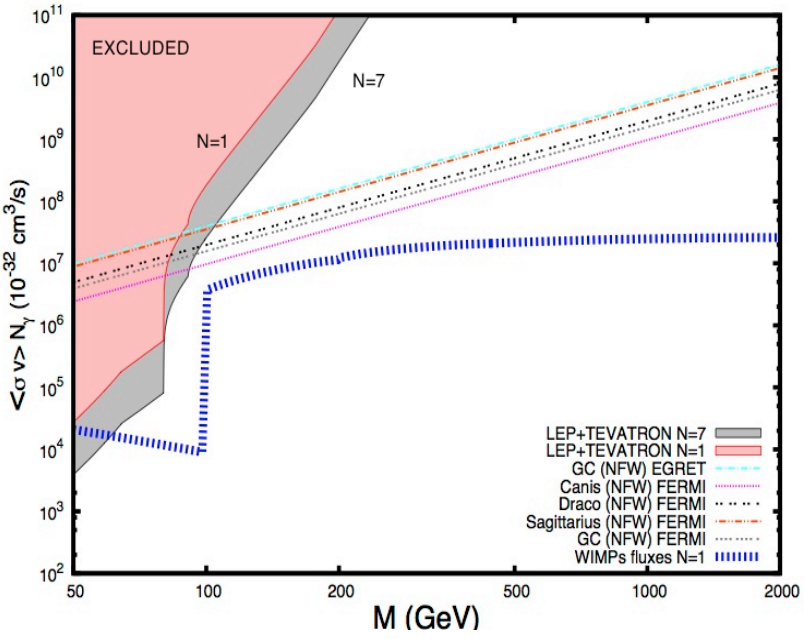

FIGURE 4.3: Sensitivity of different targets to constrain gamma rays coming from branon annihilation. Here, $M \equiv m_{\rm DM}$. The straight lines show the estimated exclusion limits at 5σ for satellite experiments (FERMI and EGRET). The blue thick line corresponds to the photon flux above 1 GeV coming from branons with the thermal abundance inside the WMAP7 [89] limits ($\Omega_{\rm CDM}h^2 = 0.1123 \pm 0.0035$). The area on the upper left corner above the corresponding lines is excluded by LEP and TEVATRON experiments for both $N = 1$ and $N = 7$, number of extra dimensions.

minimum detectable gamma-ray fluxes for the Draco, Sagittarius, Canis Major dSphs, for the GC and for SEGUE 1 respectively.

By using the estimated minimum detectable flux at 2σ or 5σ significance and the particular astrophysical factor ($J_{\langle\Delta\Omega\rangle}$) of each target, the sensitivity on $N^{(\gamma)}_{(2,5)}\langle\sigma v\rangle$ has been obtained as a function of the WIMP mass depending on the particular detector. The assumption of a constant effective area gives the typical power law behavior on the WIMP mass of this sensitivity ($N^{(\gamma)}_{(2,5)}\langle\sigma v\rangle \propto m^2_{\rm DM}$). The corresponding curves for the different targets and detectors are shown in Figs. 4.3 and 4.4. On the other hand, the theoretical value for $N^{(\gamma)}\langle\sigma v\rangle$ for branons has been obtained by integrating the differential spectrum $\sum_i \langle\sigma_i v\rangle \frac{{\rm d}\, N_i^{(\gamma)}}{{\rm d}\, E_\gamma}$ taking into account the energy threshold of 1 GeV for satellite experiments (Fig. 4.3) or 50 GeV for ACTs (Fig. 4.4). The resulting $N^{(\gamma)}\langle\sigma v\rangle$ is a function of the two branon parameters $(f, m_{\rm DM})$ and it does not depend on N (number of branon species) (Section 1.5.2). This can be easily understood due to the fact that the proportionally lower flux coming from the annihilation of a larger number of branon species, is compensated by the higher abundance that a larger number of species provides (for a fixed coupling, i.e. for a fixed value of f). Assuming that the branon relic density agrees with WMAP observations [89], it is possible to obtain $f(m_{\rm DM})$, which

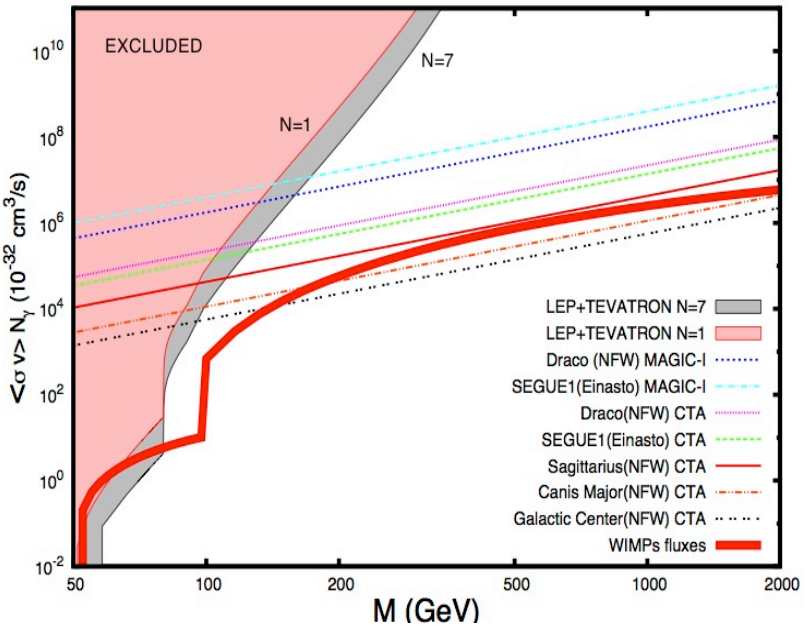

FIGURE 4.4: Same as Fig. 4.3 for ground-based detectors. In this figure, the continuous thick red line corresponds to the photon flux above 50 GeV coming from branons with the thermal abundance inside the WMAP7 [89] limits.

finally allows us to plot $N^{(\gamma)}\langle\sigma v\rangle$ as a function of the branon mass. Thus, if the integrated spectrum line is over the straight lines (which represent the sensitivity at 5σ for a particular target), a detector will be sensitive to branon annihilation coming from a particular target. We see that present experiments (EGRET, FERMI or MAGIC) are unable to detect signals from branon annihilation for the targets considered. However, as shown in Fig. 4.4, future experiments such as CTA could be able to detect gamma-ray photons coming from the annihilation of branons with masses higher than 150 GeV for observations of the GC or above 200 GeV for Canis Major.

It is important to note again that the above computations and figures are based on particular assumptions about the DM profiles and neglecting substructure contributions. Uncertainties of order one are expected for dSph satellites, but existence of boost factors of up to three orders of magnitude has been claimed for GC analyses [15]. This case has been discussed in the previous Chapter. On the other hand, these signals could be reduced for core DM profiles, that are in agreement for kinematic surveys not only of the Milky Way, but also of its dSphs [97].

4.4 Conclusions

Branons are new degrees of freedom corresponding to brane fluctuations in brane-world models. They are natural candidates for DM because they are massive fields weakly

interacting with the SM particles, since their interaction is suppressed with the fourth power of the brane tension scale f. For masses over 100 GeV, the main contribution to the photon spectra comes from branons annihilating into gauge bosons ZZ, and W^+W^-. In [36] it was shown that a branon DM with mass $m_{\rm DM} \simeq 50.6$ TeV, provides an excellent fit to HESS data. The corresponding background being compatible with Fermi-LAT data. The compatibility of its thermal abundance with the WMAP constraints [89], demands a cross section of $\langle \sigma v \rangle = (1.14 \pm 0.19) \cdot 10^{-26}$ cm^{3}s^{-1}, what is equivalent to a brane tension of $f \simeq 27.5$ TeV. In order to confirm this result, we have studied the sensitivity of different gamma-ray telescopes for the observation of indirect signals of branon DM in brane-world scenarios. Under the assumption that branons are mass degenerate, this sensitivity only depends on two parameters of the effective theory that describes the low energy dynamics of flexible brane-worlds: the brane tension scale f and the branon mass $m_{\rm DM}$. We have computed the production of photons coming from branon annihilation happening in either some dSphs or the GC, and estimated the sensitivity for these cosmic photons to be detected in different experiments. In particular, we have studied the prospective detectable flux from Draco, Sagittarius, Canis Major, SEGUE 1 and for the GC for EGRET, FERMI and the future CTA. In the case of Draco and SEGUE 1, an estimation for the MAGIC telescope is given as well. The estimated constraints show that the interesting parameter space of the theory, where the thermal branon relics account for the total non-baryonic DM content of the Universe, has not been restricted by present observations yet. Concerning the next generation of ACTs, they seem to be able to prove this thermal area of the parameter space thanks to, fundamentally, the use of a large number of telescopes which can increase significantly the effective area of detection (Fig. 4.4). With a better sensitivity, this kind of instruments could explore the highest part of the spectrum for branons heavier than 200 GeV by means of the observation of both dSphs (Canis Major in particular) and the GC. On the other hand, the estimates for the next generation of ACTs show that these types of signals could provide the first evidences of these models. We would like to point out that in this discussion, we have assumed a value astrophysical factor associated with DM only simulations. This is in contrast with the approach followed in the previous Chapter. In the same figures (4.3 and 4.4), it is possible to see the present constraints from collider experiments. These searches are complementary and probe, in general, a different area of the parameter space of the model. Indeed, these collider analyses in addition to direct detection experiments and other cosmic ray studies would be necessary to distinguish branon DM from other WIMP candidates since they are impossible to be distinguished from a potential positive result from gamma-ray observations. The analysis of other cosmic rays [98] from the GC and from other astrophysical objects is fundamental to cross check the hypotheses considered in this work. Updated analyses of this kind of

signals for heavy DM combined with simple background components is presented in the next Chapters.

Chapter 5

Neutrino Flux from the Galactic Center

As discussed in the previous Chapters 3 and 4, the observed data collected by the HESS collaboration from the J1745-290 source during the years 2004, 2005, and 2006 [58, 59] are well fitted as DM signal complemented by a diffuse background [69]. The analysis shows good agreement with DM annihilation or decay into $u\bar{u}$, $d\bar{d}$, $s\bar{s}$ and $t\bar{t}$ quark-antiquark channels and W^+W^- and ZZ boson channels. Leptonic and other quark-antiquark channels were excluded with 95.4% confidence level. The background provided by the analysis is also compatible with the Fermi-LAT data from the IFGL J1745.6-2900 source observed during 25 months [71], which is spatially consistent with the HESS J1745-290 source [78]. In any case, the fundamental nature of this gamma-ray flux is still unclear. The DM particle that originate this spectrum needs to have a mass between 15 TeV $\lesssim m_{\rm DM} \lesssim$ 110 TeV [69]. This makes highly challenging to observe these particles in direct detection experiments or particle accelerators [80]. On the contrary, complementary cosmic-rays analysis [98] from the GC and from other astrophysical objects are the most promising way to cross check the commented DM hypotheses. In particular, the analysis of neutrino fluxes from the same region can be determining. If DM annihilates or decays into SM particles producing VHE gamma-ray photons, it has to produce also VHE neutrinos. Indeed, if the dark halo properties are adjusted to explain the HESS J1745-290 data, the neutrino flux is completely determined if one concrete annihilation or decay channel is assumed.

This Chapter is organized as follows: In Section 5.1, we study the expected neutrino fluxes as indirect products of annihilating DM in the direction of the GC. Section 5.2 is devoted to discuss the flavor oscillation effects in this signal. In Section 5.3, we model

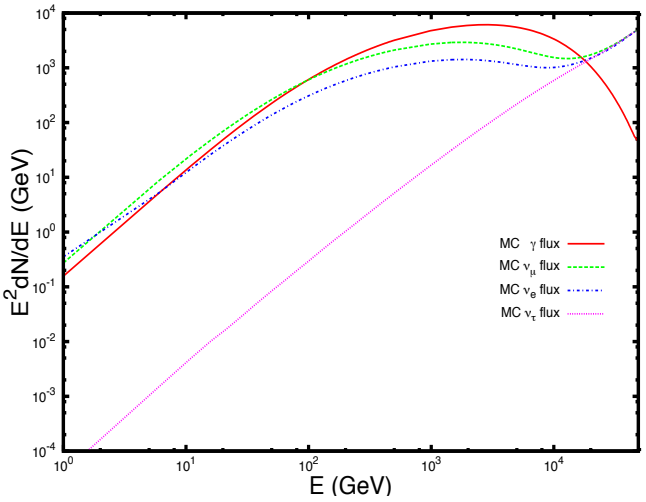

FIGURE 5.1: The gramma-ray (γ) and neutrino (ν_p) fluxes from DM annihilating into W^+W^- bosons, as generated by `PYTHIA` 8.135 and reported by [50].

the background of our analysis by taking into account the atmospheric neutrino flux observed by the IceCube experiment and we study the best configuration that may allow the detection of the corresponding neutrino signal associated with the HESS J1745-290 GC gamma-ray source. Finally, we summarize our main conclusions in Section 5.4. This Chapter is based on [99].

5.1 Neutrino flux from Dark Matter

The differential flux of neutrinos of a given flavor ν_f observed on the Earth in a particular direction can be computed as

$$\frac{d\Phi_{\nu_f}}{dE} = \sum_{p=1}^{3}\sum_{a=1}^{2}\sum_{i}^{\text{channels}} P_{fp}\cdot\frac{\zeta_i^{(a)}}{a}\frac{dN_i^{(\nu_p)}}{dE}\cdot\frac{\Delta\Omega\,\langle J_{(a)}\rangle_{\Delta\Omega}}{4\pi m_{\text{DM}}^a} \tag{5.1}$$

where $\eta_\nu = P_{fp}$ are the elements of the symmetric 3×3 matrix which takes into account the neutrino oscillation effects from the produced neutrino flavor (ν_p) generated by the DM from galactic sources to the observed neutrino flavor (ν_f) on the Earth. We shall discuss these effects in detail in the next section. m_{DM} is the mass of the DM particle. The case $a = 2$ accounts for neutrinos coming from DM annihilation with $\zeta_i^{(2)} \equiv \langle\sigma_i v\rangle$ the thermal averaged annihilation cross-section of two DM particles (assumed to be their own antiparticles) into SM particles (also labeled by the subindex i). If DM is metastable, neutrinos can be produced also by its decay. As commented in Section 2.3, in

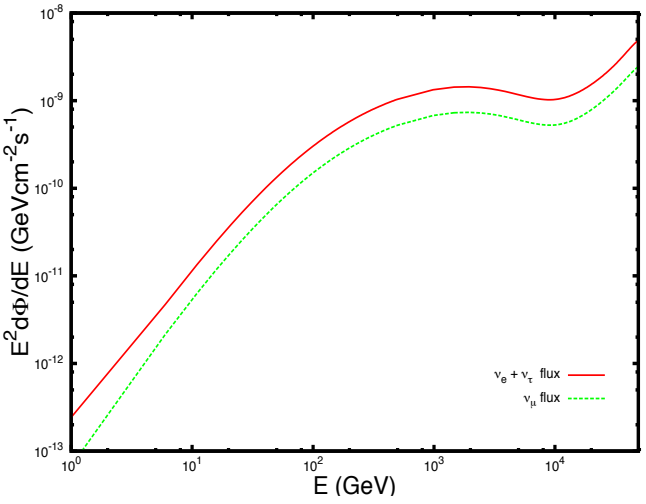

FIGURE 5.2: Neutrino differential fluxes ($\Phi_{\nu_e} + \Phi_{\nu_\tau}$ and Φ_{ν_μ}) as expected to be observed on the Earth, taking into account both neutrinos oscillations and neutrino-antineutrino total flux. We are assuming DM annihilating into the W^+W^- channel. The parameters in Eq.(5.1) are: $\langle\sigma v\rangle = 3 \times 10^{-26}\text{cm}^3\text{s}^{-1}$, $m_{\text{DM}} = 48.8$ TeV, $< J_{(2)} >_{\Delta\Omega} \simeq 4.95 \times 10^{28}\text{GeV}^2\text{cm}^{-5}$, and $\Delta\Omega = 10^{-5}$.

such a case the contribution with $a = 1$ is activated with $\zeta_i^{(1)} \equiv \langle 1/\tau_i^{\text{decay}} \rangle$ the decay width into SM particles (labeled by the same subindex i).

The number of neutrinos of flavor ν_p produced in each annihilating or decaying channel $dN_i^{(\nu_p)}/dE$, involves decays and/or hadronization of unstable products such as quarks and leptons. Because of the non-perturbative QCD effects, this requires Monte Carlo events generators [76] or fitting or interpolation functions [38]. In particular, we will use the results reported in [50]. They refer to `PYTHIA` 8.135 Monte Carlo events generator code [76] and reproduce the differential number of neutrinos produced by DM of different masses. In this Chapter, we will focus on neutrino fluxes coming from fragmentation and decays of SM particle-antiparticle pairs produced by DM annihilation. As in the analysis of the gamma-ray flux, we shall ignore DM decays, the possible production of mono energetic neutrinos, n-body annihilations (with $n > 2$), or neutrinos produced from electroweak bremsstrahlung. In particular, we will consider DM annihilation into single channels of SM particle-antiparticle pairs that are consistent with the origin of the HESS J1745-290 gamma-ray observations as we have explained.

The DM spatial distribution is encoded in the astrophysical factors $\kappa_\nu = \langle J_{(a)} \rangle$, that depend on the Ψ angle, determined by the line of observation with respect to the direction of the GC, and the total angular field of view $\Delta\Omega$ as in Eq. (2.4). The neutrino fluxes have to be averaged over the field of view of the detector, that we shall parameterize with the angle θ: $\Delta\Omega = 2\pi(1 - \cos\theta)$. The HESS Cherenkov telescopes array can be characterized typically by $\Delta\Omega_{\text{HESS}} \simeq 10^{-5}$ or $\theta_{\text{HESS}} \simeq 0.1°$. This angular resolution

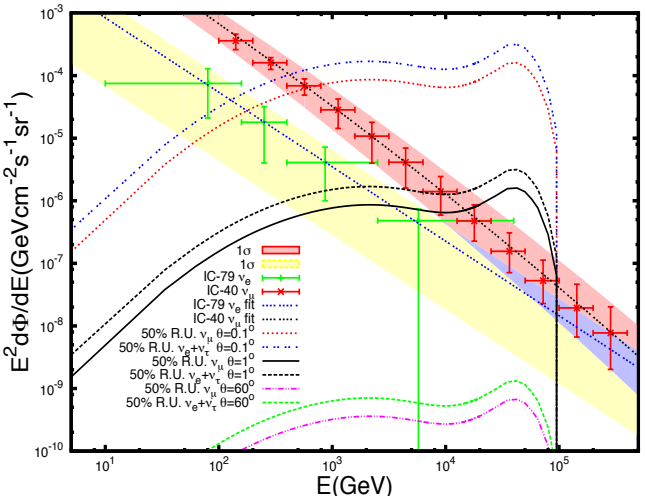

FIGURE 5.3: Expected neutrino fluxes corresponding to muon neutrinos and electron plus tau neutrinos from DM annihilating into W^+W^- bosons for an angular field of view of $\theta = 60°$, $1°$ and $0.1°$. The flux accounts for a 50% Resolution Uncertainty (R.U.) associated with a typical high energy neutrino telescope. The observed atmospheric muon by the IceCube telescope in the 40-string configuration (IC-40) and electron neutrinos by the 79-string configuration (IC-79) are also shown together with the fitting functions given by Equations (5.9) and (5.8) respectively and the corresponding shared regions at 1σ confidence level.

angle is not precise enough to resolve the J1745-290 gamma-ray morphology, which can be approximated by a point-like source. Therefore, the integration along the line of sight can be approximated by a constant value for $\theta \gtrsim 0.1°$ and the astrophysical factor given by Eq. (2.4) is fixed by fitting the HESS data:

$$\langle J_{(a)} \rangle = \langle J_{(a)} \rangle_{\rm HESS} \frac{\Delta\Omega_{\rm HESS}}{\Delta\Omega} \,, \tag{5.2}$$

where $\langle J_{(a)} \rangle_{\rm HESS}$ is the astrophysical factor which reproduces the J1745-290 gamma-ray flux, and it depends on the particular annihilating or decaying DM channel [69]. Therefore, for a neutrino telescope with $\Delta\Omega \gtrsim 10^{-5}$ the total astrophysical factor ($\langle J_{(a)} \rangle \Delta\Omega$) is constant, whereas the average ($\langle J_{(a)} \rangle$) decreases with $\Delta\Omega$ inversely. In particular, we will focus on the W^+W^- and $u\bar{u}$ annihilation channels with the standard thermal value $\langle \sigma v \rangle = 3 \times 10^{-26} {\rm cm}^3 {\rm s}^{-1}$. By taking into account the results of [69]:

$$\langle J^{W^+W^-}_{(2)} \rangle = \frac{(7.9 \pm 1.9) \times 10^{-22}}{1 - \cos\theta} \, {\rm GeV}^2 {\rm cm}^{-5} \,, \tag{5.3}$$

and

$$\langle J^{u\bar{u}}_{(2)} \rangle = \frac{(4.4 \pm 0.8) \times 10^{-22}}{1 - \cos\theta} \, {\rm GeV}^2 {\rm cm}^{-5} \,. \tag{5.4}$$

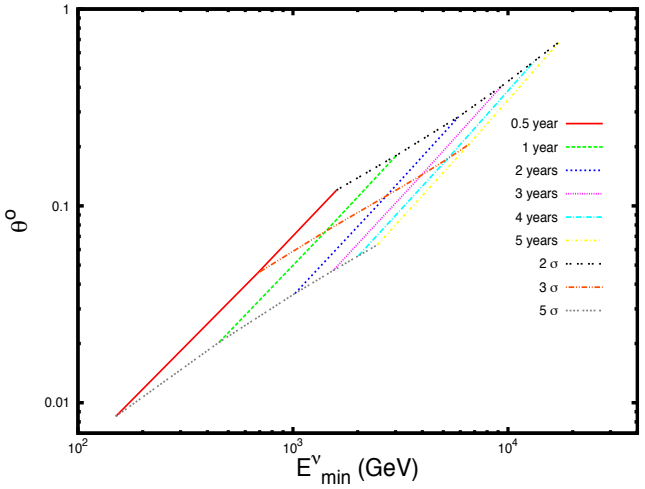

FIGURE 5.4: Combination of the angular field of view θ, minimum energy threshold and exposition time that allow to detect a muon neutrino flux signal coming from DM annihilating in the GC at 2σ, 3σ or 5σ confidence level, with a detector with 50 m^2 effective area. The annihilating mode is the W^+W^- channel, the mass of the DM particles is 48.8 TeV, the annihilation cross section is $\langle\sigma v\rangle = 3\times10^{-26}\text{cm}^3\text{s}^{-1}$ and the astrophysical factor is given by Eq. (5.3). The lowest value of $\theta \simeq 0.01^\circ$ corresponds to a 5σ confidence level with energy threshold of $E^\nu_{\text{min}} \simeq 150$ GeV and six months of exposition time. The higher the exposition time, the higher the angular resolution of the analysis needed to reduce the atmospheric background. The largest value of $\theta \simeq 0.68^\circ$ is associated with 5 years of exposition time, a statistical significance of 2σ, and an energy threshold of $E^\nu_{\text{min}} \simeq 17.42$ TeV.

5.2 Neutrino flavors and mixing

After simulating the neutrino fluxes produced at the source, one has to take into account different aspects in order to estimate the expected flux as observed on the Earth, such as neutrino oscillations and detector sensitivity to neutrino flavors. On the other hand, we shall assume that our detector is not able to discriminate between neutrinos and antineutrinos. Due to neutrino oscillations, the ratio of neutrino flavor changes during the way from the source to the observer [100]. By considering the standard three-flavor neutrino oscillation, the probability matrix P for astrophysical neutrinos traversing a vast distance is given by:

$$P(i \to j) = \sum_{a=1}^{3} |U_{ia}|^2 |U_{ja}|^2, \tag{5.5}$$

where U_{ia} are the elements of the neutrino mixing matrix [101]. For example, for the simplified case of the oscillation between only two flavors at a distance x by the source, the probability can be written as:

$$P(i \to j) = \sin^2(2\alpha^{(\nu)}_{ij}) \times \sin^2\left(\pi \frac{x}{L_\nu}\right). \tag{5.6}$$

It depends on the mixing angle $\alpha^{(\nu)}$, and the oscillation length $L_\nu = 4\pi E/\Delta m^2$, where

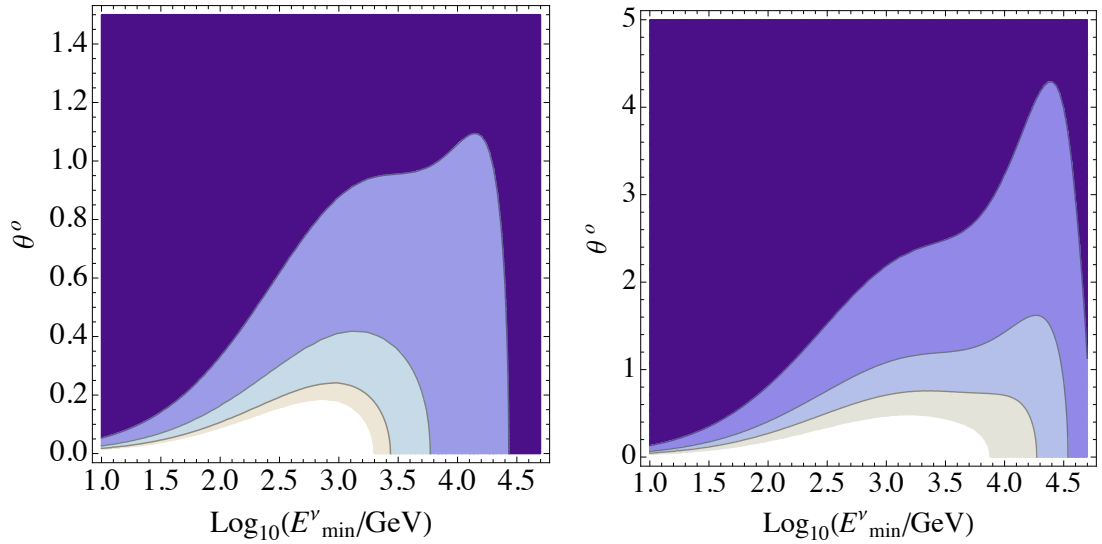

FIGURE 5.5: The Figure shows the 1σ (dark), 2σ, 3σ, 5σ (white) confidence levels contours in the case of DM annihilating into the W^+W^- channel. The factor $Af = A_{\rm eff} \times t_{\rm exp}$ is fixed in both analyses: $Af = 100\,{\rm m}^2\,{\rm yr}$ *(Left–panel)* and $Af = 600\,{\rm m}^2\,{\rm yr}$ *(Right–panel)*. The possibility to detect the neutrino flux signal above the atmospheric background depends on the energy cut $E^{\nu}_{\rm min}$ and the resolution angle.

E is the energy and $\Delta m^2 \equiv \mid m_1^2 - m_2^2 \mid$ is the squared mass difference between the two mass eigenstates. By taking into account that $\Delta m^2_{21} = (7.50 \pm 0.20) \times 10^{-5}{\rm eV}^2$, and $\Delta m^2_{32} = 2.32^{+0.12}_{-0.08} \times 10^{-3}{\rm eV}^2$ [102], we can assume that the oscillation length L_ν is small compared to the linear dimension of the source, so that the source is flavor coherent and the oscillations will be averaged out both over dimension and energy. In any case, due to the large distance of the GC compared with the dimensions of the detector, this fact does not affect the computation [100]. For a point-like source localized in the GC, we can assume that the totally averaged oscillations among the three flavors is given by a symmetric matrix of the form:

$$\begin{pmatrix} \Phi_{\nu_e} \\ \Phi_{\nu_\mu} \\ \Phi_{\nu_\tau} \end{pmatrix} = \begin{pmatrix} P_{ee} & P_{e\mu} & P_{e\tau} \\ P_{e\mu} & P_{\mu\mu} & P_{\mu\tau} \\ P_{e\tau} & P_{\mu\tau} & P_{\tau\tau} \end{pmatrix} \begin{pmatrix} \Phi^0_{\nu_e} \\ \Phi^0_{\nu_\mu} \\ \Phi^0_{\nu_\tau} \end{pmatrix} . \tag{5.7}$$

The elements $P_{\alpha\beta}$ depend on the three mixing angles $\alpha^{(\nu)}_{ij}$ and the CP phase δ (read, for example, [101]). There are important uncertainties associated to these values, but a good and simple approximation is given by assuming $\sin^2(2\alpha^{(\nu)}_{13}) = 0$ and $\sin^2(2\alpha^{(\nu)}_{23}) = 1$ (the present experimental observations constrain these angles as $\sin^2(2\alpha^{(\nu)}_{13}) = 0.095 \pm 0.010$ and $\sin^2(2\alpha^{(\nu)}_{23}) > 0.95$ [102]). In such a case, $P_{\alpha\beta}$ depends only on the $\alpha^{(\nu)}_{12}$ angle in the following way: $P_{ee} \simeq 1 - \sin^2(2\alpha^{(\nu)}_{12})/2$, $P_{e\mu} \simeq P_{e\tau} \simeq 1 - \sin^2(2\alpha^{(\nu)}_{12})/4$, $P_{\mu\mu} \simeq P_{\mu\tau} \simeq P_{\tau\tau} \simeq 1 - \sin^2(2\alpha^{(\nu)}_{12})/8$.

E^{ν}_{min}(GeV) / θ°	t_{exp}		
	2 yr	3 yr	5 yr
5σ	818 / 0.18	630 / 0.15	973 / 0.23
3σ	977 / 0.24	1102 / 0.32	1737 / 0.45
2σ	1321 / 0.42	1482 / 0.54	1811 / 0.72

TABLE 5.1: Energy threshold cut (GeV) and resolution angle in order to achieve a confidence level of 5σ, 3σ or 2σ from the muon neutrino flux for three different exposition times for DM annihilating into the W^+W^- channel with an effective area of $50\,\mathrm{m}^2$.

E^{ν}_{min}(GeV) / θ°	t_{exp}		
	2 yr	3 yr	5 yr
5σ		21 / 0.002	156 / 0.003
3σ	110 / 0.02	176 / 0.03	334 / 0.07
2σ	296 / 0.06	638 / 0.15	624 / 0.15

TABLE 5.2: Same data reported in Tab. 5.1 but for an effective area of $5\,\mathrm{m}^2$.

It means that the astrophysical flux of ν_μ and ν_τ are approximately the same independently of the flavor composition of neutrinos produced at the source. In addition, as the value of $\alpha_{12}^{(\nu)}$ is important ($\sin^2(2\alpha_{12}^{(\nu)}) = 0.857 \pm 0.024$ [102]), the oscillation effects need to be taking into account. In any case, as it can be seen in Figures 5.1 and 5.2 for the W^+W^- annihilation channel, we have checked that the neutrino flavor ratio of the fluxes observed at the Earth are very homogeneous: $\Phi_{\nu_e} : \Phi_{\nu_\mu} : \Phi_{\nu_\tau} \simeq 1 : 1 : 1$. The reason is that the most part of the neutrinos come from the charged pion decay chain: $\pi^+ \to \mu^+ + \nu_\mu \to e^+ + \nu_\mu + \nu_e + \bar{\nu}_\mu$ (or $\pi^- \to \mu^- + \bar{\nu}_\mu \to e^- + \bar{\nu}_\mu + \bar{\nu}_e + \nu_\mu$), that gives an original ratio: $\Phi^0_{\nu_e} : \Phi^0_{\nu_\mu} : \Phi^0_{\nu_\tau} \simeq 1 : 2 : 0$. This production is dominant except for the mentioned W^+W^- channel at very high energies, where the neutrinos are produced directly by the leptonic decay of the gauge bosons: $W^+ \to l^+ + \nu_l$ (or $W^- \to l^- + \bar{\nu}_l$), but it implies that even the original neutrino flux produced by the source is already homogeneous: $\Phi^0_{\nu_e} : \Phi^0_{\nu_\mu} : \Phi^0_{\nu_\tau} \simeq 1 : 1 : 1$. In both cases, it is easy to understand from the oscillation Matrix (5.7) that the three flavors arrive at the Earth with very similar fluxes.

The differential number of neutrinos for the different flavors ν_p, with $p = e$, μ and τ, as generated by the Monte Carlo event generator code, are shown in Fig. 5.1. The photon differential number is also shown for reference. As we have commented, the three flavors

are produced with the same ratio at high energies, whereas the number of ν_τ is negligible at low ones. In Fig. 5.2, we show the expected neutrino fluxes given by Eq. (5.1), as observed at the Earth, when oscillations and detection limits are taken into account. The parameters are given by the DM model independent fit of the HESS data in gamma rays characterized by Eq. (5.3) and $m_{\rm DM} \simeq 48.8$ TeV [69]. At this stage, the energy resolution of the neutrinos detector has not been yet considered.

As we have commented, we are assuming that the neutrino detector will not be able to distinguish between neutrinos and antineutrinos [103]. So the neutrino flux Φ_{ν_α} is understood to be the sum of ν_α and $\bar{\nu}_\alpha$. In addition, we shall assume that the detector will be able to distinguish muon neutrinos from electron and tau neutrinos. The later flavors give a typical showering signal, whereas the ν_μ provide a distinctive track signal. More precisely, neutrino flavors can be deduced from two different event topologies: muon tracks, related to the Cherenkov light of a propagating muon, and hadronic or electromagnetic showers. Showers are produced by neutral current (NC) interactions of any neutrino flavor, and by both ν_e and ν_τ charge current (CC) interactions. On the contrary, tracks are induced by muons from ν_μ CC interactions and ν_τ CC interactions in which the tau decay produces a muon.

5.3 Analysis

The most important source of background for highly energetic astrophysical neutrinos is given by atmospheric neutrinos and muons, depending on the direction of observation. The ν_μ and ν_e atmospheric neutrinos have been reported by IceCube [103, 104]. The electronic neutrino background has few data with important uncertainties. In this case, the ν_e atmospheric flux ($\Phi_\nu^{\rm Atm} \equiv \Phi_{\nu-Bg}$) can be well fitted by a simple power-law:

$$E^2 \times \frac{d\Phi_{\nu_e-Bg}}{dE} = A^0_{\nu_e} \left(\frac{E}{\rm GeV}\right)^{-B^0_{\nu_e}}, \tag{5.8}$$

with $A^0_{\nu_e} = 0.012 \pm 0.011$ GeV cm^{-2}s^{-1}sr^{-1} and $B^0_{\nu_e} = 1.17$. IceCube has measured the muon neutrino background with more precision, and a modified power-law fitting function is needed to reproduce the observed data accurately:

$$E^2 \times \frac{d\Phi_{\nu_\mu-Bg}}{dE} = A^0_{\nu_\mu} \left(\frac{E}{\rm GeV}\right)^{-(B^0_{\nu_\mu}+B_{\nu_\mu}\times ln(E/{\rm GeV}))}, \tag{5.9}$$

with $A_{\nu_\mu} = 0.05^{+0.01}_{-0.02}$ GeV cm^{-2}s^{-1}sr^{-1}, $B^0_{\nu_\mu} = 0.81^{-0.066}_{+0.008}$, and $B_{\nu_\mu} = 0.037$. The IceCube experimental data and both fitting functions within 1σ standard deviation are shown in Fig.5.3. The lack of ν_e atmospheric flux data and its large uncertainty

allow the power law fit, but a decreasing flux similar to the ν_μ case is expected at energies higher than 10^4 GeV. As we shall discuss, the analysis associated with the ν_e signal is not particularly interesting in this case due to its lower angular accuracy. Therefore, the overestimation of its atmospheric background at high energies does not have consequences in our results.

Our purpose is to estimate the possibilities of a general neutrino telescope to be sensitive to the neutrino signal associated to the HESS observation by assuming a DM origin. In order to be conservative, we will consider a 5σ signal (or a less restrictive 3σ or 2σ confidence level) by comparing the number of events with respect to the atmospheric background for a particular neutrino signature:

$$\chi_{\nu_i} = \frac{\Phi_{\nu_i}\sqrt{A_{\rm eff}\, t_{\rm exp}\, \Delta\Omega}}{\sqrt{\Phi_{\nu_i} + \Phi_{\nu_i}^{\rm Atm}}} = 5\,(3,\,2)\,, \tag{5.10}$$

where the effective area $A_{\rm eff}$, the solid angle $\Delta\Omega$ and the exposition time $t_{\rm exp}$ depend on the particular detector and the observation. High-energy neutrino telescopes have an effective area range between the cm^2 and the km^2, depending not only on the experiment, but also on the neutrino energy, the position of the source with respect to the telescope and the associated type of background. We can combine the track search and the shower signals in a common analysis. However, high energy muons point essentially in the same direction as the incident neutrino, and the angular resolution of high energy muon tracks is quite good, smaller than $\theta = 1^\circ$ for detectors as IceCube. This feature makes these signatures particularly interesting for the analysis of DM annihilation in the GC. For the IceCube/DeepCore detector, the GC is above the horizon, so the neutrino flux from this region contributes to the downward muon rate. However, for ANTARES [105] or the projected KM3NeT [106] detector, the GC contributes to the upward muon rate. This fact is a clear advantage since the effective area and volume are enhanced.

The electromagnetic or hadronic showers produced by neutrinos can be used as an additional signature to test the DM interpretation of the muon track signal. However, it is difficult to think that they can be used to have the first evidence of DM neutrinos coming from the GC since the current capabilities for shower angular resolution are much more limited.

As it can be observed in Fig. 5.3 and 5.7, the sensitivity to DM in the GC depends crucially on the angular resolution. The best strategy consists in reducing the angle in order to decrease the atmospheric background. In such a case, an excess at energies of the order of $\sim$ 10 TeV can be observable. In order to estimate the energy cut-off E^ν_{min}, we can restrict the total background to few events: $\sum_{i=1}^{2} \Phi_{\nu_i}^{\rm Atm} \times A_{\rm eff}\, t_{\rm exp} \simeq 1$. As we have commented, we will assume that neutrinos produced by a point-like source are

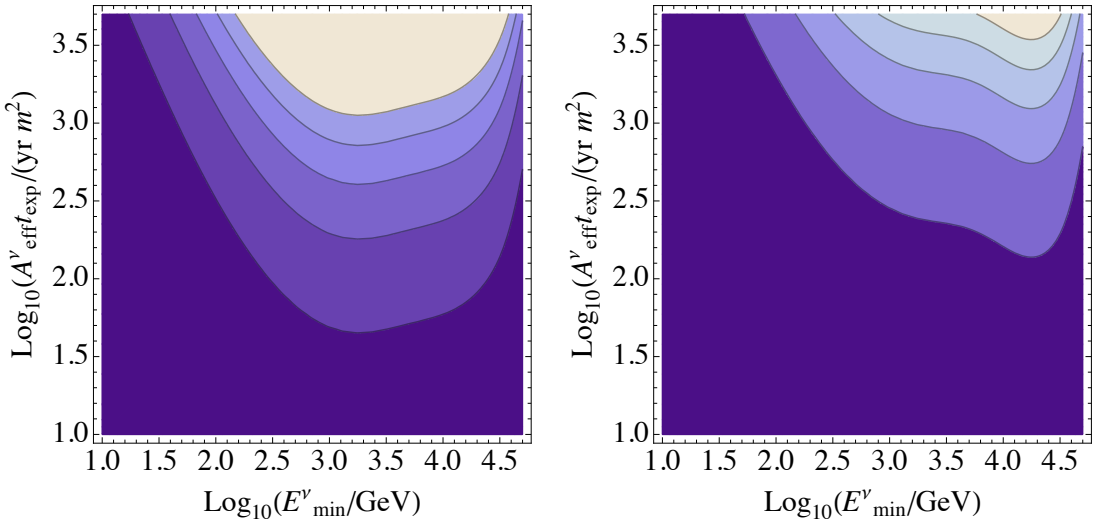

FIGURE 5.6: As in Figure 5.5, the 1σ (dark), 2σ, 3σ, 4σ, 5σ (white) confidence levels contours for DM annihilating into the W^+W^- channel are plotted. In this case, the angular field of view is fixed as $\theta = 0.6°$ *(Left–panel)* and $\theta = 1.5°$ *(Right–panel)*. Therefore, the possibility to detect the neutrino flux signal above the atmospheric background depends on the energy cut E^{ν}_{min} and the factor $Af \equiv A_{\rm eff} \times t_{\rm exp}$.

E^{ν}_{min}(GeV) / $\theta°$	t_{exp} 2 yr	t_{exp} 3 yr	t_{exp} 5 yr
5σ	274 / 0.13	336 / 0.16	420 / 0.22
3σ	398 / 0.24	479 / 0.30	524 / 0.40
2σ	490 / 0.38	839 / 0.46	552 / 0.60

TABLE 5.3: Same data reported in Tab. 5.1 but in the case of DM annihilating into $u\bar{u}$ channel with an effective area of $50\,\mathrm{m}^2$.

independent of the resolution angle of the neutrino telescope. In order to compute the number of neutrino events coming from DM, we integrate Eq. (5.1) over the observation time and energy:

$$N^{(\nu_f)}_{t_{exp}} = \int_{E^{\nu}_{\rm min}}^{\infty} dE_\nu \; \frac{d\Phi_{\nu_f}}{dE} \times A_{\rm eff}\, t_{\rm exp}\,. \tag{5.11}$$

We shall not consider the probability to detect a neutrino produced close to the detector. There is also an attenuation effect associated with neutrino interactions within the Earth's volume [107, 108]. It only affects up coming neutrinos and it will be also neglected in our estimations. By fixing the exposition time (t_{exp} = 0.5, 1, 2, 3, 4, 5 years in Figures 5.4 and 5.8), we can determine the minimum energy E^{ν}_{min} that gives a certain number of neutrino events for each observation time (in the same Figures:

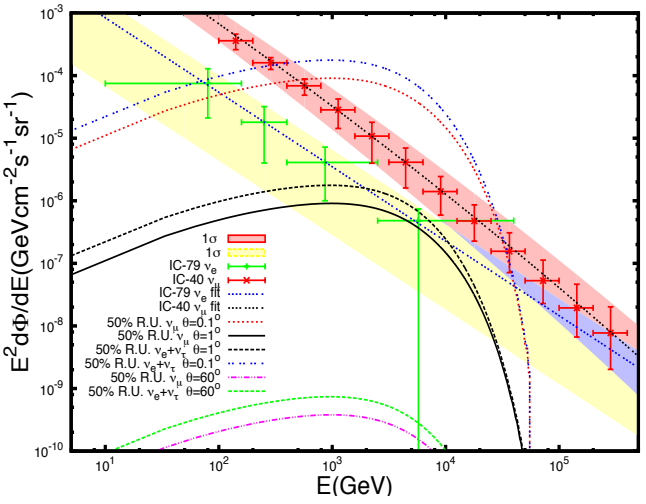

FIGURE 5.7: Same information as Fig. 5.3 but for DM annihilating into the $u\bar{u}$ channel.

$N^{(\nu_\mu)} \simeq 25$, 9, 4, which are approximately associated with 5, 3 or 2σ if the background events are negligible). On the contrary to the neutrino flux from DM, the events corresponding to the atmospheric background depend on the resolution angle of the telescope. For a given energy cut E^{ν}_{min}, we can find the maximum value for the angular field of view θ necessary to detect a negligible background (We have allowed 1 event of background for the reported values in Figures 5.4 and 5.8). We have developed this analysis for two channels qualitatively different: W^+W^- boson and $u\bar{u}$ quark-antiquark annihilation.

Following [69], DM annihilating into the W^+W^- channel requests a DM mass of around 48.8 TeV to fit the HESS gamma-ray spectra of the J1745-290 source. As we can see in Fig. 5.3, no neutrino signal produced by such kind of DM is expected with an angle of $\theta \approx 60°$. In the same figure, it is shown that the DM flux can be observable for $\theta \sim 1°$ or smaller (we are assuming a typical energy resolution of 50%).

On the other hand, Figures 5.5 and 5.6 are plotted without any constraint in the number of background events. The minimum energy thresholds for the W^+W^- channel, are reported in Tables 5.1 and 5.2 for different effective areas and exposition times. We have studied the variation of the angular field of view and the energy cut. Larger sensitivities require very accurate angular resolutions. An analysis of energies larger than $E^{\nu}_{min} \simeq 973$ GeV and an effective area of $A_{\rm eff} \simeq 50$ m^2 with an exposition time of $t_{\rm exp} \simeq 5$ yr can provide 5σ detection signal for angular resolutions of $\theta \simeq 0.23°$. Larger angular analyses of the order $\theta \simeq 0.7°$ can provide first evidences of these signatures with less statistical significance. In this case, the energy cut needs to be larger ($E^{\nu}_{min} \simeq 18$ TeV) in order to reduce the atmospheric background. In Fig. 5.5, we show the resolution angle θ as function of the minimum energy cut E^{ν}_{min} for different statistical significances

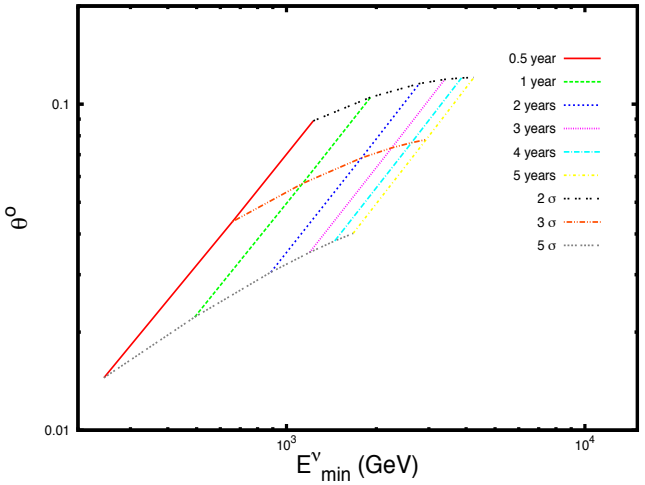

FIGURE 5.8: Same information as Fig. 5.4 but for the $u\bar{u}$ channel. In this case, the DM mass is fixed to 27.9 TeV, and the astrophysical factor is given by Eq. (5.4). The lowest value of $\theta \simeq 0.01^\circ$ corresponds to a 5σ confidence level with energy threshold of $E^\nu_{\rm min} \simeq 244$ GeV and six months of exposition time. The largest value of $\theta \simeq 0.12^\circ$ is associated with 5 years of exposition time, a statistical significance of 2σ, and an energy threshold of $E^\nu_{\rm min} \simeq 4.25$ TeV.

and exposition times $t_{\rm exp}$. Similar information about the factor $Af \equiv A_{\rm eff} \times t_{\rm exp}$ is given in Figure 5.6.

The J1745-290 gamma-ray spectrum observed by HESS can be also well fitted by DM annihilating in hadronic modes. As an example, we have analyzed the $u\bar{u}$ quark-antiquark channel, which requires a mass close to 27.9 TeV [69]. Under this assumption, we have repeated the study developed for the W^+W^- channel. In Fig. 5.7, we show the expected flux for different angular analyses. Estimations of the minimum energy cut and resolution angles depending on the exposition time and the statistical significance with negligible background are reported in Fig. 5.8. In Table 5.3 and Fig. 5.9, we present the results of the analysis for the same hadronic channel without constraining the number of background events, but fixing the effective area and exposition time combination ($Af = 100\,{\rm m}^2{\rm yr}$ in the left panel) or the resolution angle ($\theta = 0.6^\circ$ in the right panel).

5.4 Conclusions

The operation of the IceCube neutrino telescope at the South Pole, together with several counterparts at the Nothern hemisphere, such as ANTARES and NT200 presently, or the future KM3NeT and GVD, are opening a new window in our knowledge of neutrino astronomy.

Indeed, the construction of KM3NeT will imply a new substantial improvement in sensitivity corresponding to a km^3 sized detector. On the other hand, radio and airshower

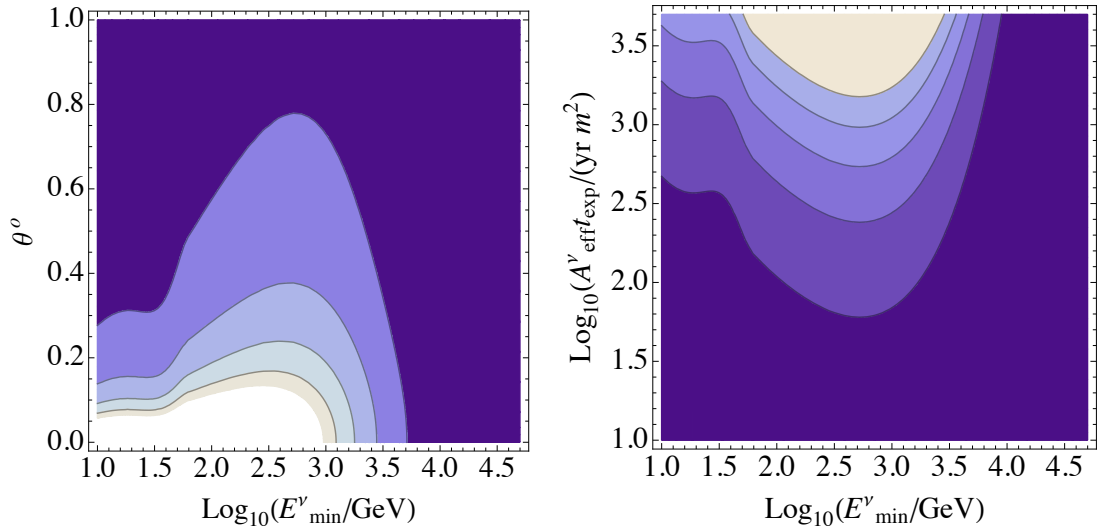

FIGURE 5.9: Confidence level contours associated to the observation of DM annihilating into the $u\bar{u}$ quark-antiquark channel at 1σ (dark), 2σ, 3σ, 4σ, 5σ (white) confidence level. *(Left–panel)*: The minimum energy cut is optimized around 1 TeV depending on the resolution angle. The exposition time and effective area are fixed to the relation: $Af \equiv A_{\rm eff} \times t_{\rm exp} \simeq 100\,{\rm m}^2\,{\rm yr}$. *(Right–panel)*: the angular field of view is fixed as $\theta = 0.6^\circ$. In such a case, the possibility to detect the neutrino flux signal above the atmospheric background demands $Af \equiv A_{\rm eff} \times t_{\rm exp} \gtrsim 100\ {\rm m}^2{\rm yr}$.

detectors, such as ANITA and the Pierre Auger observatory are sensitive to neutrinos with even higher energies. The development of neutrino detectors have increased the interest for analysing the DM nature through the production of astrophysical neutrinos as its primary source.

We have studied the prospective neutrino fluxes that should be originated by DM annihilating in the GC, in the case that the J1745-290 HESS high energy gamma rays have this origin [69]. The photon spectra is well fitted by different electroweak and hadronic channels. We have done a explicit analysis for 48.8 TeV DM annihilating in W^+W^- and 27.9 TeV DM annihilating into $u\bar{u}$ channel. In these cases, the neutrino fluxes are completely determined by assuming that the DM region is localized as it is imposed by the gamma-ray analysis. We have estimated the best combinations of energy cuts, observation times and angular resolutions of a general high-energy neutrino telescope.

For this purpose, we have used IceCube atmospheric neutrino observations as background. In particular, the data collected with exposition time of $t_{\rm exp}^{\nu_\mu} = 359$ days and $t_{\rm exp}^{\nu_e} = 281$ days for the muon and electron neutrinos, respectively [103, 104]. We have found that for DM annihilating into the W^+W^- boson channel, we need a resolution angle $0.18^\circ \lesssim \theta \lesssim 0.72^\circ$ and low energy cut-off $818\,{\rm GeV} \lesssim E_{\rm min}^{\nu} \lesssim 1811$ GeV to get a signal between 5σ and 2σ with a minimum of 2 years of exposition time and a maximum of five years for a 50 $\rm m^2$ of detector effective area. The mass associated with the $u\bar{u}$ annihilation channel is significantly smaller. It implies that the neutrino flux produced

in this case is less energetic, and more difficult to discriminate from the background. It demands a higher angular resolution ($0.13^\circ \lesssim \theta \lesssim 0.60^\circ$) and the energy cuts need to be smaller ($274\,\text{GeV} \lesssim E^{\nu}_{\text{min}} \lesssim 552$ GeV) in order to accumulate enough events. We have considered only track signal data by rejecting the muon background and taking into account the total number of events. For a binned analysis with a non-zero background and with a combined analysis of track and shower signatures, it could be possible to find better experimental configurations that should allow to detect neutrinos produced by heavy DM from the GC with worst resolution angle, smaller effective area or less exposition time.

Recently, the IceCube collaboration have reported the observation of 37 high energy neutrinos over the range 30 TeV $-$ 1 PeV at 4.1σ of confidence level, and $t_{\text{exp}} = 662$ days ($\simeq 1.8$ years). Of these events, 5 are likely originated from the GC [108]. These neutrinos seem to have an astrophysical origin, but the spectrum and direction are not compatible with the signal studied in this Chapter (the angular resolution in the muon track events is of $\theta \approx 8^\circ$). The DM signal analyzed may only account for a small part of the events, that will be more likely associated with an electroweak channel, as the W^+W^- annihilating DM model.

Chapter 6

Antiproton flux from the Galactic Center

As we described in the previous Chapters, the GC hosts large macroscopic concentrations of gas, DM and interstellar radiation, which implies an important diffuse Galactic emission in this region. In addition, the GC contains a large number of resolved and unresolved sources of cosmic-rays. Such a complex structure copiously sources different cosmic-rays from hadronic inelastic interactions, charged particle acceleration, inverse Compton scattering and Bremsstrahlung. This dense environment does not allow to reconstruct cosmic-ray fluxes from first principles without non-trivial extrapolations and important assumptions. Different studies of the GC region have found interesting features in the spectra of cosmic-ray fluxes, mainly related to gamma-ray emissions, and reported as excesses with respect to expected backgrounds. Some of them, as the one observed by the EGRET telescope in the diffuse gamma-ray emission [109, 110], has been fully explained as having a systematic origin [111] since it has not been confirmed by other data [112] as the one collected by the FERMI-LAT [61, 71]. However, it has been claimed that these new data contain another possible excess [113]. As discussed in Chapter 3, observations of the GC at higher energies have been reported by several collaborations such as CANGAROO [56], VERITAS [57], HESS [58, 59], MAGIC [60]. Also neutrino fluxes are expected to be originated from the GC. In fact, the IceCube collaboration have reported the observation of 37 high-energy neutrinos. They seem to have an astrophysical origin and 5 of them are likely originated from the GC [114] (Chapter 5).

There are different potential candidates for the primary source of new cosmic rays over the aforementioned backgrounds. In particular, there are point sources associated with the Sgr A* black hole [115, 116], supernova remnants such as the Sgr A East supernova [68], unresolved populations of millisecond pulsars [117], or other unidentified point

sources. As we have mentioned, the majority of the observations are related to gamma-ray fluxes, but it is expected that the same primary source, which constitutes the origin of the observed signal, may produce leptonic or hadronic counterparts. In addition, the production of a concrete particle will induce the production of others depending on the particular type of particle and energy. This secondary production would affect mainly the diffuse signal through hadronic emission by inelastic proton collision with the interstellar gas, inverse Compton scattering of interstellar radiation by cosmic-ray electrons and positrons, or Bremsstrahlung [112, 118].

All these effects make the analysis very challenging. In order to model the GC background, different templates have been used. However, significant systematic effects are associated with cosmic-ray density distribution and diffuse hadronic emission [119]. Indeed, there is a large ignorance about cosmic rays in this region since different populations of them are likely to be present in the GC itself and may have an important contribution to the fluxes observed at the Earth. Another fundamental issue with using the diffusion models is the set of templates employed to reproduce the morphology of the hadronic and inverse Compton Galactic emission. For example, gas column-density map templates neglect the possibility of an enhanced cosmic-ray abundance in the inner Galaxy, and the inverse-Compton template depends strongly on specific choices for the input parameters in the `Galprop` code [120].

With all the commented caveats in mind, we will assume that such an emission from the GC exists and we will estimate the possibility of detecting such signal under the assumption that it is very localized around the GC. In particular, we will focus on an antiproton emission. The $e^{\pm}$ and $p\bar{p}$ data from ATIC/PPB-BETS, PAMELA, FERMI and AMS have been largely studied. It has been speculated during the last years about the possibility of explaining the leptonic data at high energy with DM annihilation or decay. However, the data are also consistent with astrophysical primary sources [121, 122]. On the contrary, antiproton observations seem perfectly consistent with astrophysical expectations, whose origin is due to the interactions between cosmic-ray nuclei and the ISM. In this sense, antiproton data can be used to characterize diffusion models of charged particles along our galaxy, or to constrain new physics, whose antiproton flux may be identified upon the diffusion background. This is the case of DM models, whose indirect astrophysical searches are fundamental in order to investigate the constraints and the prospectives for the detection of different DM models [98, 123–126]. This is particularly true for heavy DM candidates, whose observation in direct detection experiments or particle accelerators [80] is highly challenging.

In particular, we will use the PAMELA antiproton data [127], that are in perfect agreement with *secondary* and *tertiary* antiprotons production. Astrophysical uncertainties

due to the antiproton diffusion model affect the antiproton flux at the Top Of the Atmosphere (TOA) and several standard and non-standard diffusion models can be found in the literature [49, 125]. In this Chapter, we will study the propagation of the antiproton flux emitted by a localized source at GC and the prospective antiproton flux for different emission spectra. Our aim is to study the prospective signature that could arise in the antiproton flux generated by such a source. Restrictions can be set depending on the total integrated flux and the features of the emission spectra. In Section 6.1, we will review the antiproton diffusion equation and in Section 6.2 its solution for the particular case of a point-like source at the GC. In Section 6.3, we will analyze the prospective flux at TOA produced by a fiducial power law and monochromatic antiproton spectra for such a point-like source at the GC. Section 6.4 will be devoted to the study of a TeVDM candidate able to explain the gamma-ray emission from the same region and detected by HESS [69]. Finally, we will summarize our main results in Section 6.5. This Chapter is based on [128].

6.1 Antiproton propagation

Charged cosmic-ray propagation in the Galaxy is a complex process affected by many different physical phenomena. Propagation parameters are set by B/C and sub-Fe/Fe cosmic-ray nuclei data analyses. Different configuration of parameters may be compatible with both set of data [49]. Antiproton energy losses, convention and reacceleration also affect the flux at the TOA. Energy losses are mainly due to two effects: First, ionization in neutral ISM and ionized plasma; and second, the existence of a Galactic wind. The latter phenomena is described as a constant convective wind velocity V_c, that pushes the antiprotons far away from the Galactic plane. In the middle of this plane, at z=0, a singularity takes place since V_c has opposite sign above and below the Galactic plane [49]. The Galactic wind is due to a constant flow of irregularities in the Galactic magnetic field and it cannot be neglected in the central part of the Milky Way. This fact can be deduced from observations from ROSAT and FERMI [129, 130]. However, there is not a concrete implementation of this effect for the antiproton diffusion model within this region, and we will not take it into account in our analysis. We have computed explicitly the consequences of an important increase for the convective velocity in the model and it produces a significant loss of antiprotons, mainly, in the low part of the spectrum. However, the systematic errors introduced in this way are comparable to the existing uncertainties in the diffusion model itself.

The interaction between charged particles and inhomogeneities is described by the pure space diffusion coefficient $K(E)$. This term is energy-dependent because higher energy

Model	Δ	K_0 [kpc^2/Myr]	V_c [km/s]	L [kpc]
MIN	0.85	0.0016	13.5	1
MED	0.70	0.0112	12	4
MAX	0.46	0.0765	5	15

TABLE 6.1: Value of the parameters associated with different diffusion models of the antiproton propagation within the Milky Way. The adjectives minimum, medium and maximum refer to the probability of such diffusion [131].

particles are sensitive to larger spatial scales:

$$K(E_{\bar{p}}) = K_0 v_{\bar{p}} (p/\mathrm{GeV})^{\Delta}. \tag{6.1}$$

Here, $p = (E_{\bar{p}}^2 + 2m_p E_{\bar{p}})^{1/2}$ is the antiproton ($\bar{p}$) momentum and $v_{\bar{p}} = (1 - m_p^2/(E_{\bar{p}} + m_p)^2)^{1/2}$ its velocity in natural units; $E_{\bar{p}} = E - m_p$, the $\bar{p}$ kinetic energy; and $m_p = 0.938$ GeV its mass. The parameters K_0 and Δ depend on the diffusion model, and parameterize the antiproton escape probability from the confinement volume. This volume is identified with the Galactic halo, that is described as a cylinder of radius R_D, and halo half-height L. The Galactic plane at $z = 0$ can be modelled as a thin disk of thickness $2\,h_D = 200\,\mathrm{pc}$. The antiproton number density per unit energy $f_{\bar{p}}(t, \vec{r}, E_{\bar{p}}) = dN^{(\bar{p})}/dE_{\bar{p}}$ vanishes on the surface of the cylinder at height $z = \pm L$, and at radius $r = R_D$. The larger L and R_D are, the larger the probability for particles emitted in remote sources to reach us [48, 50]. In Tab. 6.1, we show the parameters for models with minimum, medium and maximum propagation consistent with the commented observations [50, 131]. We will use these models for our analyses although they are optimized for cosmic-ray species produced following the distribution of supernova remnants in the Galaxy. The extrapolation of such models to study the GC region is another source of systematic uncertainties. Indeed, diffusion effects for antiprotons at distances around 1 pc from the GC may be negligible since they can lose their energy *in situ* by synchrotron radiation due to the very large value of the turbulent magnetic field within this region [132]. One should take into account that this hypothesis could suppress the sensitivity to antiproton fluxes originated at the GC by several orders of magnitude [133].

Standard sources and interactions with the ISM are confined to the thin disk. The $p\bar{p}$ interaction in the Galactic plane depends on the inelastic and spallation cross section. We will use [50]:

$$\sigma_{p\bar{p}}^{\mathrm{inel}}(E_{\bar{p}}) = 24.7\left[1 + 0.584(E_{\bar{p}}/\mathrm{GeV})^{-0.115} + 0.856(E_{\bar{p}}/\mathrm{GeV})^{-0.566}\right]\mathrm{mbar}\,. \tag{6.2}$$

Such an expression for the inelastic cross section $\sigma_{p\bar{p}}^{\mathrm{inel}} = \sigma_{\mathrm{ann}} + \sigma_{\text{not-ann}}$ is an extrapolation of the behaviour at low energies ($E_{\bar{p}} \lesssim 100$ GeV) that is consistent with data [49] in order to describe the interstellar $p\bar{p}$ interactions in the galactic plane, both as

proton-antiproton annihilation and proton-hydrogen scattering (*secondary* contribution) or energy loss (*tertiary* contribution). Within this approximation, we are neglecting the *tertiary* antiprotons that lose a significant fraction of their energy. At high energies the $\sigma_{\rm ann}$ tends to be smaller, so that $\sigma^{\rm inel}_{p\bar{p}} \simeq \sigma_{\text{not-ann}}$. In any case, the exact expression does not affect the final result at these higher energies in an appreciable way. This is because the *tertiary* contribution does not produce new antiprotons, but merely redistributes them towards lower energies [49, 50]. All these contributions and the *primary* source $\hat{Q}(t, \vec{r}, E_{\bar{p}})$ are transported according to the diffusion equation:

$$\frac{\partial}{\partial t}\frac{dN^{(\bar{p})}}{dE_{\bar{p}}} - K(E_{\bar{p}}) \cdot \bigtriangledown^2 \frac{dN^{(\bar{p})}}{dE_{\bar{p}}} + \frac{\partial}{\partial z}\left(sign(z) \frac{dN^{(\bar{p})}}{dE_{\bar{p}}} V_c \right) = \\ = \hat{Q}(t, \vec{r}, E_{\bar{p}}) - 2h_D \delta(z) \sigma^{\rm inel}_{p\bar{p}}\left(E_{\bar{p}}\right) \frac{dN^{(\bar{p})}}{dE_{\bar{p}}} \,. \tag{6.3}$$

We will analyze steady states defined by $\partial f_{\bar{p}}/\partial t = 0$ and $\hat{Q}(t, \vec{r}, E_{\bar{p}}) = \hat{Q}(\vec{r}, E_{\bar{p}})$. In addition, we will assume that the *primary* source can be factorized in two functions depending on its spatial distribution (Q_X) and its spectral shape (Q_E) in the following way: $\hat{Q}(\vec{r}, E_{\bar{p}}) = Q_X(\vec{r}) \cdot Q_E(E_{\bar{p}})$. In such a case, a general solution of Eq. (6.3) for the antiproton flux per unit of energy and per steradian can be written as:

$$\frac{d\Phi^{\rm Sun}_{\bar{p}}}{dE_{\bar{p}}} = \frac{v_{\bar{p}}}{4\pi}\frac{dN^{(\bar{p})}_{\rm Sun}}{dE_{\bar{p}}} = \frac{v_{\bar{p}}}{4\pi} R_{\bar{p}}(r_\odot, E_{\bar{p}}) Q_E(E_{\bar{p}}) \,, \tag{6.4}$$

where $dN^{\rm Sun}_{\bar{p}}/dE_{\bar{p}}$ is the solution at $r = r_\odot$ and

$$R_{\bar{p}}(r_\odot, E_{\bar{p}}) = \sum_{m=1}^{\infty} J_0\left(\zeta^J_m \frac{r_\odot}{R_D}\right) \exp\Big[-\frac{V_c L}{2K\left(E_{\bar{p}}\right)}\Big] \frac{\Pi_m\left(L, E_{\bar{p}}\right)}{A_m\left(E_{\bar{p}}\right) \sinh\left[S_m\left(E_{\bar{p}}\right) L/2\right]} \tag{6.5}$$

describes the Galactic antiproton production and propagation with

$$A_m\left(E_{\bar{p}}\right) = 2h_D \sigma^{\rm inel}_{p\bar{p}}\left(E_{\bar{p}}\right) + V_c + K\left(E_{\bar{p}}\right) S_m\left(E_{\bar{p}}\right) \coth\Big[S_m\left(E_{\bar{p}}\right) L/2\Big] \,, \tag{6.6}$$

$$S_m\left(E_{\bar{p}}\right) = \left(\frac{V_c^2}{K\left(E_{\bar{p}}\right)^2} + \frac{4{\zeta^J_m}^2}{R_D^2} \right)^{1/2} \,. \tag{6.7}$$

Because of the cylindrical symmetry, solutions are found in terms of Bessel functions of order n-th (J_n) and thus the properties of these Bessel functions control the behavior of these steady-state solutions. In particular, J_0 is the zero-*th* order Bessel function and ζ^J_m is its *m-th* order zero. On the other hand, Π_m depends also on the Bessel function

of first order J_1:

$$\Pi_m\left(L, E_{\bar{p}}\right) = \frac{2}{J_1^2\left(\zeta_m^J\right) R_D^2} \int_0^R dr\, r J_0\left(\zeta_m \frac{r}{R_D}\right) \times \int_{-L}^{L} dz \exp\Big[\frac{V_c(L-z)}{2K\left(E_{\bar{p}}\right)}\Big] \sinh\left[S_m\left(E_{\bar{p}}\right)(L-z)/2\right] Q_X(\vec{r})\,. \tag{6.8}$$

6.2 Antiproton point like source

As we commented so far, we would like to estimate constraints and prospectives for the detection of antiproton fluxes originated from the inner part of our Galaxy. In order to simplify the mathematical treatment, we will assume a localized source at the GC. In particular, we will model $Q_X(\vec{r})$ with a point-like spatial distribution described by a three dimensional δ-function ($\delta^{(3)}$) centered at GC:

$$Q_X(\vec{r}) = Q_X^0 \delta^{(3)}(\vec{r}) \equiv Q_X^0 \frac{1}{2\pi r} \delta^{(1)}(r)\delta^{(1)}(z)\,, \tag{6.9}$$

where Q_X^0 is a normalization constant, and we have explicitly written $\delta^{(3)}(\vec{r})$ in terms of one dimensional δ-functions ($\delta^{(1)}$) in cylindrical coordinates (r, θ, z). In such a case, Equations (6.5) and (6.8) acquire simpler expressions:

$$\Pi_m^{\delta}\left(L, E_{\bar{p}}\right) = \frac{Q_X^0}{\pi R_D^2} \frac{J_0(0)}{J_1^2\left(\zeta_m^J\right)} \exp\Big[\frac{V_c\, L}{2K\left(E_{\bar{p}}\right)}\Big] \sinh\left(S_m\left(E_{\bar{p}}\right) L/2\right)\,, \tag{6.10}$$

$$R_{\bar{p}}^{\delta}(r_\odot, E_{\bar{p}}) = \frac{Q_X^0}{\pi R_D^2} \sum_{m=1}^{\infty} \frac{J_0\left(\zeta_m^J \frac{r_\odot}{R_D}\right)}{A_m(E_{\bar{p}}) J_1^2\left(\zeta_m^J\right)}\,. \tag{6.11}$$

Therefore, the steady flux of antiprotons for a localized source located at the center of our galaxy can be written as:

$$\frac{d\Phi_{\bar{p}}^{\delta}}{dE_{\bar{p}}} = \frac{v_{\bar{p}}}{4\pi} R_{\bar{p}}^{\delta}(r_\odot, E_{\bar{p}}) Q_E(E_{\bar{p}}), \tag{6.12}$$

where $Q_E(E_{\bar{p}})$ is its characteristic energy spectrum.
Equations (6.4) and (6.12) provide the solution at the position of the Sun of the antiproton diffusion equation in the Galaxy. To get the antiproton flux at the TOA we have taken into account the solar modulation by assuming the so-called force-field or Fisk potential [50, 134]:

$$\frac{d\Phi_{\bar{p}}^{\mathrm{TOA}}}{dE_{\bar{p}}^{\mathrm{TOA}}} = \frac{p_{\mathrm{TOA}}^2}{p^2} \frac{d\Phi_{\bar{p}}}{dE_{\bar{p}}} \tag{6.13}$$

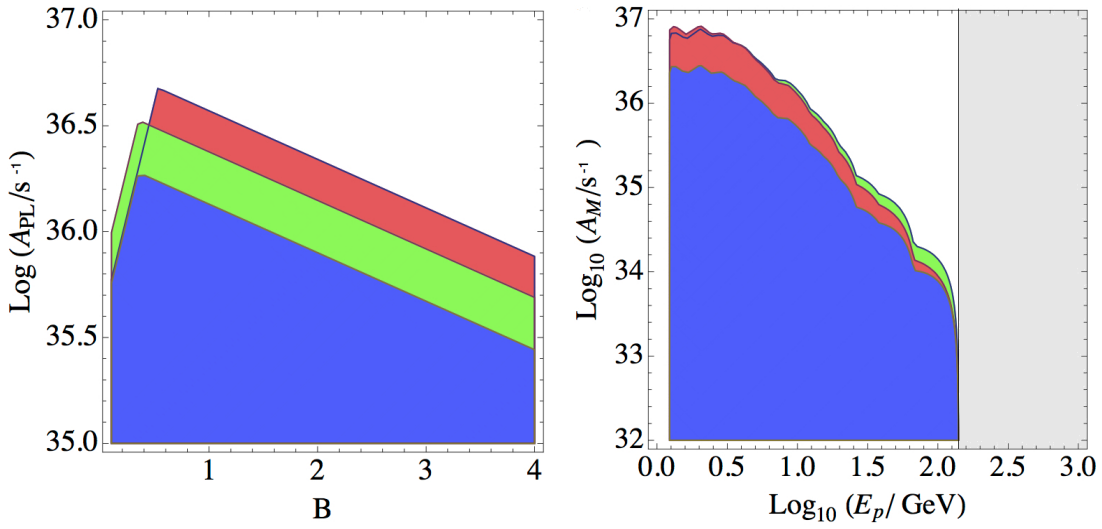

FIGURE 6.1: *(Left–panel)* Sensitivity regions derived from PAMELA data for a point-like source of antiprotons at the GC characterized by a power law emission spectrum with total amplitude A_{PL} and spectral index $-(B_{\rm PL}+1)$ (Here $B = B_{\rm PL}$). Red, green and blue regions correspond to high, medium and low diffusion models respectively. The experiment is sensitive in the upper region independently on the diffusion features of the antiprotons within the Milky Way. Low spectral indices are constrained by high energy data whereas the sensitivity related to high spectral indices is determined by low energy data. It explains the change in the slope shown by the Figure.*(Right–panel)* The same as in left-panel of this Figure but for a point-like source with monochromatic emission, $E^0_{\bar{p}}$. The figure shows the sensitivity region of the parameter space $(A_M, E^0_{\bar{p}})$ for all possible characteristic energies between 1 GeV and 130 GeV approximately. Higher emission energies are not constrained by the lack of observational data.

with $E_{\bar{p}} = E^{\rm TOA}_{\bar{p}} + |Ze|\phi_F$. As it is well known, the particular value of the Fisk potential ϕ_F in order to parameterize the solar modulation on cosmic-rays depends on the solar activity and the epoch of observation. We have used $\phi_F = 0.5$ GV since different works (for instance, read [135]) have concluded that the range between 0.1 GV and 1.0 GV is the most appropriate for the PAMELA data taking period. This effect is important at low energies. It reduces the flux of antiprotons for energies below 10 GeV, and consequently, the sensitivity of the antiproton study if the analysis is typically dominated by low-energy observations.

6.3 Energy spectra associated with general astrophysical sources

As we have commented so far, the GC hosts different types of point-like sources such as black holes, supernovas, pulsars, etc. These sources have been identified mainly by observations of their gamma-ray emissions. In order to estimate the possible observation of their antiproton counterpart, it is necessary to assume a particular spectral shape without entering into the details of the particular source. If the range of antiproton energies, that is relevant for the analysis, does not extend for many orders of magnitude,

a power law spectrum is typically a good approximation. Indeed, acceleration of cosmic-rays by Supernovae Remnats (SNR) or Pulsar Wind Nebulae (PWN) are examples of power law spectra (with a cut-off at higher energies [121]). In such a case, the antiproton source spectrum can be described in terms of two parameters:

$$Q_E^{\rm PL}(E_{\bar{p}}) = \frac{Q_E^{0-{\rm PL}}}{E_{\bar{p}}} \cdot \left(\frac{E_{\bar{p}}}{\rm GeV}\right)^{-B_{\rm PL}} , \tag{6.14}$$

where $B_{\rm PL}$ characterizes the suppression of power at high energies, and $Q_E^{0-{\rm PL}}$ normalizes the spectral flux. Therefore, we can write the total antiproton flux at TOA in terms of two constants:

$$\frac{d\Phi_{\bar{p}}^{\delta-{\rm PL}}}{dE_{\bar{p}}} = \frac{v_{\bar{p}}}{4\pi} R^{\delta}(E_{\bar{p}}) \frac{A_{\rm PL}^{(\bar{p})}}{E_{\bar{p}}} \cdot \left(\frac{E_{\bar{p}}}{GeV}\right)^{-B_{\rm PL}^{(\bar{p})}} , \tag{6.15}$$

where $A_{\rm PL}^{(\bar{p})} \equiv Q_X^0 \cdot Q_E^{0-{\rm PL}}$, takes into account the total normalization of the emission. We have compared such flux with the antiproton data observed by PAMELA. In order to be conservative, we will neglect the background contribution and assume that observations are sensitive to the signal if it produces a higher antiproton flux than the observed one at any point of the spectrum. We have checked that a complete study with the use of a realistic background as the one given in [136] gives very similar results. By following this approach, the sensitivity on the amplitude and spectral index are shown in the left-panel of Fig. 6.1 by using different diffusion models. In any case, such a dependence is not significant as it can be seen in the mentioned figure.

The power law spectral source is constrained fundamentally by the low energy data ($E_{\bar{p}} \lesssim 1$ GeV). However, in a general case, observations of antiprotons at higher energies can be more relevant. We can analyze this effect by assuming a monochromatic source. In this sense, this spectrum characterizes complementary features to the power law assumption. In particular, we will describe the spectral shape as a gaussian distribution in energy

$$Q_E^{\rm M}(E_{\bar{p}}) = \frac{Q_E^{0-{\rm M}}}{\sqrt{2\pi}\Delta_E} e^{-\frac{(E_{\bar{p}}-E_{\bar{p}}^0)^2}{2\,\Delta_E^2}} , \tag{6.16}$$

with the standard deviation given by the typical energy resolution of the device. For the PAMELA calorimeter the energy resolution is of the order of 5% of the antiproton energy ($\Delta_E \simeq 0.05 E_{\bar{p}}$) for a large spectral range. In this case, the two parameters that define the spectrum are the spectral normalization Q_E^0 and the monochromatic emission energy $E_{\bar{p}}^0$. We can perform an analogous analysis that for the power law shape. In this case, the total antiproton signal at TOA reads:

$$\frac{d\Phi_{\bar{p}}^{\delta-{\rm M}}}{dE_{\bar{p}}} = \frac{v_{\bar{p}}}{4\pi} R^{\delta}(E_{\bar{p}}) \frac{A_{\rm M}^{(\bar{p})}}{\sqrt{2\pi}\Delta_E} e^{-\frac{(E_{\bar{p}}-E_{\bar{p}}^0)^2}{2\,\Delta_E^2}} , \tag{6.17}$$

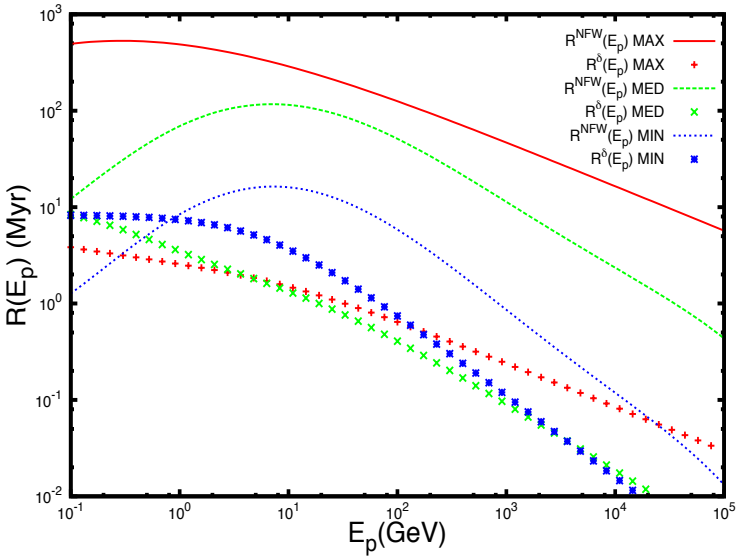

FIGURE 6.2: Dependence of the antiproton diffusion function $R(E_{\bar{p}})$, in terms of the antiproton kinetic energy $E_{\bar{p}}$, for the maximum, medium and minimum diffusion models, associated with the annihilating DM distributed by following a NFW profile ($R^{\rm NFW}(E_{\bar{p}})$ represented by a full, broken and dotted line respectively) as in [50]; and a point-like DM distribution at the GC ($R^{\delta}(E_{\bar{p}})$ represented by plus, cross and star points respectively, with $Q_X^{0-{\rm NFW}} = 2.13 \cdot 10^{60}$ m^3 sr as in [69].

where the two constants, that parameterize the signal are $A_{\rm M}^{\bar{p}} \equiv Q_X^0 \cdot Q_E^{0-{\rm M}}$, and $E_{\bar{p}}^0$. Again, the analysis shows very low dependence with the diffusion model (see right-panel of Fig. 6.1). However, in this case, all the observational data are important depending on $E_{\bar{p}}^0$, and in fact, data at high energies are most constraining since the observed antiproton flux is much more reduced. For energies higher than $E_{\bar{p}}^0 \simeq 130$ GeV (beyond the black solid vertical line), mono-energetic sources are unconstrained by PAMELA observations due to the lack of data.

6.4 Dark Matter and the HESS gamma-ray J1745-290 source

Another interesting spectral shape to be studied is the one associated with annihilation or decay of DM particles, which can cluster around a very compact region of the center of our galaxy. For example, baryonic effects may modify the gravitational potential by increasing the density in the GC [15, 73] and compressing the dark halo. This scenario is under debate [74], but it could enhance the importance of the GC region for indirect DM searches, and in particular, for the antiproton analysis. In fact, it has been shown in Chapter 3 that the J1745-290 HESS gamma-ray data [58, 59] are well fitted as a point-like DM source at the GC. Therefore, a significant flux of antiprotons is expected to be produced if the DM is the origin of this gamma-ray emission.

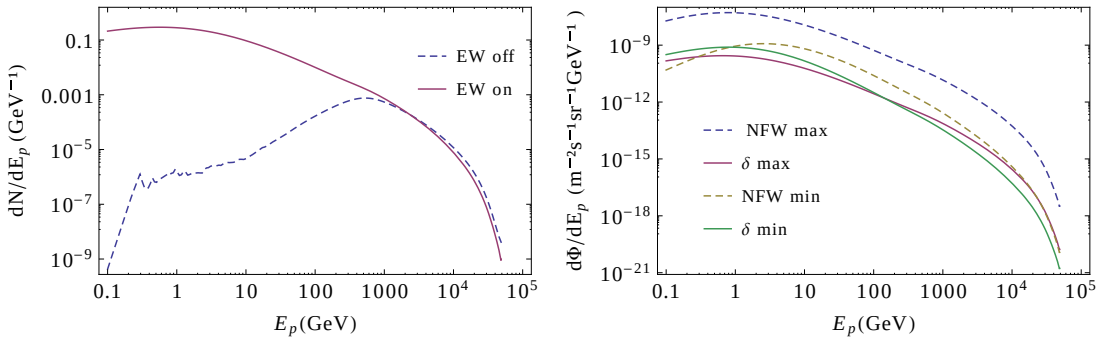

FIGURE 6.3: *(Left–panel)* Antiproton differential flux at the source for DM annihilating into W^+W^- channel with mass $m_{\rm DM} = 48.8$ TeV, before propagation. It is evident that the electroweak (EW) radiation effects cannot be neglected. *(Right–panel)* Antiproton differential flux at the TOA after propagation for 48.8 TeV DM annihilating into W^+W^- pairs. Dashed lines correspond to a spatial distribution following the standard NFW halo profile: upper and lower lines stand for the maximum and minimum propagation model, respectively. The full lines mean the same for antiproton propagation from a point-like source located at the GC with amplitude $Q_X^{0-\rm NFW} = 2.13 \cdot 10^{60}\,{\rm m}^3$ sr.

On the other hand, there is another motivation to consider this type of localized DM sources at the GC. Antiproton fluxes from DM have been largely studied in previous works [123, 124, 137], but they have been focused on the total dark halo contribution, which is dominated by local density contributions. Indeed, numerical results for general antiproton fluxes at the TOA generated by annihilation or decay of DM particles in the Galaxy halo with different propagation models have been provided in [50]. It has been shown that numerical computations of different solutions of the diffusion equation present an unavoidable singularity around the GC, because of the central steepness, which usually characterizes DM halo density profiles. In particular, in Ref. [50], this divergence is replaced by a well behaved approximation below an arbitrary critical radius of few parsecs (footnote 16 in [50]). In this sense, the addition of a DM contribution from a point-like source at the GC provides a more complete analysis (for a different way of regularizing the central DM halo singularity, read [138]).

In order to give a well established physical reference for the value of this point-like contribution, we will use the standard contribution of annihilating DM from the NFW profile [77] of our Galaxy and the gamma-ray observation in the direction of the GC. In this case, the expression for the κ-factor is given by Eq. 2.4 and $R_{\bar{p}}$ given in Eq. (6.11). In this case, the equivalent DM point-like source associated with the density distribution $\rho_\delta(\vec{r})$ is a spatial δ-function centered at the GC, which in spherical coordinates $\vec{r} \equiv (r_{spy}, \theta_{spy}, \phi_{spy})$, can be written as:

$$Q_X(\vec{r}) = Q_X^0 \delta^{(3)}(\vec{r}) \equiv Q_X^0 \frac{1}{4\pi r^2} \delta^{(1)}(r_s) \equiv \left[\frac{\rho_\delta(\vec{r})}{\rho_\odot}\right]^2 , \tag{6.18}$$

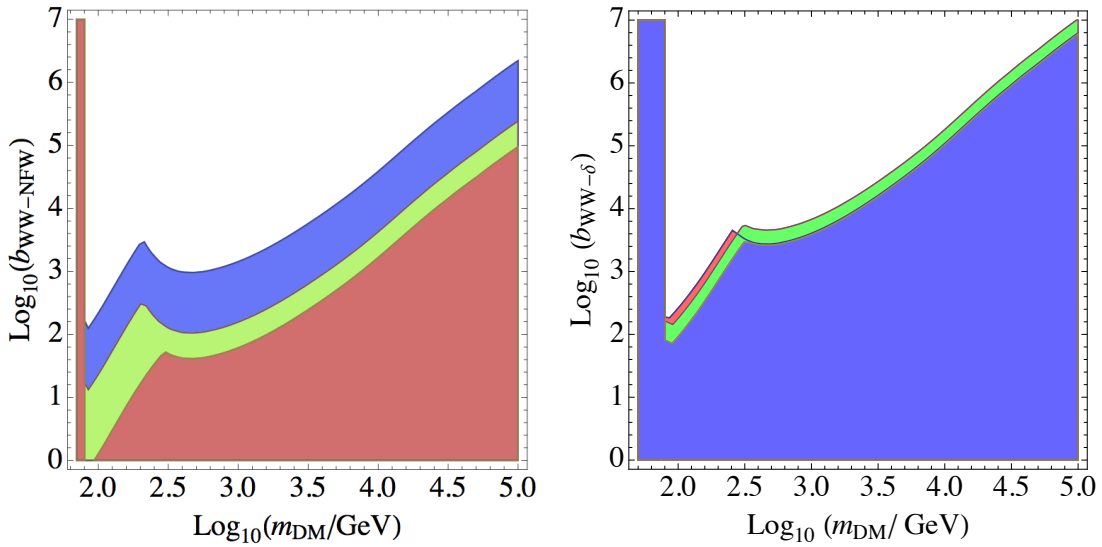

FIGURE 6.4: *(Left–panel)* Sensitivity regions from PAMELA data for DM annihilating into W^+W^- pairs distributed in a NFW halo. The experiment is sensitive to the upper (white) region independently on the diffusion features of the antiprotons within the Milky Way. On the contrary, the lower (red) region is allowed. Intermediate regions (green and blue) are allowed also for medium and minimum diffusion models, respectively (the boost factor associated to the NFW halo emission is plotted in the vertical axis $b^{WW}_{\rm NFW}$, whereas the boost factor associated to a potential contribution from the GC is zero: $b^{WW}_{\delta-\rm NFW}=0$). Figure starts near the W^+W^- direct production threshold (vertical line). The y-axis can be understood as the DM cross-section divided by the standard thermal one used for reference if annihilating DM distributed in a NFW profile with no substructure is assumed. However, the meaning of the y-axis is more general since the boost factor can be associated with a different dark halo, the presence of substructure or a possible DM decay channel. *(Right–panel)* The same as in the left-panel of this Fig. 6.4 but for a point-like DM distribution at the GC with amplitude $Q^0_X = b^{WW}_{\delta-\rm NFW}\, Q^{0-\rm NFW}_X$ (here, the boost factor associated to the NFW halo emission is taken to be zero: $b^{WW}_{\rm NFW}=0$, and the boost factor associated to the point-like source $b^{WW}_{\delta-\rm NFW}$, is plotted in the vertical axis).

where we normalize this value to the local DM density $\rho_\odot \simeq 0.3$ GeVcm^{-3}. Thus, the contribution of the point-like spatial distribution to the gamma-ray flux is

$$\langle J\rangle_{\Delta\Omega} = \frac{1}{\Delta\Omega}\int_{\Delta\Omega} d\Omega \int_0^{l_{max}} \rho^2_\odot Q^0_X \delta^{(3)}\left[\vec{r}(l)\right] dl(\psi) = \frac{Q^0_X}{\Delta\Omega}\left(\frac{\rho^2_\odot}{D^2_\odot}\right) . \tag{6.19}$$

The same astrophysical factor for the gamma-ray observation coming from the GC direction with a telescope with the same HESS solid angle $\Delta\Omega \simeq 10^{-5}$ sr and NFW DM density distribution is $\langle J\rangle^{NFW}_{\Delta\Omega^{\rm HESS}} = 280\times 10^{23}$GeV^{2}cm^{-5}. Thus, the equivalent normalization constant, that we will use as reference, is given by

$$Q^{0-\rm NFW}_X \;=\; \langle J\rangle^{NFW}_{\Delta\Omega}\Delta\Omega_{\rm HESS}\left(\frac{D_\odot}{\rho_\odot}\right)^2 \simeq 2.13\cdot 10^{60}\,{\rm m}^3\,{\rm sr}. \tag{6.20}$$

It is interesting to compare the antiproton flux coming from the GC and the expected contribution from the continuous halo. The relation will depend on the diffusion model and the particular features of the DM density distribution. In order to give numerical

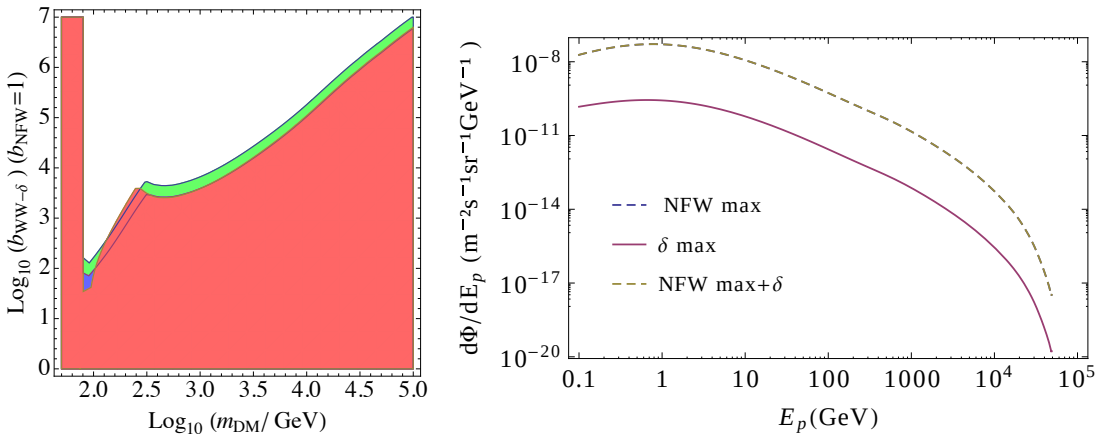

FIGURE 6.5: *(Left–panel)* Combination of both contributions from the NFW halo and point-like DM distribution in Fig. 6.4 (i.e., the boost factor associated with the NFW halo emission is taken to be one: $b^{WW}_{\rm NFW} = 1$, and the boost factor associated with the point-like source $b^{WW}_{\delta-\rm NFW}$, is again plotted in the vertical axis). *(Right–panel)* Antiproton differential flux at the TOA after propagation for 48.8 TeV DM annihilating into W^+W^- pairs by assuming the maximum propagation model. Dashed lines correspond to the contribution from a spatial distribution following the standard NFW halo profile, whereas the full line stands for the contribution from a point-like source located at the GC with amplitude $Q_X^{0-\rm NFW} = 2.13 \cdot 10^{60}\,{\rm m}^3\,{\rm sr}$. This second contribution is subdominant and the addition of both components overlap with the one coming from the continuous halo.

results, we will focus again in the annihilating DM case within the standard NFW profile. The diffusion Equation (6.3) applies to the total antiproton source coming from DM annihilation. The steady solution is also given by Eq. (6.4), but we need to take into account the continuous distribution of the DM to compute $R^{\rm NFW}(E_{\bar{p}})$ from Eq. (6.5):

$$Q_X(\vec{r}) = \left[\frac{\rho_{\rm NFW}(\vec{r})}{\rho_\odot}\right]^2 . \tag{6.21}$$

As we see in Fig. 6.2, when $Q_X^0 \simeq 1$ in units of $Q_X^{0-\rm NFW}$, the propagation function $R^\delta(E_{\bar{p}})$ for the point-like DM source at the GC is comparable with the propagation function $R^{\rm NFW}(E_{\bar{p}})$ for the NFW halo profile. Moreover, fitting HESS data requires typically $Q_X^0 \simeq 10^3\, Q_X^{0-\rm NFW}$, which implies that the GC contribution could dominate the standard one (see Fig. 6.2).

The emission spectra of the source term for annihilating DM is

$$Q_E(E_{\bar{p}}) = \frac{1}{2}\left(\frac{\rho_\odot}{m_{\rm DM}}\right)^2 \sum_i \langle\sigma v\rangle_i \frac{dN_i^{(\bar{p})}}{dE_{\bar{p}}} . \tag{6.22}$$

The differential number of antiprotons per energy unit $dN_i^{(\bar{p})}/{\rm d}E_{\bar{p}}$, produced in a given annihilating or decaying channel i, involves hadronization and possible decays of unstable products. This requires Monte Carlo events generators [139] or fitting or interpolation functions [38]. In particular, we will use the results reported in [50]. They refer to `PYTHIA` 8.135 Monte Carlo events generator software [76] and reproduce the differential

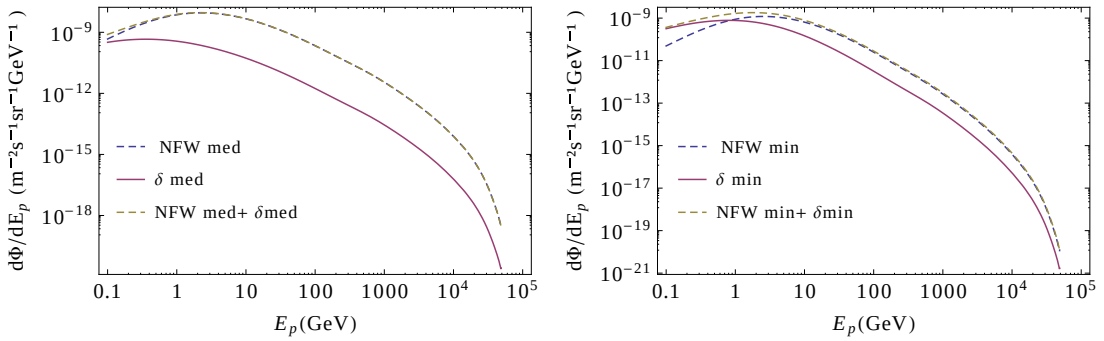

FIGURE 6.6: *(Left–panel)* The same as the right-panel of Fig. 6.5 for the medium propagation model. *(Right–panel)* The same as the right-panel of Fig. 6.5 for the minimum propagation model. In this case, the contribution from the GC is dominant at low energies.

number of antiprotons produced by DM of different masses. In order to be conservative with the previous analysis of this thesis, we will focus on antiproton fluxes coming from fragmentation and decays of SM particle-antiparticle pairs produced by DM annihilation. We will ignore DM decays. In particular, we will illustrate our analysis by considering DM annihilation into W^+W^- pairs that are consistent with the origin of the HESS J1745-290 gamma-ray observations [69] discussed in the previous chapters, as an interesting example.

Thus, in the left panel of Fig. 6.3, we show the antiproton flux generated by a 48.8 TeV DM particles that annihilate into W^+W^- pairs at source, before the propagation. As we can see, electroweak (EW) corrections are important for antiproton production at low energies. In the right panel of Fig. 6.3, we show the antiproton flux at TOA after the propagation within the Galaxy when the *primary* source is the mentioned 48.8 TeV DM annihilating into the W^+W^- channel in the cases of a NFW halo profile and a point-like source at the GC for different diffusion models.

We can compare with the PAMELA antiproton data in order to constrain a vast range of DM masses depending on the particular value of Q_X^0, the DM mass $m_{\rm DM}$, and the annihilation or decay channel. In particular, we will present results for the NFW halo profile and annihilating DM into the W^+W^- channel by assuming the standard thermal averaged cross-section $\langle\sigma v\rangle = 3\times10^{-26}{\rm cm}^3{\rm s}^{-1}$. In the left panel Fig. 6.4, we analyze the case of the only contribution of a simple NFW halo profile.

For DM masses below $m_W \simeq 80.4$ GeV, DM cannot annihilate into a real W^+W^- pair. However, for a kinematically allowed annihilation channel, it is well known that low mass DM particles are severely constrained for masses below 1 or 100 GeV, depending on the diffusion model features (minimum or maximum type, respectively). The restrictions can be extrapolated to higher masses for high values of the boost factor $b_{\rm NFW}$, which accounts for possible enhancements of the antiproton flux due to higher annihilating

cross sections or different DM density distributions. Indeed, enhancements of order $b_{\rm NFW} \simeq 10^3$ allow to restrict DM masses of order $m_{\rm DM} \simeq 100$ GeV or even $m_{\rm DM} \simeq 10$ TeV depending on the particular features of the antiproton propagation. It is also interesting to compare the sensitivity of the antiproton and gamma-ray analyses. For DM particles with masses below 500 GeV, the gamma-ray study should be done with the observations of the Fermi Gamma-ray Space Telescope. For example, we can compare our results with the gamma-ray analysis performed in [140], although this comparison depends on the particular dark halo shape and substructure. For a NFW halo, the thermal DM cross-section mentioned above is typically excluded for a DM mass below 20 GeV. In the case of the W^+W^- channel, this constraint does not apply since it is below the production threshold. However, this DM model would be excluded for a small boost factor of $b^{WW}_{\rm NFW} = 3$ at 100 GeV or $b^{WW}_{\rm NFW} = 10$ at 1 TeV. By comparing with the left panel of Fig. 6.4, we conclude that the gamma-ray analysis is more sensitive except for the maximum propagation model. Under this assumption, both studies are competitive and a combined analysis could improve DM constraints.

In the right panel in Fig. 6.4, we show the results from the same analysis computed for the propagation of antiprotons produced at a point-like source centered at the GC. Following our convention, we need very high values of Q^0_X in units of $Q_X^{0-\rm NFW}$ in order to find significant constraints. We can define the boost factor associated to the central contribution as $b_{\delta-\rm NFW} = Q^0_X/Q_X^{0-\rm NFW}$. In contrast with $b_{\rm NFW}$, it is important to remark that, in general, there is not a preferred theoretical value for $b_{\delta-\rm NFW}$. It depends on the particular clustering mechanism for the DM substructure localized at the GC. Indeed, it may be much larger or smaller than one.

In such a case, we can compute the total antiproton flux as:

$$\frac{d\Phi^{\rm DM}_{\bar p}}{dE_{\bar p}} = \frac{v_{\bar p}}{8\pi}\left(\frac{\rho_\odot}{m_{\rm DM}}\right)^2 \sum_i \langle\sigma v\rangle_i \frac{dN_i^{(\bar p)}}{dE_{\bar p}} \left[b^i_{\rm NFW}\cdot R^{\rm NFW}_{\bar p}(E_{\bar p}) + b^i_{\delta-\rm NFW}\cdot R^{\delta-\rm NFW}_{\bar p}(E_{\bar p})\right], \tag{6.23}$$

where i labeled the possible different annihilating or decaying channel contribution, and $R^{\delta-\rm NFW}(E_{\bar p})$ means the propagation function associated to the localized central contribution normalized with $Q^0_X = Q_X^{0-\rm NFW} \simeq 2.13\cdot 10^{60}\,{\rm m}^3\,{\rm sr}$. Because antiprotons from the GC could reach the Earth from any direction, they would be hard to distinguish from the ones produced by the continuous halo distribution.

By taking into account both contributions, and particularizing again for the W^+W^- annihilation channel, we can reach the results shown in the left-panel of Fig. 6.5 for $b^{WW}_{\rm NFW} = 1$. DM particles with masses below approximately 100 GeV, which annihilate in the mentioned boson channel are excluded for the maximum diffusion model (right

panel Fig. 6.5). This is due to the GC contribution and because the majority of the antiproton flux produced by heavy DM annihilating into W^+W^- pairs contributes mainly at high energies. The point-like contribution dominates for $b^{WW}_{\delta-\mathrm{NFW}} \gtrsim 10^3$, whereas it is negligible for $b^{WW}_{\delta} \lesssim 10^{-2}$. In any case, heavy DM masses are allowed also with large values of $b^{WW}_{\delta-\mathrm{NFW}}$. In fact, current observations are not sensitive to the DM particle masses around 48.8 TeV. Such a value is consistent with the origin of the HESS data of gamma rays coming from the GC, which requires $b^{WW}_{\delta-\mathrm{NFW}} = 1767 \pm 419$ [69] (We define $b^{WW}_{\mathrm{HESS}} \equiv 1767$ as a benchmark boost factor, which we will use to illustrate our results). Similar features can be observed in Fig. 6.5 . The contribution from the point-like source at the GC is more important at low energies. This result is general for any value of the DM mass. On the contrary, the mass value characterizes the emission at high energies, since the spectra show a cut-off at the DM mass. These high energy features are quite independent of the spatial distribution assumed for the DM particles. Similar conclusions can be derived from Fig. 6.7, where an explicit comparison with the PAMELA data is provided.

One of the most interesting conclusions of this Chapter is the relation between the results associated with different analyses. In particular, by comparing the two panels of Fig. 6.4, we can observe the antiproton sensitivity dependence on the diffusion model. The most important restrictions for the dark halo emission come from the maximum diffusion model, whereas the minimum model is the least constraining. On the contrary, for the antiprotons produced at the GC, the constraints are more important for the minimum diffusion model for DM masses lower than 200 GeV. For masses higher than 1 TeV, the most constraining models are the minimum and the maximum one.

Therefore, the most constraining diffusive model on antiproton fluxes depends on whether they are produced from the GC (right panel of Figure 6.4) or from the entire halo (Figure 6.4 left panel). These results can be understood by observing Fig. 6.2 and Fig. 6.7. The most important constraints for the GC emission are provided by the minimum diffusion model if the restrictions are dominated by low energy observations (antiproton data around 1 GeV). If the restrictions come from the high energy data (around 100 GeV), minimum and maximum propagations give the most restricting results. On the contrary, independently on the DM mass, the maximum diffusion model is the most constraining if the antiprotons are produced within the entire dark halo.

6.5 Conclusions

Present antiproton flux measurements are compatible with standard diffusion models of cosmic-rays without additional primary sources. Indeed cosmic-ray interactions with the

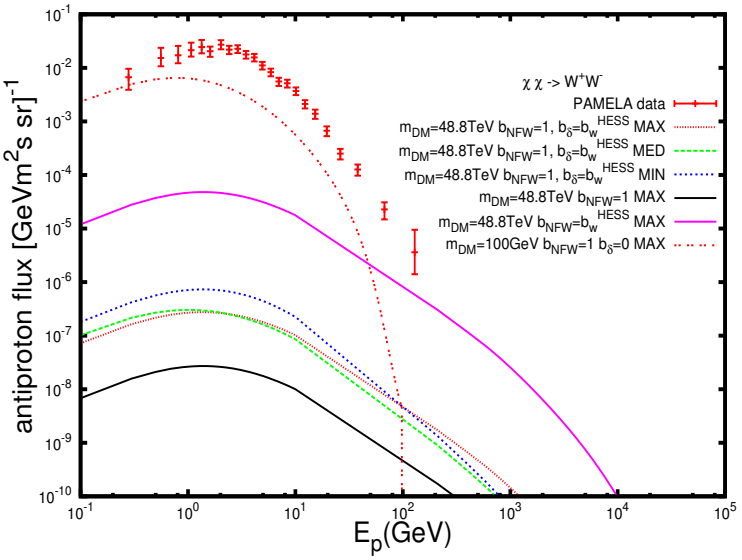

FIGURE 6.7: Antiproton differential flux at the TOA after propagation for 48.8 TeV DM annihilating into W^+W^- pairs for different diffusion models and distribution profiles: The lower signal (black line) corresponds to the non-boosted NFW profile by employing the maximum diffusion model. On the other hand, the same assumptions give raise to the highest flux at high energies (violet line) but with a boost factor of $b^{WW}_{\rm NFW} = b^{WW}_{\rm HESS} = 1767$. A point-like source is negligible for this diffusion model if it is not enhanced by very large factors (see right-panel of Fig. 6.3 or right-panel of 6.5). We show the antiproton flux at TOA for the medium diffusion model for non-boosted NFW profile plus enhanced δ-DM distribution ($b^{WW}_{\delta-{\rm NFW}} = b^{\rm HESS}_{WW}$) at the GC for three diffusion models (blue big-dotted, green rushed and red little-dotted line). Finally, we show as a non-boosted NFW profile of 100 GeV DM annihilating into the W^+W^- channel is excluded also without enhancement at the GC.

ISM and their propagation represents the background for new astrophysical primaries that may produce an important amount of antiprotons. We have analyzed the prospective signatures that should be produced by different types of antiproton spectra sources at the center of our Galaxy. The diffusion of antiproton particles highly affects the final signature. In this sense, our analysis can be used to constrain new sources of primary antiprotons if the agreement between observations and predictions is maintained; or alternatively, it can determine the features of the diffusion model if a new antiproton flux component from the GC is identified. We have studied the antiproton propagation function for a point-like source at the GC. In general, this function depends on the spatial distribution source. We have analyzed the flux at the TOA for three emission spectra, considered as different models that could be associated to a large variety of astrophysical sources, such as the case of a power law flux, monochromatic emission, or to annihilating or decaying DM. We have compared such flux with the present antiproton data. In order to be conservative, we have neglected the background contribution. We have studied the sensitivity by constraining the different features of the mentioned spectra, as the total normalization amplitude, the power index, the characteristic energy, the DM mass, etc. The constraints are very general and need to be compared with particular motivated

sources. Alternatively, if an excess is observed, our analysis can determine the particular model favoured for such data.

In the case of the DM, there are two reasons for the analysis. On the one hand, DM can be compacted around a very localized region at the center of our galaxy for different processes, as the baryonic compression or black hole effects. On the other hand, numerical computations of the diffusion equation present a singularity at the GC, because of the central behaviour of DM halos density profiles. This divergence needs to be regularized. The simplest possibility is removing it below a given radius [50]. Another possibility is to consider its contribution separately as a point-like source. In any case, the contribution from the local continuous halo profile is expected to be important and the interplay between both contributions gives a rich phenomenology, as we have shown in the present chapter.

Chapter 7

Monte Carlo Event Generator Uncertainties

As shown in this thesis so far, in order to set constraints on the diverse DM models and get a better understanding of the astrophysical factor associated with the distribution of this kind of matter, numerous signals detected in gamma–rays, neutrinos, positrons, antiprotons and other particles have been studied in the available literature [55–60, 89, 91, 141]. The majority of these analyses make use of Monte Carlo event generator packages, that allow to predict the spectra of final-state particles generated by DM annihilation and decays into SM particles. The most used Monte Carlo generator packages are `PYTHIA` and `HERWIG`, both with available versions written either in Fortran or C++.

In this Chapter we shall focus on the gamma–ray spectra generated by these four codes, showing how the choice of the Monte Carlo code may affect the DM search. Thus, Section 7.1 is devoted to illustrate the main differences between `PYTHIA` 6.418 (Fortran version), `PYTHIA` 8.165 (C++ version), `HERWIG` Fortran version 6.5.10 and `HERWIG` C++ version 2.6.1. In Section 7.2 we determine the differences between the four Monte Carlo codes when four illustrative annihilation channels are studied. In Section 7.3 we then analyze the implications that these differences may have in the WIMPs phenomenology and DM indirect searches. Finally Section 7.4 shall cover the main conclusions of such analysis. This Chapter is based on [142].

7.1 Monte Carlo simulations

As introduced, the majority of the analyses for indirect search of DM make use of Monte Carlo event generator packages, of which the most used are `PYTHIA` and `HERWIG`,

both available in Fortran and C++. Among others cosmic-ray fluxes, the differential photon flux produced by Monte Carlo event generators may be understood as the outcome obtained from a particle shower schematization in three fundamentals parts: the QCD Final-State Radiation, the hadronization model and the QED Final-State Radiation. Differences between available generators in the aforementioned parts, may help understanding the origin of such differences. Therefore, let us study separately the technicalities of each part in the following (read [141] for further details).

7.1.1 QCD Final-State Radiation

The QCD Final-State Radiation is described by the elementary probability to radiate either quarks or gluons (partons). This probability is universal in the soft (low energy) and collinear (high energy) approximation. In these two limits the branching probability is proportional to [143]:

$$\frac{\alpha_s(k_T)}{2\pi}\Delta_s(Q^2_{max},Q^2)P^{\rm MC}_{i,jk}(z_{\rm MC})\frac{{\rm d}Q^2}{Q^2}{\rm d}z_{\rm MC}\frac{{\rm d}\phi_{\rm MC}}{2\pi}\ , \tag{7.1}$$

where α_s is the coupling constant of the strong interaction, Q^2 is the evolution variable, Q^2_{max} is its maximum allowed value, $z_{\rm MC}$ and (1- $z_{\rm MC}$) are the energy fraction of the two generated partons, and $\phi_{\rm MC}$ is the azimuthal angle ($z_{\rm MC}$ and $\phi_{\rm MC}$ are defined in the center of mass frame, but other definitions only differ beyond the leading logarithmic order approximation). $P^{\rm MC}_{i,jk}(z_{\rm MC})$ is the Altarelli-Parisi [144] splitting function describing the distribution of the fraction $z_{\rm MC}$ of the emitted parton energy with respect to its parents, where the subindices i and jk stand for the incoming and final parton species. $\Delta_s(Q^2_1,Q^2_2)$ holds for the Sudakov form factor accounting for all the non-resolvable effects of the perturbative theory (quantum loops and resonances among others) acting on the probability of transition between Q_1 and Q_2 states. Q^2_{max} is set by the hard-scattering, i.e., the head (initial) process of the parton shower, and Q^2_0 is the last process when the parton shower ends and the hadronization begins.

The evolution variable Q^2 represents the first difference between the Monte Carlo simulations: In `HERWIG` and `HERWIG++` $Q^2 \simeq E^2(1-\cos\theta_{\rm MC})$, where E is the energy of the parent parton and $\theta_{\rm MC}$ is the emission angle. It was originally implemented in [145]. However, in `PYTHIA` 6.4 the evolution variable Q^2 corresponds to the virtuality of the emitted parton, i.e., its virtual mass, whereas in `PYTHIA` 8 is given by k_T, the transverse momentum of the emitted parton with respect to the emitting one. The latter formulation allows to order the final-state showers with regard to k_T through a sequence of falling transverse-momentum values [146]. In most cases, the two variables used in

the two versions of PYTHIA are compatible, but HERWIG turns out to reproduce more accurately the color coherence dependent data in the soft limit.

Finally, the Sudakov form factor for one parton is given by [35]:

$$\Delta_S(Q^2_{max}, Q^2) = \exp\left[-\int_{Q^2}^{Q^2_{max}} \frac{\mathrm{d}k_T^2}{k_T^2} \int_{z_{min}}^{z_{max}} \mathrm{d}z_{\mathrm{MC}} \frac{\alpha_s(z_{\mathrm{MC}}, k_T^2)}{2\pi} P^{\mathrm{MC}}_{i,jk}(z_{\mathrm{MC}})\right] . \quad (7.2)$$

In multiparton processes, the previous equation needs to be integrated; the integration method differs for each package. For instance, in PYTHIA $z^{min}_{\mathrm{MC}} = Q_0^2/Q^2$, whereas in HERWIG $z^{min}_{\mathrm{MC}} = Q_0/Q$. With regard to z^{max}_{MC}, it satisfies $z^{max}_{\mathrm{MC}} = 1 - z^{min}_{\mathrm{MC}}$ for all the codes. This definition leads to conclude that, for a given value for Q^2, the evolution range in the z_{MC} variable is larger in PYTHIA than in HERWIG. When comparing the two simulations with LEP data, the strong coupling constant α_s takes also different values, being $\alpha_s(M_Z) \simeq 0.127$ in PYTHIA and $\alpha_s(M_Z) \simeq 0.116$ in HERWIG. This fact depends on the implemented approximation. In the QCD shower, the soft gluons interference effects lead to an ordering of subsequent emissions in terms of decreasing angles. This approximation of coherence effects also depends on the Q^2 definition. For the first mass-ordering version of PYTHIA, in which $Q^2 \approx m^2$ with $m^2 = E^2 - k^2 \geq 0$, it had to be implemented as additional requirement. In the case of the k_T-ordering version, with $Q^2 \approx k_T^2 = z_{\mathrm{MC}}(1 - z_{\mathrm{MC}})m^2$, it leads directly to the proper behavior. Finally, due to theoretical analysis, the scale choice $\alpha_s = \alpha_s(k_T^2) = \alpha_s(z_{\mathrm{MC}}(1 - z_{\mathrm{MC}})m^2)$ is the default one in PYTHIA. On the other hand, HERWIG takes into account this effect via the angular ordering of emissions in the parton shower by redefining the running constant. In this case, $\alpha_s = \alpha_s\left(z^2_{\mathrm{MC}}(1 - z^2_{\mathrm{MC}})\tilde{q}^2\right)$, where $\tilde{q}$ corresponds to the scale of the decaying parton. Moreover, a two-loop approximation is reproduced in HERWIG by means of the Monte Carlo scheme with $\alpha_s^{\mathrm{MC}} = \alpha_s^{\bar{\mathrm{MS}}}(1 + K\alpha_s^{\bar{\mathrm{MS}}}/2\pi)$, where $\alpha_s^{\bar{\mathrm{MS}}}$ is defined in the usual modified minimal subtraction ($\bar{\mathrm{MS}}$) scheme in QCD (read [147] for further details). In any case, we conclude that photon emission is not affected by angular ordering [148].

7.1.2 Hadronization

When the evolution variable Q^2 reaches the value Q_0^2, the parton shower ends and the hadronization begins. Two different models to describe hadronization are thus developed in the two aforementioned packages. PYTHIA relies on the String Model Hadronization [148, 149] whereas HERWIG does on the Cluster Model Hadronization [150, 151]. In any case, both models take into account the experimental data collected by the LEP for tuning their parameters. In particular, the standard "tunes" use data at 100 GeV of center of energy. In the future, new tunes could also consider the LHC data. In any

case, the hadronization model does not seem to affect the gamma–ray spectra in an appreciable way, except if the π^0 production changes significantly. Finally, let us remaind that most of the hadrons formed during the hadronization process are unstable and will eventually decay. The resultant final states, which are mainly leptons, lead the photon production involving QED processes.

7.1.3 QED Final-State Radiation

The radiation emitted by quarks, $W^{\pm}$ bosons, and charged leptons (i.e. Bremsstrahlung radiation), as well as the possibility of pair production, can be added to equation (7.1) introduced above. The Bremsstrahlung component of the Final-State Radiation (FSR) represents the main contribution in the case of gamma–rays produced by DM annihilating/decaying into e^+e^- and $\mu^+\mu^-$ channels. The high energy leptons come directly from the hard process in the first case and both from hard processes and $\mu^{\pm}$ decay in the second one. In any case, associated γ-photons are produced by Bremsstrahlung effects in both cases. Bremsstrahlung FSR from hard processes is currently not implemented in `HERWIG++` version 2.6.1, being unable to produce gamma–ray spectra in the case of e^+e^- and $\mu^+\mu^-$ channels, while it is included in both `HERWIG` and `PYTHIA` (6.4 and 8). This component clearly affects all the logarithmic part of gamma–ray spectra at high energy generated with `HERWIG++`, as shall be shown in the following sections.

With regards to the electroweak (EW) $2 \to 2$ processes of the FSR, where photons are produced or annihilated, `PYTHIA` 8 accounts for all these processes, except the $\gamma\gamma \to W^+W^-$. As for `HERWIG`, it contains the $q \to q\gamma$ processes, but not the process $\gamma \to f\bar{f}$. These two last processes are indeed contained in `HERWIG++`. However, we verified that different sets of such processes did not affect the gamma–ray spectra in an appreciable way after modifying the codes.

7.2 Gamma–ray spectra from DM annihilation/decay

In this Section we study the spectra of four relevant channels by using the four Monte Carlo generators mentioned above. Namely, we have studied the on-shell channels: W^+W^-, $b\bar{b}$, $\tau^+\tau^-$ and $t\bar{t}$ since they are representative channels of the phenomenology of annihiliating/decaying DM. The $t\bar{t}$ channel was studied separately since it presents a particular phenomenology with respect to the other quark channels.

The photon spectra is better described in terms of the dimensionless variable:

$$x \equiv 2\frac{E_\gamma}{E_{\rm CM}}\,, \tag{7.3}$$

where E_γ and $E_{\rm CM}$ correspond to the photon and center of mass (CM) energies, respectively. This variable is simply reduced to $x \equiv E_\gamma/m_{\rm DM}$ in the case of annihilating DM and therefore lies in the range between 0 and 1. Large differences between spectra are usually present at extremes of x. For this reason, we present the spectra in both linear and logarithmic scales for x. In the first (second) case the behavior at high (low) x is more clearly shown. For each channel, we focused on two values of DM particle mass: 100 GeV and 1 TeV. In the case of the $t\bar{t}$ channel the masses under study were 500 GeV and 1 TeV.

Gamma–ray spectra from DM annihilation: W^+W^- channel

The simulated gamma–ray spectra for DM particles annihilating into W^+W^- channel appear very similar for $x > 10^{-5}$ both for a DM mass of 100 GeV and 1 TeV. This behavior can be seen in Figs. 7.1 and 7.2 respectively. It is clear from the figure the considerably lower fluxes generated by `HERWIG++` at high energies as compared to the rest of packages, probably because of the absence of Bremsstrahlung from hard processes in the e^+e^- and $\mu^+\mu^-$ cases commented before. On the other hand, a slight difference is observed for energies between $x = 0.3 - 0.7$ with `HERWIG` providing in both cases the highest values. Nonetheless, the main differences appear at lower energies as can be seen in Figs. 7.1 and 7.2. In `PYTHIA` 8, we have generated each photon spectrum by using the resonant process $e^+e^- \to \phi^*$, where ϕ^* is a resonance with mass of $E_{\rm CM}$ and a user-defined decay mode. This procedure is very similar to the one we used for `PYTHIA` 6.4, except that channels were created by using the subroutine `PY2ENT`. In `HERWIG++`, we used the scattering of photons as the initial process. The photon spectra are then independent of the initial beams (e^+e^- or $\gamma\gamma$) and solely depend on the energy of the event, i.e. $E_{\rm CM} = 2m_{\rm DM}$. In `PYTHIA` 8, the cut-off at low energy strongly depends upon this parameter `pTminChgL` (dubbed here p_T) and exactly corresponds to its set value, with allowed range of 0.001 – 2.0 and a default value of 0.005. (FIG. 7.3 *(Right-panel)*) In `HERWIG++`, `QEDRadiationHandler` is set off by default, so that the cut-off appears to higher energy with respect to the other Monte Carlo generators. In the opposite case, when `QEDRadiationHandler` is enable and the relevant parameter `IFDipole:MinimumEnergyRest` varies in values, the spectrum at low energy changes drastically. Smaller values of such parameter enlarge the production of photons at low energies (See Fig. 7.3, *left–panel*).

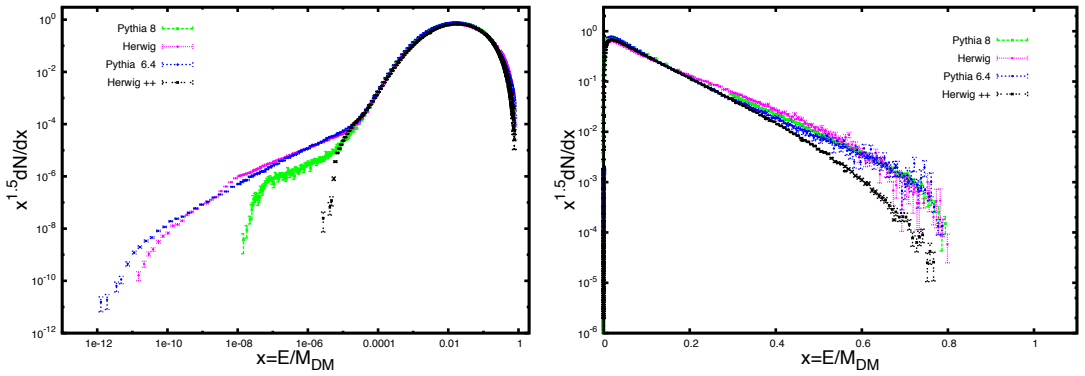

FIGURE 7.1: *(Left–panel)* DM particles annihilating into W^+W^- channel with $m_{\rm DM} = 100$ GeV in logarithmic scale. The simulations are consistent down to $x \simeq 10^{-4}$. At $x \simeq 10^{-5}$ Fortran simulations are bigger than the C++ ones by a factor ten. At $x \simeq 10^{-6}$ no more photons are produced in `HERWIG++` provided that the `QEDRadiationHandler` is set off as default. In our simulation, `QEDRadiationHandler` is switched on with a clear cut-off at energy of 10^{-10}. Analogous cut-off appear at $x \simeq 10^{-8}$ in `PYTHIA` 8, $x \simeq 10^{-11}$ in `HERWIG` and $x \simeq 10^{-12}$ in `PYTHIA` 6.4 . The simulations are very different at these energy values and physical validity has to be checked. Due to the fit of the Monte Carlo codes with high energy colliders (such as LEP and LHC) that are poor of data at low energy, simulations at low energies might be unreliable. If this is the case, it is expected that this effect affects all the simulated channels. *(Right–panel)* DM particles annihilating into W^+W^- channel with $m_{\rm DM} = 100$ GeV in linear scale. Notice the lower flux for `HERWIG++` at high energies when compared to the rest of packages

Gamma–ray spectra from DM annihilation: $b\bar{b}$ channel

In the case of DM annihilation into $b\bar{b}$ channel, the `HERWIG++` spectrum appears lower for high energy ($x > 0.6$) with respect to the other simulations, due to the lack of the Bremsstrahlung photons generated by high energy leptons. Thus, both `PYTHIA` codes and `HERWIG` simulations look very similar qualitatively for the two studied values of DM mass as seen in Figs. 7.4 and 7.5. On the other hand, at very small energies $\left(x < 10^{-4}\right)$ `HERWIG` simulation returns higher values of the flux with respect to the other packages. This fact can be seen in Figs. 7.4 and 7.5. The other codes for these small energies agree very well in their predictions.

Gamma–ray spectra from DM annihilation: $\tau^+\tau^-$ channel

Differences in the gamma-spectra appear in the case of DM particles annihilating into leptonic channels. Here we show the $\tau^+\tau^-$ annihilation channel as an illustrative example. In this channel and for the two studied DM masses, both `HERWIG` codes present an important suppression of the spectrum for energies in the interval $0.8 < x < 1$, while both versions of `PYTHIA` extend the photon spectra up to $x = 1$ with higher spectra. This fact can be observed in Figs. 7.6 and 7.7 and may be explained by the absence of Bremsstrahlung gamma–rays generated by high energy leptons when `HERWIG` codes

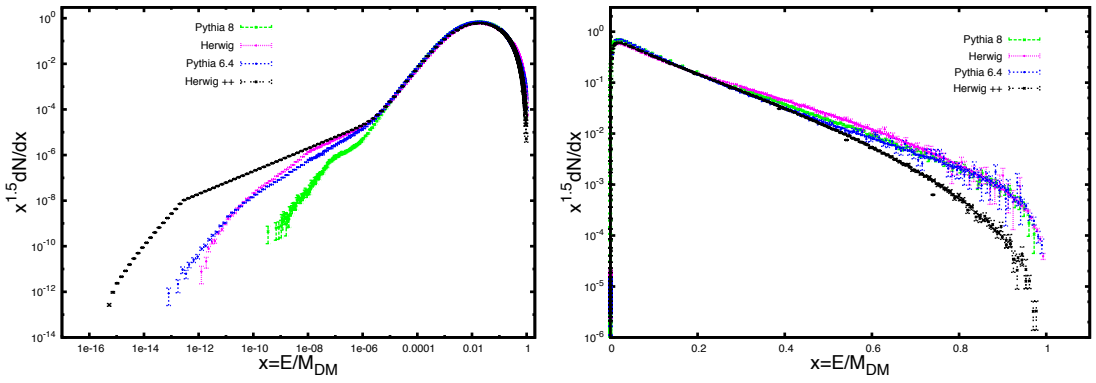

FIGURE 7.2: *(Left–panel)* W^+W^- annihilation channel with $m_{\rm DM} = 1$ TeV in logarithmic scale. As in Fig. 7.1, the simulations are consistent down to a value of x, that is 10^{-6} in the case of $m_{\rm DM} = 1$ TeV (a factor ten lower in x with respect to the case with $m_{\rm DM} = 100$ GeV). Similar behaviors of the lower energy cuts-off are also observed, with a general shift of x cut-off value of order 10^{-2}. *(Right–panel)* W^+W^- annihilation channel with $m_{\rm DM} = 1$ TeV in linear scale. All the simulations except for `HERWIG++` exhibit the same behavior as in Fig. 7.1, but within $x \simeq 0.3$ and $x \simeq 0.7$ and a maximum discrepancy at $x \simeq 0.5$. The shift with respect to Fig. 7.1 can be simply explained by the increment of the WIMP mass.

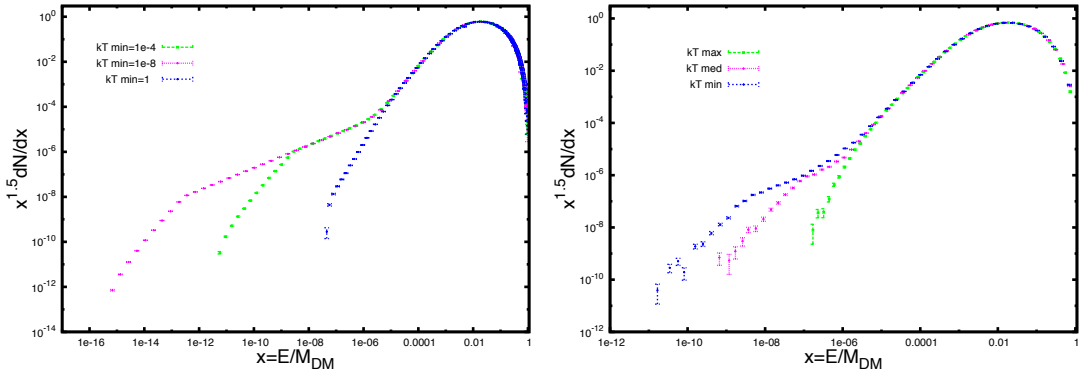

FIGURE 7.3: Cut-off at low energy photons in C++ codes. High energy linear scale are not affected. *(Left–panel)* W^+W^- annihilation channel with HERWIG++ at $m_{\rm DM} = 1$ TeV in logarithmic scale. Different cut-off at low energy in logarithmic scale correspond to cuts in the `QEDRadiationHandler` of $k_T = 10^{-8}, 10^{-4}, 1$. *(Right–panel)* $b\bar{b}$ annihilation channel with PYTHIA 8 at $m_{\rm DM} = 1$ TeV in logarithmic scale. Here the cut-off are set as the minimum, medium and maximum value of the allowed range of value.

are used. As can be seen in the leptonic and muonic channel, `HERWIG` Fortran accounts for an extrapolation with respect to the Bremsstrahlung photons related with hard processes, but it does not provide an exact implementation of this EW process. This is the reason why the gamma–ray spectra simulated with `HERWIG` Fortran for channels where the Bremsstrahlung radiation contribution is subdominant are in agreement with `PYTHIA` 6.4 and 8 results, up to the statistical errors. Moreover, a difference of one order of magnitude appears for energies $x \geq 0.8$ among `PYTHIA` codes and `HERWIG` codes. At intermediate energies, $x \approx 10^{-3} - 0.2$, all codes agree. For small energies, `PYTHIA` packages agree in their spectra up to $x = 10^{-7}$ but not for lower energies where both

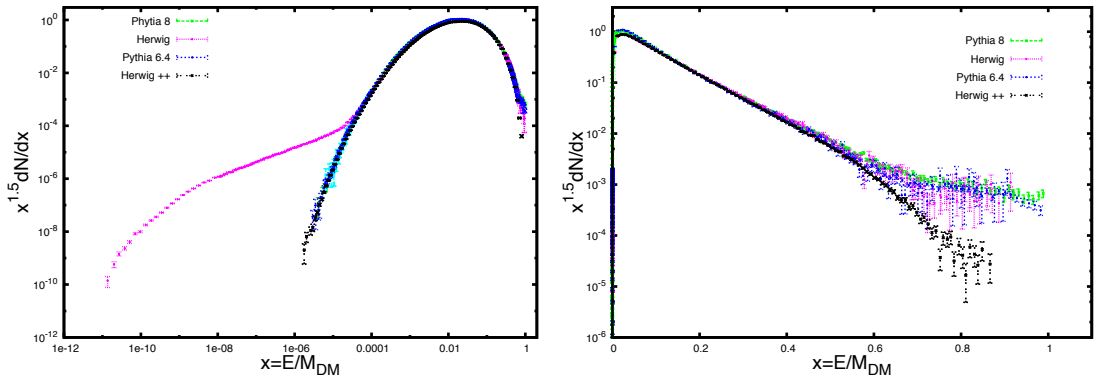

FIGURE 7.4: *(Left–panel)* $b\bar{b}$ annihilation channel with $m_{\rm DM} = 100$ GeV in logarithmic scale. Three of the four simulations perfectly match down to $x \simeq 10^{-6}$, where no more photons are produced. `HERWIG` Fortran also match down to $\simeq 10^{-5}$. Here, its simulated flux appears much bigger, with no photons counted at energies smaller than $x \simeq 10^{-11}$. *(Right–panel)* $b\bar{b}$ annihilation channel with $m_{\rm DM} = 100$ GeV in linear scale. Three of the four simulations are in agreement within the statistical error bars on the full x range, while `HERWIG++` gives lower flux above $x \simeq 0.5$.

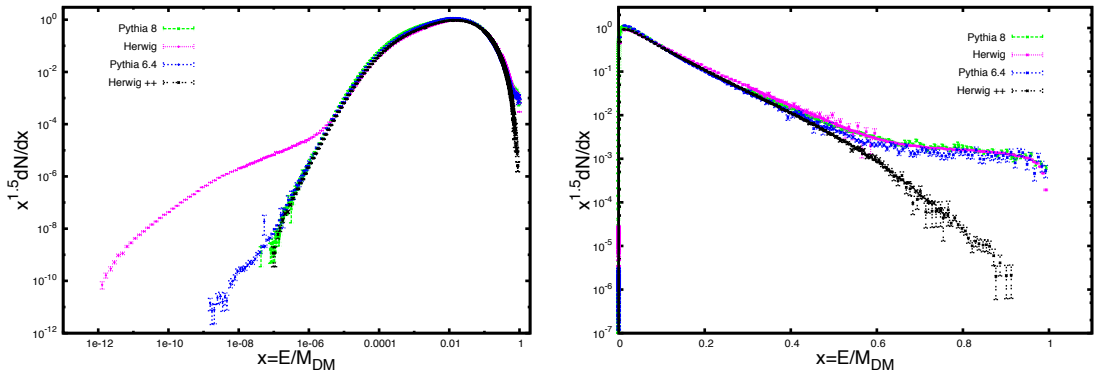

FIGURE 7.5: *(Left–panel)* $b\bar{b}$ annihilation channel with $m_{\rm DM} = 1$ TeV in logarithmic scale. `PYTHIA` 6.4 agrees with both `HERWIG++` and `PYTHIA` 8 down to $x \simeq 10^{-7}$, where the spectra of the latter two packages stop. `PYTHIA` 6.4 stops providing gamma–rays at $x \simeq 10^{-9}$. Once again, `HERWIG` generates larger gamma–ray fluxes at low energy. The difference at high energy discussed in Fig. 7.2 is also apparent on the right panel. *(Right–panel)* $b\bar{b}$ annihilation channel with $m_{\rm DM} = 1$ TeV in linear scale. As in Fig. 7.4, `HERWIG++` gives much lower flux above $x \simeq 0.5$. Although `HERWIG` agrees both with Pithia 6.4 and `PYTHIA` 8 within statistical errors, `PYTHIA` 8 flux (with better statistics) appears two or three times bigger than `PYTHIA` 6.4 at $x \simeq 0.6, 0.8$.

`PYTHIA` 8 seems to be strongly suppressed for energies smaller than $x = 10^{-7}$.

`HERWIG++` produces less photons for small energies $x \leq 10^{-3}$, although the `QEDRadiation Handler` was enable. Concerning `HERWIG`, the spectrum can be extended down to $x = 10^{-11}$ and it lies in between the `PYTHIA` 6.4 and `HERWIG++` simulations, for the two studied masses and for small energies. With regard to high energies close to $x = 1$, `HERWIG` spectrum is the most suppressed for this channel.

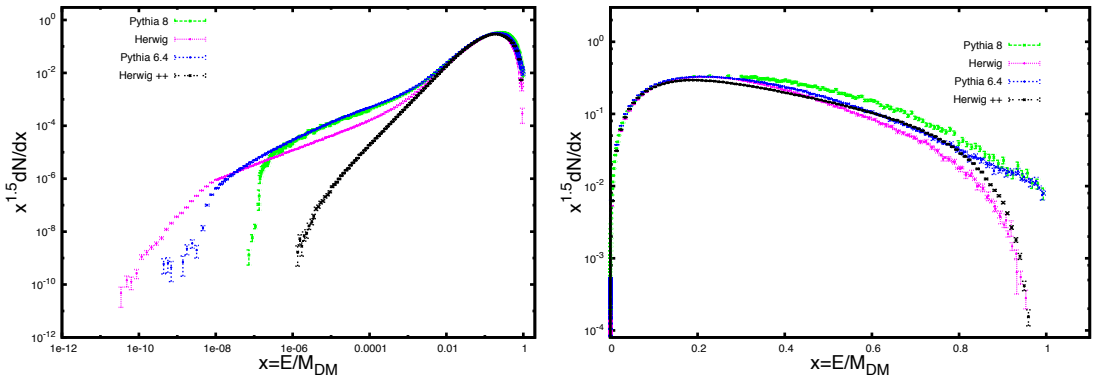

FIGURE 7.6: *(Left–panel)* $\tau^+\tau^-$ annihilation channel with $m_{\rm DM} = 100$ GeV in logarithmic scale. The simulations are inconsistent below $x \simeq 10^{-2}$. PYTHIA codes are more consistent, generating the same spectral form down to $x \simeq 10^{-7}$, where PYTHIA 8 has its cut-off. PYTHIA 6.4 spectra attains smaller energies to almost 10^{-10}. HERWIG cut-off reaches almost $x \simeq 10^{-11}$, but its flux is lower than the PYTHIA ones below $x = 10^{-3}$ and reaching the maximum inconsistence of almost a factor ten at $x = 10^{-5}$. HERWIG++ appears totally inconsistent with the other three packages, with a much lower flux that gets a maximum divergence of 5 orders of magnitude at $x \simeq 10^{-6}$ where its photons production stops. *(Right–panel)* $\tau^+\tau^-$ annihilation channel with $m_{\rm DM} = 100$ GeV in linear scale. For this leptonic channel, the spectral forms of the four codes differ on the whole energy range. We can see that the spectral cut-off at high energy is similar for both HERWIG codes and PYTHIA ones by pairs. In the interval $x \simeq 0.6 - 0.8$, simulated gamma–ray flux from PYTHIA 6.4 and HERWIG++ match. At $x \simeq 0.7$, PYTHIA 8 lies a factor 2-3 above HERWIG++ and PYTHIA whereas HERWIG lies the same factor below. Therefore there exists a non negligible difference (almost a factor ten), between PYTHIA 8 and HERWIG simulated spectra at this value of x.

Gamma–ray spectra from DM annihilation: $t\bar{t}$ channel

The most remarkable differences between the four simulations packages appear in the $t\bar{t}$ channel. To enable top decays in PYTHIA 6.4, the subroutine PYINIT() has to be executed. Alternatively, this process can be implemented by its dominant SM decay, i.e. $t \to W^+b$ (or equivalently $\bar{t} \to W^-\bar{b}$) [38]. In order to maintain any non-perturbative effect, the initial state was made of a four-particle state composed by W^+b coming from the t quark and $W^-\bar{b}$ from $\bar{t}$ anti-quark. These choices conserve all kinematics and color properties from the original pair and show the same results as the PYINIT() case. Starting from this configuration, we force decays and hadronization processes to evolve as PYTHIA does. Therefore, the gamma–ray spectra corresponding to this channel have also been included for PYTHIA 6.4 in our analysis using this procedure. For this channel we have studied two DM masses 500 GeV and 1 TeV. The simulated spectra appear very similar in the range $10^{-5} < x < 0.1$. Nonetheless, at lower and higher energies the four are quite different. At large energies, PYTHIA 8 gives the highest flux being able to acquire non-null flux for $x \approx 1$. The smallest flux is again for HERWIG++ whereas PYTHIA 6.4 and HERWIG lie in between the other two. These facts can be seen in Figs. 7.8 and 7.9. The four spectra also differ at high energy due to the (absence of) implementation

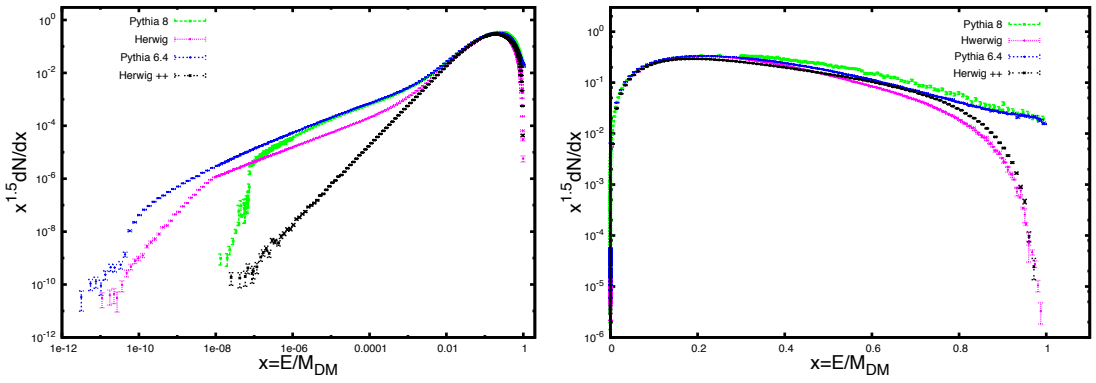

FIGURE 7.7: *(Left–panel)* $\tau^+\tau^-$ annihilation channel with $m_{\rm DM} = 1$ TeV in logarithmic scale. Compared to Fig. 7.6, all the lower cut-offs are shifted by a factor of ten to lower x's, with the exception of `PYTHIA` 6.4 that is shifted by a factor of a hundred, so that it never crossed `HERWIG` data as happened with $m_{\rm DM} = 100$GeV. *(Right–panel)* $\tau^+\tau^-$ annihilation channel with $m_{\rm DM} = 1$ TeV in linear scale. The behavior is analogous to the one discussed in Fig. 7.6.

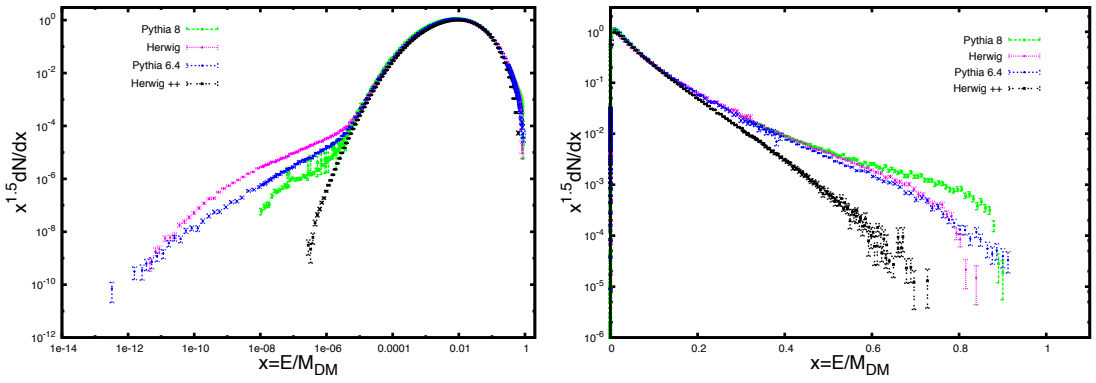

FIGURE 7.8: *(Left–panel)* $t\bar{t}$ annihilation channel with $m_{\rm DM}$ GeV in logarithmic scale. At low energy the simulations are consistent down to $x \simeq 10^{-5}$. `HERWIG++` drops down at $x \simeq 10^{-7}$ and `PYTHIA` 8 does at 10^{-9}, producing a higher number of photons 100 times bigger than `HERWIG++` at $x \approx 10^{-7}$, and almost 10 times lower of `PYTHIA` 6.4 at the same value of x. `PYTHIA` 6.4 cuts-off at $x \simeq 10^{-13}$ and `HERWIG` does at $x \simeq 10^{-12}$, where the two spectra match. For higher energies, `HERWIG` gamma–ray flux is higher than `PYTHIA` 6.4, with a maximum factor of ten at $x \simeq 10^{-9}$. *(Right–panel)* $t\bar{t}$ annihilation channel with $m_{\rm DM} = 500$ GeV linear scale. The four simulations are manifestly inconsistent between them at high energy. `HERWIG++` flux became lower from $x \simeq 0.2$ onwards and cuts off at $x < 0.8$. At $x \simeq 0.4$ `PYTHIA` 6.4 and `HERWIG` are similar between the statistical errors up to $x \approx 0.8$, where spectra and cuts-off become different. `PYTHIA` 8 starting from $x \simeq 0.6$ produces the highest flux with cut-off at $x \simeq 1$.

of Bremsstrahlung effects. All the possibilities were summarized in Table 7.1. At low energy the differences may be associated as in the $\tau^+\tau^-$ both to the cut-off in the lowest energy allowed for photons and to the presence or not of the `QEDRadiationHandler` in the simulation.

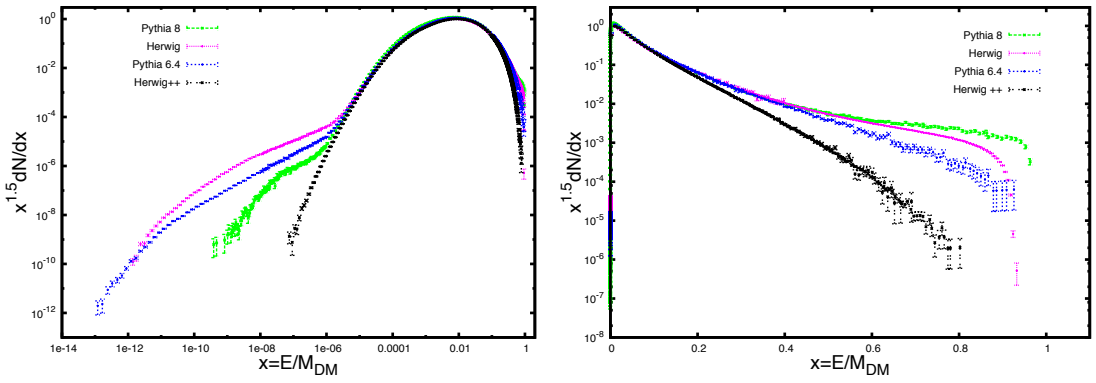

FIGURE 7.9: *(Left–panel)* $t\bar{t}$ annihilation channel with $m_{\rm DM} = 1$ TeV in logarithmic scale. At low energy the simulations are consistent down to $x \simeq 10^{-6}$. `HERWIG++` drops down at $x \simeq 10^{-7}$ and `PYTHIA` 8 does at $x \simeq 10^{-10}$, producing a higher number of photons that is 100 times higher than `HERWIG++` at $x \simeq 10^{-7}$, and almost 10 times lower than `PYTHIA` 6.4 at the same value of x. `PYTHIA` 6.4 cuts-off at $x \simeq 10^{-13}$ whereas `HERWIG` does at $x \simeq 10^{-12}$ where the two spectra match. For higher energies, `HERWIG` provides a higher flux with a maximum factor of ten at $x \simeq 10^{-8}$. *(Right–panel)* $t\bar{t}$ annihilation channel with $m_{\rm DM} = 1$ TeV in linear scale. The four simulations are all manifestly inconsistent between them at very high energy. `HERWIG++` flux becomes lower from $x \simeq 0.2$ onwards and cuts-off at $x < 0.8$. At $x \simeq 0.4$, `PYTHIA` 6.4 splits from `HERWIG` and `PYTHIA` 8 that remain with higher flux. `PYTHIA` 6.4 cuts-off before reaching $x = 1$, such as `HERWIG` does, although with very different spectral form and a separation of a factor ten at $x \simeq 0.8$. Finally, `HERWIG` also splits from `PYTHIA` 8 at $x \simeq 0.6$, producing the highest flux with cut-off at $x = 1$.

Package	Bremsstrahlung
`PYTHIA` 6.4	Implemented
`PYTHIA` 8	Implemented
`HERWIG`	Partially implemented
`HERWIG++`	Not implemented

TABLE 7.1: Simulations are strongly affected by the inclusion of Bremsstrahlung radiation and consequently the spectra turn out to look very different at high energy.

7.3 Implications to WIMPs phenomenology

Monte Carlo generators are essential tools for indirect searches of DM. The simulated spectra generated by `PYTHIA` 6.4, `PYTHIA` 8, `HERWIG` and `HERWIG++` allow to get predictions about the signal coming from DM annihilation and/or decay. The choice of the Monte Carlo generator may affect the predictions on both constraints and upper/lower limits to be imposed on DM annihilation cross section, relic density, astrophysical factor and other relevant quantities. As we discussed in the previous sections, the gamma–ray spectra look more similar at the energy corresponding to the peak of emission, but important differences appear at lower and higher energies. Lower energies are less important in the context of indirect searches, because of the dominance of astrophysical background components. However, the spectra at high energies could be fundamental.

As an illustrative example, the next CTA is expected to extend the accessible energy range from well below 100 GeV to above 100 TeV [91] and therefore may cover a wide range of high gamma–ray energies and signatures of DM annihilation in a wider range of masses than for instance FERMI-LAT satellite.

Since `PYTHIA` 8 includes both a good description of the t quark behavior and the QED radiation, we use it to compare with the other generators. We present the Monte Carlo relative deviation ($\Delta\mathrm{MC}_i$) with respect to `PYTHIA` 8 in Fig. 7.10, defined as

$$\Delta MC_i = \frac{MC_i - \mathrm{PYTHIA\,8}}{\mathrm{PYTHIA\,8}}, \tag{7.4}$$

where MC_i stands for `PYTHIA` 6.4, `HERWIG` and `HERWIG++`. For a DM mass of 1 TeV, the relative deviations are always less than 20% up to $x = 0.2$. For the whole high energy range, `PYTHIA` 6.4 produces typically less photons with a maximum relative error of 50% with respect to `PYTHIA` 8, apart from the $t\bar{t}$ channel for which the strong approximation leads to differences up to 100%. `HERWIG` exhibits deviations lower than 50% for the W^+W^- channel up to $x \simeq 0.6$, similar deviations are found for $b\bar{b}$ up to $x \simeq 0.5$ and for almost all the high energy range (up to $x = 0.8$) for $\tau^+\tau^-$. In the case of $t\bar{t}$ channel, deviations below 50% are found just below $x \simeq 0.3$. `HERWIG++` shows differences up to 100% for all the annihilation channels when the energy increases beyond those values.

On the other hand, the total number of photons produced by each event or multiplicity, also affects the constraints both in the sense of annihilations cross section and astrophysical factor. In indirect searches a typical significance of the signal between 2σ and 5σ with respect to the background is demanded. Apart from the specific characteristics of the detector, the flux of photons depends upon the DM density and the distance and distribution of the sources. All these dependences are taken into account by the astrophysical factor $\langle J \rangle$ and the boost factor b. Thus, two simulations should give different number of photons for the same number of events, this situation will affect the parameters $\langle J \rangle$ and b.

As we can see in Fig. 7.11, the multiplicity depends not only on the Monte Carlo event generator, but also on the energy of the event and the annihilation channel. In this study, we set a lower photon energy cut-off of $x_C = 10^{-5}$. It means that the energy cut-off increases with the DM mass. This kind of DM mass depending cut-off allows to reject photons of lower energies, where the simulations present important differences. However, the excluded range of the spectrum is not relevant for gamma-ray observations. This cut-off is also compatible with typical gamma-ray detectors energy thresholds. As an example, for a DM mass of 10 TeV, the corresponding energy cut lies at 100 MeV. Detector energy thresholds are typically around $1 - 10$ GeV depending on the particular

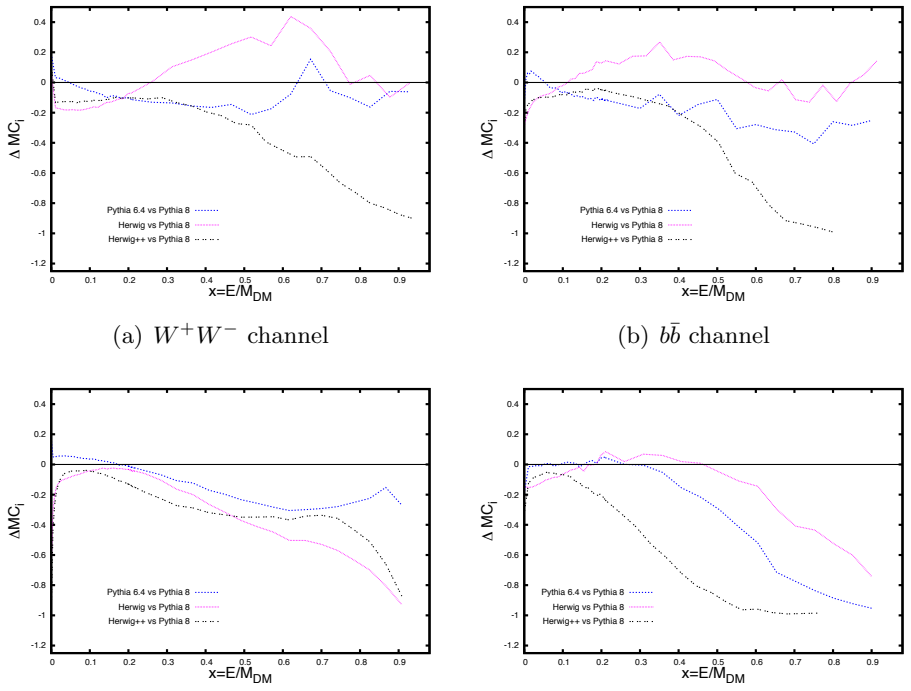

(a) W^+W^- channel (b) $b\bar{b}$ channel

(c) $\tau^+\tau^-$ channel (d) $t\bar{t}$ channel

FIGURE 7.10: Relative deviations versus x at $m_{\rm DM} = 1$ TeV. The full horizontal line at zero represents PYTHIA 8. The dashed blue line holds for PYTHIA 6.4 vs. PYTHIA 8, the dotted one is HERWIG Fortran vs. PYTHIA 8 and the two-dotted one is HERWIG++ vs. PYTHIA 8.

experimental device [37]. In any case, we have checked that our results and conclusions about the different multiplicities do not depend on the particular choice of this cut-off. Thus we have tested the robustness of our analysis with $x_C = 10^{-3}$ and $M_C = 1$ GeV. In most of the cases PYTHIA 6.4 gives the multiplicity upper limit, except for the $t\bar{t}$ annihilation channel – maybe due to the approximation of such process [38] – and $b\bar{b}$ channel at the range $m_{\rm DM} > 200$ GeV. On the other hand, the lower limit is given by HERWIG++ in most of the cases, except for W^+W^- and $b\bar{b}$ (the last one, up to $m_{\rm DM} > 200$ GeV) annihilation channel.

The multiplicity behavior is well approximated by the following power law relation with the DM mass:

$$\frac{N_\gamma}{N_{\chi\chi\to SM}} \simeq a_{\rm MC} \cdot \left(\frac{m_{\rm DM}}{1\,{\rm GeV}}\right)^{b_{\rm MC}} , \tag{7.5}$$

where the $a_{\rm MC}$ and $b_{\rm MC}$ coefficients depend on both the Monte Carlo simulator and the annihilation channel. When the SM particle is fixed, cosmological constraints obtained by means of the total number of generated gamma photons might depend on the Monte Carlo simulation. As in the previous analysis, in Table 7.2 we give the relations between the total number of photons generated by PYTHIA 6.4, HERWIG and HERWIG++ with respect to PYTHIA 8.

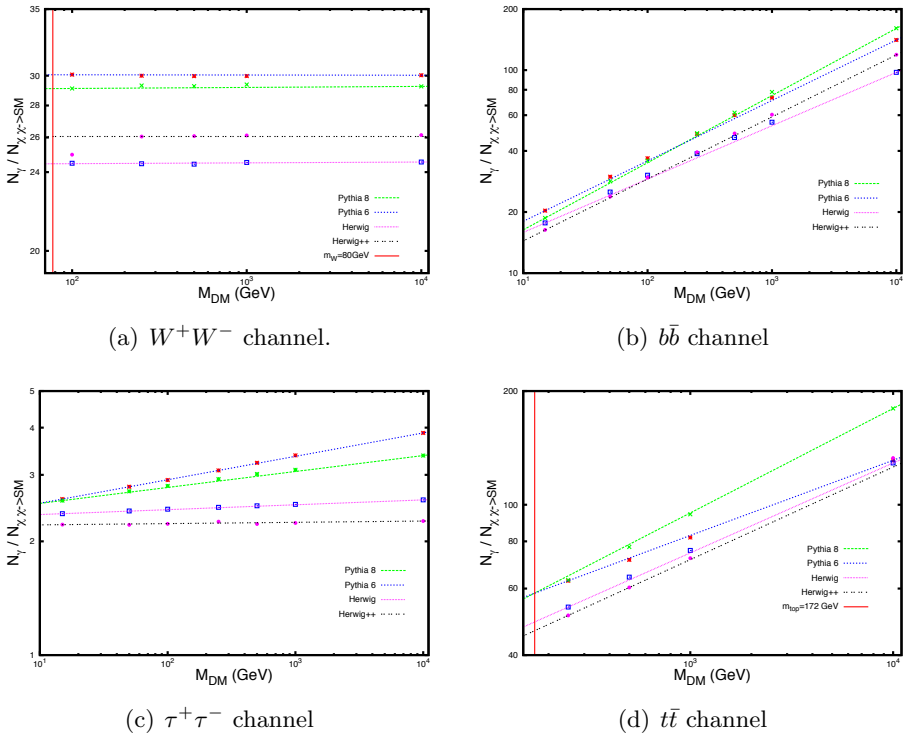

(a) W^+W^- channel. (b) $b\bar{b}$ channel

(c) $\tau^+\tau^-$ channel (d) $t\bar{t}$ channel

FIGURE 7.11: Multiplicity of the four Monte Carlo generators for each annihilation channel. W^+W^- annihilation channel (upper left panel): Regardless the DM mass value, PYTHIA 6.4 provides the upper limit to the number of generated photons, while HERWIG Fortran provides the lower limit with 23% difference between them; $b\bar{b}$ annihilation channel (upper right panel): At $m_{\rm DM} \sim 200$ GeV, the multiplicity of the two versions of PYTHIA is the same, as for the multiplicity of the HERWIG versions, but different between them. For that value of the mass, the relative deviation on multiplicity between PYTHIA and HERWIG codes almost attains 100%; $\tau^+\tau^-$ annihilation channel (lower left panel): The maximum difference between the four simulations multiplicities ranges between 20% at low energy up to 72% at higher energy; $t\bar{t}$ annihilation channel (lower right panel): Relative deviations run from 20% up to 30% depending on the energy of the event.

Let us summarize the situation as follows:

- W^+W^- **annihilation channel**: Roughly speaking PYTHIA 6.4 generates one more photon than PYTHIA 8 for each event, while HERWIG++ and HERWIG Fortran produce 3 and 5 photons less, respectively. Above $\simeq$ 200 GeV, this fact introduces a deviation on the multiplicity of $\sim 4\%$ between PYTHIA 6.4 and PYTHIA 8, of $\sim 16\%$ between HERWIG and PYTHIA 8 and of $\sim 10\%$ between HERWIG++ and PYTHIA 8. Between PYTHIA 6.4 and HERWIG in Fortan and HERWIG++ the deviation is $\sim 23\%$ and $\sim 15\%$, respectively. Finally, the deviation between HERWIG and HERWIG++ is $\sim 6\%$. For kinematic reasons, no photons are produced at energies lower than the mass of the W boson, that is the reason of the cut around $\simeq$ 80 GeV.

Software/PYTHIA 8	W^+W^-	$b\bar{b}$	$\tau^+\tau^-$	$t\bar{t}$
PYTHIA 6.4	$A_{\rm MC} = 1.04$ $B_{\rm MC} = 0$	$A_{\rm MC} = 1.18$ $B_{\rm MC} = -0.033$	$A_{\rm MC} = 0.96$ $B_{\rm MC} = 0.020$	$A_{\rm MC} = 1.49$ $B_{\rm MC} = -0.077$
HERWIG	$A_{\rm MC} = 0.84$ $B_{\rm MC} = 0$	$A_{\rm MC} = 1.13$ $B_{\rm MC} = -0.068$	$A_{\rm MC} = 1.00$ $B_{\rm MC} = -0.029$	$A_{\rm MC} = 1.02$ $B_{\rm MC} = -0.038$
HERWIG++	$A_{\rm MC} = 0.90$ $B_{\rm MC} = 0$	$A_{\rm MC} = 0.93$ $B_{\rm MC} = -0.025$	$A_{\rm MC} = 0.96$ $B_{\rm MC} = -0.039$	$A_{\rm MC} = 0.93$ $B_{\rm MC} = -0.031$

PYTHIA 8	$a_{\rm MC} = 28.9$ $b_{\rm MC} = 0.001$	$a_{\rm MC} = 7.62$ $b_{\rm MC} = 0.331$	$a_{\rm MC} = 2.29$ $b_{\rm MC} = 0.042$	$a_{\rm MC} = 14.1$ $b_{\rm MC} = 0.276$

TABLE 7.2: Relative behaviors in the total number of photons produced by PYTHIA 6.4, HERWIG and HERWIG++ with respect to PYTHIA 8 in the range 15 GeV - 10 TeV. Here $A_{\rm MC} = a_{MC_i}/a_{\texttt{PYTHIA 8}}$ and $B_{\rm MC} = b_{MC_i} - b_{\texttt{PYTHIA 8}}$. PYTHIA 8 multiplicity parameters are listed at the end of the Table.

- $b\bar{b}$ **annihilation channel**: At $m_{\rm DM} \simeq 200$ GeV, the deviation between the multiplicity of the two versions of PYTHIA is the less than 1%, as for at 100 GeV and HERWIG versions, but different between them. At 150 GeV, the number of photons produced by the Fortran versions of PYTHIA code is a 22% bigger than the HERWIG one. For masses below ~ 200 GeV the upper limit is given by PYTHIA 6.4 whereas the lower one is provided by HERWIG++. At 10 TeV the deviation reach the maximum value of $\sim 13\%$, $\sim 40\%$ and $\sim 26\%$ between PYTHIA 6.4, HERWIG, HERWIG++ and PYTHIA 8, respectively. On the other hand, at $m_{\rm DM} > 200$ GeV PYTHIA 8 gives the upper limit and HERWIG Fortran the lower one.

- $\tau^+\tau^-$ **annihilation channel**: The number of photons per event produced by the four Monte Carlo generators is very similar for this channel, but very low. This fact introduces a very important difference, that reach the maximum of $\sim 42\%$ at 10 TeV between PYTHIA 6.4 and HERWIG++. PYTHIA 6.4 gives here the upper limit, followed by PYTHIA 8, HERWIG Fortran and HERWIG++. At lower energies the difference between upper and lower limit is less than 20%, and increases up to 72% at higher DM mass.

- $t\bar{t}$ **annihilation channel**: As in the case of W^+W^- channel, no photons are produced at energies lower than the mass of the top quark because of kinematic reason. Always PYTHIA 8 gives here the upper limit, followed by PYTHIA 6.4, HERWIG Fortran and HERWIG++. All the multiplicities depend on the DM mass in a exponential way, but with different exponents. At lower energies the deviation between upper and lower limits is about 20%, and around 30% for events at higher energies.

7.4 Conclusions

We have analyzed the gamma–ray spectra produced by four Monte Carlo event generator codes, namely `PYTHIA` 6.4, `PYTHIA` 8, `HERWIG` Fortran and `HERWIG++`. These spectra have been largely used in the framework of DM indirect searches and the differences between them may affect the results for those investigations. Although gamma–ray spectra have been generated for DM annihilating in all possible quark-antiquark, leptonic and bosons channels, we chose to show a representative sample of them ($b\bar{b}$ for the quark-antiquark case, $\tau^+\tau^-$ for the leptonic one and W^+W^- boson annihilation channels). We also included the particular case of the $t\bar{t}$ and studied it separately.

Around the energy of maximum flux, where the simulations are well fitted to LEP or LHC data, the differences between packages are less than 20%. This statement is always true in the range $0.01 < x < 0.2$ with possible extension of the range depending on the annihilation channel and the energy of the event (see the bulk of this communication for further details). On the one hand, at lower energy the spectra appear very different between them, depending strongly on the cut-off set for the minimal allowed energy in the parton shower. On the other hand, differences also appear at higher energy. For all the studied channels, the implementation absence of Bremsstrahlung radiation generated by high-energy leptons in `HERWIG++` leads to a smaller number of high-energy photons when compared to the other codes. Moreover, in the case of the $t\bar{t}$ annihilation channel, there is an additional effect due to the fact that the top quark behavior phenomenology has been improved in the codes released in the last years. Thus, whereas for `PYTHIA` 6.4 this channel was approximated through the decay into W and b, higher-order effects have been included in the newest code generations. Due to the combination of these two factors, we conclude that the most reliable Monte Carlo event generator code for gamma–ray spectra is `PYTHIA` 8. For this reason we got estimations for the relative deviations for `PYTHIA` 6.4, `HERWIG` Fortran and `HERWIG++` with respect to `PYTHIA` 8.

We conclude that further implementation is needed in `HERWIG++` in order to improve its competitiveness in the gamma–ray sector. For the other three Monte Carlo event generators under study in this work, the gamma–ray spectra simulated show also important differences. Without taking into account very low energies, the relative deviations can only be bounded by 50% for the hadronic ($b\bar{b}$) and electro-weak channels (W^+W^-). The situation for the $t\bar{t}$ channel and the leptonic ones ($\tau^+\tau^-$) is even worse. At high energies, the discrepancies can reach 100%. In fact, the photon fluxes predicted by the different generators can differ in several orders of magnitude. On the other hand, the situation for the total number of produced photons improves a little, and the maximum difference is a factor 2 within the studied mass region.

These significative differences can play an important role in misunderstanding DM signatures. For example, in a DM study, once the astrophysical factor is obtained by fitting the DM gamma–ray spectra, these discrepancies may introduce a deviation on the boost factor proportional to the difference of the multiplicity. This effect can be easily estimated with the help of Eq. (7.5) and Table 7.2. However, we have shown that the simulated spectral shapes can be very different and this fact may have a large impact in the analysis.

Chapter 8

Conclusions

As discussed so far, cosmology and particle physics lie at the basis of our fundamental understanding of the Universe as a whole. Nevertheless, most of the contents of the Universe remain still unknown; the 69.2% of the total mass-energy content is made of dark energy and the 26.8% is DM. So far, DM manifests itself only by gravitational effects. Although some alternative theories of gravity have been proposed, the most widely accepted explanation for these phenomena is that DM exists and that it is composed of WIMPs. Many DM candidates have been proposed beyond the SM, such as a supersymmetric and Kaluza-Klein particles and branons. They include a large amount of thermal candidates, but also no-thermal or self-interacting models (Chapter 1). Particle accelerators such as the LHC and underground experiments as DAMA, CDMS/superCDMS, ZEPLIN, XENON and LUX among others, have been developed in the context of direct search, where DM is expected to interact with atomic nuclei at the Earth. However, the most searches in colliders and underground experiments have been focused so far on energy scales below 1 TeV, while the cosmological thermal limit on DM masses is around 100 TeV. For the indirect search, many ground-based Cherenkov experiments as HESS, HAWC, and the future CTA among the others, are involved in DM searches, as well as neutrino experiments as ANTARES, IceCube or future KM3NeT and satellite detectors as AMS, FERMI-LAT and PAMELA. Indirect experiments detect secondary cosmic-ray fluxes generated by DM annihilation or decay into SM particles in astrophysical sources. While direct detection experiments are able to set stringent constraints only on low-mass WIMPs, high energy scales are investigated by indirect searches (Chapter 2). At present, searches for DM have not yet yielded to a clear discovery.

In this thesis, we have shown that TeVDM particles with masses appear as a candidate to explain HESS J1745-290 gamma-ray signals from the GC. Previous studies analyzed the same source in the context of DM model dependent fit, concluding that the data were not compatible with Kaluza-Klein or minimal supersymmetric DM candidates. In

contrast, the new analysis developed in this thesis is model independent. It is also consistent with gamma-ray data from the same region, published by the FERMI-LAT collaboration. Such data can be explained as a background component in gamma-rays that modify the HESS J1745-290 cut-off at 30 TeV as a power-law component at energies around 100 GeV. The analysis shows good agreement with DM annihilation or decay into $u\bar{u}$, $d\bar{d}$, $s\bar{s}$ and $t\bar{t}$ quark-antiquark channels and W^+W^- and ZZ boson channels for DM masses between $10 - 100$ TeV. Leptonic and other quark-antiquark channels were excluded with 95.4% confidence level (Chapter 3).

Branons represent a good TeVDM candidate. At these high energies, branons annihilate mostly in boson channels. A branon DM with mass $m_{\rm DM} \simeq 50.6$ TeV, provides an excellent fit to HESS GC data. The corresponding background being compatible with FERMI-LAT data. The compatibility of its thermal abundance with the WMAP constraints, demands a cross section of $\langle\sigma v\rangle = (1.14\pm0.19)\cdot10^{-26}$ cm^{3}s^{-1}, what is equivalent to a brane tension of $f \simeq 27.5$ TeV. Such a value of the annihilation cross section is the expected one for a thermally produced candidate. In order to better investigate the hypothesis of branon candidate for DM, we have set constraints on the sensitivity of several gamma-ray detectors to branon DM annihilating in dSph galaxies and in the GC. In particular, we found that the next generation of Cherenkov telescopes with increased effective areas and angular resolution could detect or set additional constraints on this type of DM. On the other hand, satellite telescopes are able to set less stringent limits on such high energies. The sensitivity was constrained independently of enhancements related to the presence of substructures or non-thermal particles (Chapter 4).

In the GC, a particulary high value for the astrophysical factor is needed in order to fit the HESS data. In fact, the emission region of the HESS gamma-ray source is quite compact since the signal is limited to a region of few tenths of degree. This feature is not consistent with dark halos simulated with non-baryonic cold DM, such as the standard NFW profile, and could also address to a kind of local enhancement or substructure. It needs to be more compact as the ones produced when baryonic effects are taken into account. It has been argued that the baryonic gas falls to the inner part of the halo, modifying the gravitational potential and increasing the DM density in the center. This scenario is not completely accepted, but if it is correct, it has two important consequences. First, the sensitivity of indirect DM searches is reduced to a more compressed region; and second, the DM annihilating fluxes are enhanced by up to three orders of magnitude with respect to the standard NFW profile. The HESS observations are in good agreement with these types of compressed dark halos.

When the DM mass and astrophysical factor are fixed by the gamma-ray fit, the analysis of several other cosmic-ray fluxes can verify or reject such DM hypothesis. The study of the expected production of neutrinos from such a kind of enhanced TeVDM clump at the GC shows that in order to be sensitive to this model, neutrino detectors

such as ANTARES or IceCube need improved effective areas and angular resolution with respect to present observational conditions. In particular, we have done an explicit analysis for 48.8 TeV DM annihilating in W^+W^- and 27.9 TeV DM annihilating into $u\bar{u}$ channel. In these cases, the neutrino fluxes are completely determined by assuming that the DM region is localized as it is imposed by the gamma-ray analysis. We have estimated the best combinations of energy cuts, observation times and angular resolutions of a general high energy neutrino telescope. For this purpose, we have used the IceCube atmospheric neutrino observations as background. We have also compared our results with the recent observation of 37 high energy neutrinos over the range 30 TeV $-$ 1 PeV at 4.1σ of confidence level, and $t_{\rm exp} = 662$ days ($\simeq 1.8$ years). Of these events, 5 are likely originated from the GC. These neutrinos seem to have an astrophysical origin, but the spectrum and direction are not compatible with the signal studied in this work (the angular resolution in the muon track events is of $\theta \approx 8^\circ$). In fact, we have found that for DM annihilating into the W^+W^- boson channel, we need a resolution angle $0.18^\circ \lesssim \theta \lesssim 0.72^\circ$ and low energy cut-off $818\,\text{GeV} \lesssim E^\nu_{\rm min} \lesssim 1811$ GeV to get a signal between 5σ and 2σ with a minimum of 2 years of exposition time and a maximum of five years for a 50 m^2 of detector effective area. The mass associated with light quark channels, such as the $u\bar{u}$ annihilation, is significantly smaller. It implies that the neutrino flux produced in this case is less energetic, and more difficult to discriminate from the background (Chapter 5).

Finally, we have studied the antiproton propagation function for a point-like source at the GC. In general, this function depends on both the morphology of the source and its spectra. We have analyzed the flux at the TOA for three emission spectra, namely a power law flux, monochromatic emission, or to annihilating or decaying DM. These analyses may be associated to a large variety of astrophysical sources. We have compared such flux with the present PAMELA antiproton data. In the case of the DM, there are two reasons for the analysis of the point-like emission. On the one hand, as discussed before, DM can be compacted around a very localized region in the center of our galaxy for different processes, as the baryonic compression or black hole effects. On the other hand, numerical computations of the diffusion equation present a singularity at the GC, because of the central behaviour of DM halos density profiles. This divergence needs to be regularized. For that, we consider its contribution separately as a point-like source. In any case, the contribution from the local continuous NFW DM halo profile is expected to be important and the interplay between both contributions gives a rich phenomenology (Chapter 6).

To conclude, we have discussed the uncertainty related to Monte Carlo simulations in indirect searches of DM. In order to search for a DM signal in cosmic-ray fluxes, the secondary fluxes are simulated by means of Monte Carlo event generator codes. Although in principle we would expect a good agreement between different Monte Carlo codes

at intermediate energies, and a larger difference at lower and higher energy scales, in practice, after analyzing the gamma-ray spectra we found important differences in the whole energy range. As an example, we have studied `PYTHIA` 6.4, `PYTHIA` 8, `HERWIG` Fortran and `HERWIG++`. On the one hand, at lower energy the spectra appear very different between them, depending strongly on the cut-off set for the minimal allowed energy in the parton shower. On the other hand, differences also appear at higher energy. For all the studied channels, the absence of the implementation of Bremsstrahlung radiation generated by high-energy leptons in `HERWIG++` leads to a smaller number of high-energy photons when compared to the other codes. Moreover, in the case of the $t\bar{t}$ annihilation channel, there is an additional effect due to the fact that the top quark behavior phenomenology has been improved in the codes released in the last years. These differences may introduce a deviation on the estimation of the boost factor proportional to the difference on the multiplicity (Chapter 7).

Keeping in mind the conclusion of this thesis, we would introduce some prospectives for next investigations. The study of the HESS data in gamma-rays gives good fits for annihilation of DM into boson channels and some quark-antiquark channel too, with mass above 10 TeV scale. Viable WIMP models require appropriate masses and pair annihilation/creation cross section to produce the observed DM thermal relic density. If DM is thermal, the enhancement needed at the GC to fit the HESS data has to be justified and related with the DM density distribution in the region. If the DM particle is not thermal, different values for the annihilation cross section are allowed and the enhancement should be model dependent. So far, the complementary study between particle accelerator and direct and indirect searches have been performed for low mass DM particles, due mainly to experimental limits. The better sensibility of the next generation of direct search experiments at TeV scale such as LUX, DARWIN or XENON, may give important results. An additional aim may be to extend the phenomenological study in the context of indirect searches, for example with next HAWC and CTA experiments that will yield new data above the TeV scale in the next years. Moreover, electromagnetic radiation of different wavelengths is emitted by DM through different physical mechanisms, such as inverse Compton scattering or synchrotron emission, depending on the DM properties. Cross-correlation between different signals (radio-gamma, radio-X and X-gamma) in the anisotropic sky or between a multi-wavelength DM signal with specific gravitational tracers could also provides an alternative way to determine the nature of TeVDM.

Appendix A

Fitting Function Parameters

In the following tables, we show explicitly the parameters used in the fitting functions. The precision associated with them are better than 10%. An extrapolation of PYTHIA results is necessary for high energies. This fact is justified since the mass dependence of the fitting parameters reaches an asymptotic behavior for energies higher than 1 TeV depending on the particular channel and parameter (read [38] for further details).

Parameter	Fitting power law(s)
p_1	$4530 m_{\rm DM}^{0.653}$
q_1	$0.00230 m_{\rm DM}^{-0.911} + 0.00291 m_{\rm DM}^{0.0348}$
l_1	$0.626 m_{\rm DM}^{-0.0300} + 16.4 m_{\rm DM}^{-1.34}$

TABLE A.1: Mass dependent parameters for the fitting function of the photon spectrum coming from the $\mu^+\mu^-$ channel.

Parameter	Fitting power law
n_1	$-7.00 m_{\rm DM}^{-1.99} + 179 m_{\rm DM}^{-0.763} + 9.09$
p_1	$3.07 m_{\rm DM}^{1.55}$

Channel	a_1	b_1	b_2	n_2	c_1	d_1	c_2	d_2	q_1
τ	14.7	5.40	5.31	1.40	2.54	0.295	0.373	0.470	0.00260

TABLE A.2: Mass dependent and independent parameters for the $\tau^+\tau^-$ channel fitting function.

Parameter	Fitting power law
b_1	$2.96 m_{\rm DM}^{0.0506}$
n_1	$2.91 m_{\rm DM}^{-0.351} + 1.90 m_{\rm DM}^{0.0172}$
n_2	$0.0587 m_{\rm DM}^{0.146} + 0.848 m_{\rm DM}^{-0.145}$
d_1	$0.317 m_{\rm DM}^{-0.0300} + 0.403 m_{\rm DM}^{-0.351}$
p_1	$4.74 m_{\rm DM}^{0.839}$

Channel	a_1	b_2	c_1	c_2	q_1
$u\bar{u}$	5.58	5.50	0.315	0.0	$9.30 \cdot 10^{-4}$

TABLE A.3: Parameters for the $u\bar{u}$ channel fitting function.

Parameter	Fitting power law
b_1	$3.39 m_{\rm DM}^{0.0485}$
n_1	$21.8 m_{\rm DM}^{-0.993} + 2.25 m_{\rm DM}^{-0.00113}$
n_2	$0.848 m_{\rm DM}^{-0219} + 0.161 m_{\rm DM}^{0.0573}$
c_1	$0.722 m_{\rm DM}^{-0.270} + 0.0544 m_{\rm DM}^{0.0874}$
p_1	$0.168 m_{\rm DM}^{1.29}$

Channel	a_1	b_2	d_1	c_2	q_1
$d\bar{d}$	5.20	5.10	0.410	0.0260	$1.40 \cdot 10^{-4}$

TABLE A.4: The analogous set of parameters shown in Tab. A.3 but for the $d\bar{d}$ channel.

Parameter	Fitting power law
b_1	$4.54 m_{\rm DM}^{0.0339}$
n_2	$3.68 m_{\rm DM}^{-1.01} + 0.744 m_{\rm DM}^{-0.0352}$
d_1	$0.621 m_{\rm DM}^{-0.674} + 0.414 m_{\rm DM}^{-0.0588}$
p_1	$12.8 m_{\rm DM}^{0.732}$

Channel	a_1	n_1	b_2	c_1	q_1
$s\bar{s}$	4.83	2.03	6.50	0.335	$2.40 \cdot 10^{-4}$

TABLE A.5: Parameters for the fitting function of the photon spectrum coming from DM annihilation in $s\bar{s}$ channel.

Parameter	Fitting power law
b_1	$9.90 m_{\rm DM}^{-0.130}$
n_1	$4.14 m_{\rm DM}^{-0.148}$
c_1	$0.210 m_{\rm DM}^{0.0951}$
d_1	$1.50 m_{\rm DM}^{-0.632} + 0.479 m_{\rm DM}^{-0.0942}$
p_1	$8.11 m_{\rm DM}^{0.812}$

Channel	a_1	b_2	n_2	c_2	q_1
$c\bar{c}$	5.58	7.90	0.686	0.0	$9.00 \cdot 10^{-4}$

TABLE A.6: The same as in Tab. A.3 for the $c\bar{c}$ channel.

Parameter	Fitting power law
b_1	$152 m_{\rm DM}^{-0.462}$
n_1	$18.7 m_{\rm DM}^{-0.248}$
n_2	$0.707 m_{\rm DM}^{-0.0129}$
c_1	$0.328 m_{\rm DM}^{0.0447}$
d_1	$0.449 m_{\rm DM}^{-0.0552}$
p_1	$11.8 m_{\rm DM}^{0.641}$

Channel	a_1	b_2	c_2	d_2	q_1
$b\bar{b}$	10.0	11.0	0.0151	0.550	$2.60 \cdot 10^{-4}$

TABLE A.7: Parameters for the $b\bar{b}$ channel fitting function.

Parameter	Fitting power law(s)
b_1	$16.4 m_{\mathrm{DM}}^{-0.0400}$
n_1	$0.559 m_{\mathrm{DM}}^{-0.0379}$
c_2	$8910 m_{\mathrm{DM}}^{-3.23}$
p_1	$5.78 \cdot 10^{-5} m_{\mathrm{DM}}^{1.89}$
q_1	$0.133 m_{\mathrm{DM}}^{0.488}$
l_1	$21.9 m_{\mathrm{DM}}^{-0.302}$

Channel	a_1	c_1	d_1	d_2
$t\bar{t}$	290	1.61	0.19	0.845

TABLE A.8: Mass depend and independent parameter of the fitting function given by Eq. (3.10) for the $t\bar{t}$ channel.

Channel	a_1	n_1	q_1
W	25.8	0.510	3.00
Z	25.8	0.5	3.87

Channel	b_1	c_1	d_1
W^+W^-	$9.29 m_{\mathrm{DM}}^{-0.0139}$	$0.743 m_{\mathrm{DM}}^{0.0331}$	$0.265 m_{\mathrm{DM}}^{-0.0137}$
ZZ	$9.36 m_{\mathrm{DM}}^{-0.00710}$	$0.765 m_{\mathrm{DM}}^{0.00980}$	$0.272 m_{\mathrm{DM}}^{-0.00990}$

Channel	p_1	j_1
W^+W^-	$10^5 m_{\mathrm{DM}}^{-1.13} + 285 m_{\mathrm{DM}}^{0.0794}$	$0.943 m_{\mathrm{DM}}^{0.00852}$
ZZ	$85505 m_{\mathrm{DM}}^{-0.166} + 0.476 m_{\mathrm{DM}}^{0.984}$	$0.884 m_{\mathrm{DM}}^{0.0175}$

TABLE A.9: Parameters for the fitting functions of the electroweak gauge bosons channels.

Bibliography

[1] http://map.gsfc.nasa.gov/media/060915/index.html.

[2] A. Einstein, Annalen der Physik, 18:639 (1905); A. Einstein, Sitzungsberichte der Preussischen Akademie der Wissenschaften zu Berlin, 844 - 847 (1915).

[3] A.G. Riess et al. Astron. J. 116,1009 (1998); S. Perlmutter et al. Astrophys. J. 517, 565 (1999).

[4] S. Dodelson, *Modern Cosmology*, Academic Press (2003); E. W. Kolb and M. S. Turner, *The Early Universe* (1990); S. Capozziello and M. Funaro, *Introduzione alla Relativitá Generale*, Liguori Editore (2005); A. L. Maroto and J. Ramirez, [arXiv:astro-ph/0409280].

[5] J.C. Mather et al., The Astrophysical Journal, Part 1 (ISSN 0004-637X), vol. 420, no. 2, p. 439-444E. Komatsu *et al.* [WMAP Collaboration], ApJ. Suppl. 192 18 (2011); Planck Collaboration (Ade, P.A.R. et al.) A&A (2014) arXiv:1303.5076 [astro-ph.CO]

[6] P. J. E. Peebles, *The large-scale structure of the universe*, Princeton University Press, Priceton, USA (1980).

[7] G. Gentile, P. Salucci, MNRAS 351: 903-922 (2004), [arXiv:astro-ph/0403154]; A. Klypin, A. V. Kravtsov, O. Valenzuela, F. Prada, ApJ 522: 82 (1999); M. Pawlowski et al., MNRAS (2014) [arXiv:1406.1799]; P. Kroupa, B. Famaey, K. S. de Boer, J. Dabringhausen, M. Pawlowski, C. Boily, H. Jerjen, D. Forbes, G. Hensler, A&A 523: 32-54 (2010), [arXiv:1006.1647].

[8] P. S. B. Dev, A. Mazumdar, S. Qutub, MAN/HEP/2013/23 (2013), [arXiv:1311.5297].

[9] Planck Collaboration (P.A.R. Ade et al.), Astron.Astrophys. 571 (2014) A16 [arXiv:1303.5076], Planck Collaboration (P. A. R. Ade et al.) [arXiv:1502.01589].

[10] A. H. Guth, Phys. Rev. D 23, 347 (1981); A. R. Liddle, D. H. Lyth, *Cosmological Inflation and Large Scale Structures*, Cambridge University Press (2000).

[11] S. van de Bergh, [arXiv:astro-ph/9904251];

[12] Rubin, V.C., Ford, W.K. and Thonnard, N. (1980), Astrophys. J. 238, 471; Broeils, A.H. (1992), Astron. Astrophys. 256, 19; Broeils, A.H. and Courteau, S. (1997), in M. Persic and P. Salucci (Eds.), ASP Conference Series 117.

[13] J. F. Navarro, C. S. Frenk and S. D. M. White, Astrophy. J. 462 (1196) 563[arXiv:astro-ph/9508025]; A. W. Graham, D. Merritt, B. Moore, J. Diemand and B. Terzic, Astron. J. 132 (2006) 2685[arXiv:astro-ph/0509417]; J. F. Navarro et al. [arXiv:astrp-ph0810.1522]; K. G. Begeman, A. H. Broelis, R. H. Sanders, MNRAS 249, 523 (1991). J. N. Bahcall and R. M. Soneira, Astrophys. J. Sull. 44,73 (1980); A. Burkert, IAU Symp. 171 (1996) 175 Astrophys. J. 447 (1995) L25 [arXiv:astro-ph/9504041].

[14] F. Iocco, M. Pato, G. Bertone, Nature Physics (2015), doi:10.1038/nphys3237.

[15] F. Prada, A. Klypin, J. Flix Molina, M. Martínez, E. Simonneau, Phys. Rev. Lett. **93**, 241301 (2004).

[16] M. Bradac et al. Astro. J., 652:937-947 (2006); M. Bartelmann Review talk at "Dark Matter and Energy in Clusters of Galaxy", Taipeh 2002; C. Lage and G. Farrar, Astro. J., 787:144(19pp) (2014).

[17] M. Milgrom, Acta Phys.Polon. B32 (2001) 3613 [arXiv:astro-ph/0112069].

[18] W. Hu and M. White, Scientific American 290N2 44 (2004).

[19] S. Gardner and G. Fuller, Progress in Particle and Nuclear Physics 07/2013, [arXiv:1303.4758].

[20] V. Cirigliano, S. Profumo and M. J. Ramsey-Musolf, JHEP, 0607:002 (2006) [arXiv:hep-ph/0603246].

[21] K. M. Zurek, Phys. Rev. D 79,115002 (2009) [arXiv:0811.4429]; J. L. Feng, M. Kamionkowski and S. K. Lee, Phys. Rev. D 82,015012 (2010)[arXiv:1004.4213].

[22] T. Kaluza, Sitzungsber. Preuss. Akad. Wiss. Berlin (Math. Phys.), 1921:966-972 (1921); O. Klein, Z. Phys. 37:895-906 (1926).

[23] G. Bertone, *Particle Dark Matter*, Cambridge University Press (2010); C. Muñoz, Int. J. Mod. Phys. A19. 3093-3170 (2004).

[24] J. A. R. Cembranos, A. Dobado and A. L. Maroto, Phys. Rev. Lett. **90**, 241301 (2003); T. Kugo and K. Yoshioka, Nucl. Phys. B **594**, 301 (2001); J. A. R. Cembranos, A. Dobado and A. L. Maroto, AIP Conf. Proc. **670**, 235 (2003); hep-ph/0402142; hep-ph/0406076; hep-ph/0411076; astro-ph/0411262; Int. J. Mod.

Phys. D **13**, 2275 (2004) [hep-ph/0405165]; astro-ph/0503622; astro-ph/0512569; astro-ph/0611911; A. L. Maroto, Phys. Rev. D **69**, 043509 (2004); Phys. Rev. D **69**, 101304 (2004); J. A. R. Cembranos *et al.*, 0708.0235 [hep-ph]; JCAP **0810**, 039 (2008)

[25] R. Sundrum, Phys. Rev. D **59**, 085009 (1999); M. Bando *et al.*, Phys. Rev. Lett. **83**, 3601 (1999); A. Dobado and A. L. Maroto, Nucl. Phys. B **592**, 203 (2001); J. A. R. Cembranos, A. Dobado and A. L. Maroto, Phys. Rev. D **65** 026005 (2002); hep-ph/0107155

[26] J. Alcaraz *et al.*, Phys. Rev. D **67**, 075010 (2003); J. A. R. Cembranos, A. Dobado and A. L. Maroto, Phys. Rev. D **70**, 096001 (2004)

[27] J. A. R. Cembranos, J. L. Diaz-Cruz, L. Prado, Phys. Rev.D 84, 083522 (2011), [arXiv:1110.0542v1].

[28] P. Achard *et al.*, Phys. Lett. B **597**, 145 (2004)

[29] P. Creminelli and A. Strumia, Nucl. Phys. B **596** 125 (2001)

[30] J. A. R. Cembranos, A. Dobado and A. L. Maroto, Phys. Rev. D **73**, 035008 (2006); Phys. Rev. D **73**, 057303 (2006)

[31] L. Covi, J. E. Kim and L. Roszkowski, Phys. Rev. Lett. **82**, 4180 (1999);J. L. Feng, A. Rajaraman and F. Takayama, Phys. Rev. D **68**, 085018 (2003); J. L. Feng, A. Rajaraman and F. Takayama, Int. J. Mod. Phys. D **13**, 2355 (2004); J. A. R. Cembranos, J. L. Feng, A. Rajaraman and F. Takayama, Phys. Rev. Lett. **95**, 181301 (2005); J. A. R. Cembranos, J. L. Feng, L. E. Strigari, Phys. Rev. D **75**, 036004 (2007); J. A. R. Cembranos, Phys. Rev. Lett. **102**, 141301 (2009); Phys. Rev. D **73**, 064029 (2006); J. A. R. Cembranos, J. L. Diaz-Cruz and L. Prado, Phys. Rev. D **84**, 083522 (2011).

[32] H. Goldberg, Phys. Rev. Lett. **50**, 1419 (1983); J. R. Ellis *et al.*, Nucl. Phys. B **238**, 453 (1984); K. Griest and M. Kamionkowski, Phys. Rep. **333**, 167 (2000); J. A. R. Cembranos, A. Dobado and A. L. Maroto, Phys. Rev. Lett. **90**, 241301 (2003); Phys. Rev. D **68**, 103505 (2003); Phys. Rev. D **73**, 035008 (2006); Phys. Rev. D **73**, 057303 (2006); A. L. Maroto, Phys. Rev. D **69**, 043509 (2004); Phys. Rev. D **69**, 101304 (2004); A. Dobado and A. L. Maroto, Nucl. Phys. B **592**, 203 (2001); Int. J. Mod. Phys. **D13**, 2275 (2004) [hep-ph/0405165]; J. A. R. Cembranos *et al.*, JCAP **0810**, 039 (2008).

[33] J. Alcaraz *et al.*, Phys. Rev.**D67**, 075010 (2003); P. Achard *et al.*, Phys. Lett. **B597**, 145 (2004); Europhys. Lett. **82**, 21001 (2008); J. A. R. Cembranos, A. Dobado and

A. L. Maroto, Phys. Rev. **D65** 026005 (2002); J. Phys. A **40**, 6631 (2007); Phys. Rev. **D70**, 096001 (2004); J. A. R. Cembranos *et al.*, AIP Conf. Proc. **903**, 591 (2007).

[34] J. A. R. Cembranos and L. E. Strigari, Phys. Rev. D **77**, 123519 (2008); J. A. R. Cembranos, J. L. Feng and L. E. Strigari, Phys. Rev. Lett. **99**, 191301 (2007).

[35] M. Cirelli et al. JCAP **1103**, 051 (2011) [Erratum-ibid. **1210**, E01 (2012)].

[36] J. A. R. Cembranos, V. Gammaldi and A. L. Maroto, Phys. Rev. D **86**, 103506 (2012); arXiv:1302.6871 [astro-ph.CO].

[37] J. A. R. Cembranos, A. de la Cruz-Dombriz, V. Gammaldi and A. L. Maroto, Phys. Rev. D **85**, 043505 (2012).

[38] J. A. R. Cembranos, A. de la Cruz-Dombriz, A. Dobado, R. Lineros and A. L. Maroto, Phys. Rev. D **83**, 083507 (2011); AIP Conf. Proc. **1343**, 595-597 (2011); J. Phys. Conf. Ser. **314**, 012063 (2011); A. de la Cruz-Dombriz and V. Gammaldi, arXiv:1109.5027 [hep-ph]; http://teorica.fis.ucm.es/PaginaWeb/photon_spectra.html

[39] A.V. Belikov, G. Zaharijas, J. Silk, Phys. Rev. D 86, 083516 (2012).

[40] $http://www.mpi-hd.mpg.de/lin/research\_DM.en.html$.

[41] P. J. Fox, R. Harnik, J. Kopp, Y. Tsai (Fermilab), Phys. Rev. D 85, 056011 (2012).

[42] The CMS Collaboration, Nature Physics 10, 557-560 (2014), doi:10.1038/nphys3005.

[43] M. W. Goodman and E. Witten, Phys. Rev. D 31, 3059 (1985); A. Drukier and L. Stodolsky, Phys. Rev. D 30, 2295 (1984); L. Baudis, [arXiv:1408.4371].

[44] J. Fan, M. Reece, L. Wang, JCAP 1011:042 (2010); A. L. Fitzpatrick, W. Haxton, E. Katz, N. Lubbers, Y. Xu, JCAP 1302:004 (2013); R. J. Hill, M. P. Solon, Phys. Rev. Lett. 112, 211602 (2014); N. Anand, A. L. Fitzpatrick, W. Haxton, Phys.Rev. C89, 065501 (2014).

[45] D. Akerib et al., [arXiv:1310.8214]; M. Bossa, JINST 9 (2014) C01034; M. Boulay, J. Phy. Conf Ser. 375, 012027 (2012), [arXiv: 1203.0604]; L. Baudis, J. Phys. Conf. Ser. 375, 012028 (2012), [arXiv:1201.2402].

[46] Fermi-LAT Collaboration: M. Ackermann et al., Phys. Rev. D 89, 042001 (2014), [arXiv:1310.0828].

[47] V. Gammaldi, Proceeding of RICAP-14 "The Roma International Conference on Astroparticle Physics", [arXiv:1412.7639].

[48] F.Donato *et al.*, Phys. Rev. D 69, 063501 (2004);A. Barrau *et al.*, Astron. Astrophys. **388**, 676 (2002).

[49] L. C. Tan, L. K. Ng, Nucl. J. Phys. G 9, 227-242(1983). D. Maurin, F. Donato, R. Taillet, P. Salati, Astro. J. 555, 585-596 (2001); F. Donato and P. D. Serpico, Phys. Rev. D **83**, 023014 (2011); F. Donato *et al.*, Astrophys. J. **563**, 172 (2001).

[50] M.Cirelli, G.Corcella, A.Hektor, G.HŸtsi, M.Kadastik, P.Panci, M.Raidal, F.Sala, A.Strumia, JCAP 1103 (2011) 051.

[51] D. Bauer et al., Report prepared for the Community Summer Study (Snowmass) 2013, on behalf of Cosmic Frontier Working Groups 1-4 (CF1: WIMP Dark Matter Direct Detection, CF2: WIMP Dark Matter Indirect Detection, CF3: Non-WIMP Dark Matter, and CF4: Dark Matter Complementarity, [arXiv:1305.1605 [hep-ph]].

[52] C. Savage, G. Gelmini, P. Gondolo, K. Freese, JCAP 0904:010 (2009), [arXiv:0808.3607].

[53] A.V. Belikov, G. Zaharijas, J. Silk, Phys. Rev. D 86, 083516 (2012). A. A. Abdo et al. [arXiv:astro-ph.CO/1001.4531v1] (2010). M. Chernyakova *et. al.*, ApJ **726**, 60 (2011); T. Linden, E. Lovegrove and S. Profumo, arXiv:1203.3539 [astro-ph.HE]. K. Kosak, H. M. Badran, I. H. Bond et al., ApJ, 608, L97 (2004). F. Aharonian, A. G. Akhperjanian, K.M. Aye et al. A&A, 425, L13 (2004b). F. Aharonian, A. G. Akhperjanian, K.M. Aye et al. A&A, 503, 817 (2009). J. Albert, E. Aliu, H. Anderhub et al., ApJ, 638, L101 (2006). MAGIC collaboration, [arXiv:astro-ph/1103.0477v1] (2011). Maier G. [arXiv:astro-ph.IM/0907.5118v1] ; The CTA consortium [arXiv:astro-ph.IM/1003.3703v2]; http://www.cta-observatory.org/

[54] MAGIC collaboration, [arXiv:astro-ph/1103.0477v1] (2011).

[55] A. A. Abdo et al. [arXiv:astro-ph.CO/1001.4531v1] (2010). M. Chernyakova *et. al.*, ApJ **726**, 60 (2011); T. Linden, E. Lovegrove and S. Profumo, arXiv:1203.3539 [astro-ph.HE].

[56] K. Tsuchiya, R. Enomoto, L. T. Ksenofontov et al. ApJ, 606, L115 (2004).

[57] K. Kosak, H. M. Badran, I. H. Bond et al., ApJ, 608, L97 (2004).

[58] F. Aharonian, A. G. Akhperjanian, K.M. Aye et al. A&A, 425, L13 (2004b).

[59] F. Aharonian, A. G. Akhperjanian, K.M. Aye et al. A&A, 503, 817 (2009).

[60] J. Albert, E. Aliu, H. Anderhub et al., ApJ, 638, L101 (2006). MAGIC collaboration, [arXiv:astro-ph/1103.0477v1] (2011).

[61] V. Vitale, A. Morselli and f. t. F. /L. Collaboration, arXiv:0912.3828 [astro-ph.HE].

[62] D. Horns, Phys. Lett. B **607**, 225 (2005) [Erratum-ibid. B **611**, 297 (2005)].

[63] L. Bergstrom, T. Bringmann, M. Eriksson and M. Gustafsson, Phys. Rev. Lett. **94**, 131301 (2005); Phys. Rev. Lett. **95**, 241301 (2005).

[64] S. Profumo, Phys. Rev. D **72**, 103521 (2005).

[65] F. Aharonian *et. al.*, Phys. Rev. Lett. **97**, 221102 (2006).

[66] F. Aharonian and A. Neronov, ApJ **619**, 306 (2005).

[67] A. V. Belikov, G. Zaharijas and J. Silk, Phys. Rev. D **86**, 083516 (2012).

[68] R. M. Crocker, M. Fatuzzo, J. R. Jokipii et al., ApJ, 622, 892 (2005).

[69] J. A. R. Cembranos, V. Gammaldi, A.L. Maroto, JCAP **1304**, 051 (2013).

[70] Q. Wang, F. Lu and E. Gotthelf, MNRAS, 367, 937 (2006); B. Aschenbach, N. Grosso, D. Porquet, et. al., A&A 417, 71 (2004).

[71] T. Linden, E. Lovegrove and S. Profumo, Astrophys. J. **753**, 41 (2012);W.B. Atwood et al. [Fermi Coll.] ApJ 697 (2009) 1071-1102 [arXiv:0902.1089]; A.A. Abdo et al. [Fermi Coll.], Astrop. Phy. 32 (2009) 193-219 [arXiv:0904.2226] A.A. Abdo et al. [Fermi Coll.], Phy. Rev. Lett. 102 (2009) 181101 [arXiv:0905.0025] M. Ackermann et al. [Fermi Coll], Phy. Rev. D., [arXiv:0810.4995]

[72] A. Atoyan and C. D. Dermer, ApJ **617**, L123 (2004).

[73] G.R. Blumenthal, S.M. Faber, R. Flores, J. R. Primack, ApJ **301**, 27 (1986); O. Y. Gnedin, A. V. Kravtsov, A. A. Klypin and D. Nagai, ApJ **616**, 16 (2004).

[74] E. Romano-Díaz, I. Shlosman, Y. Hoffman, and C. Heller, ApJ **685**, L105 (2008); ApJ **702**, 1250 (2009); A. V. Maccio' *et. al.*, arXiv:1111.5620 [astro-ph.CO].

[75] P. Salucci, M. I. Wilkinson, M. G. Walker, G. F. Gilmore, E. K. Grebel, A. Koch, C. F. Martins and R. F. G. Wyse, arXiv:1111.1165 [astro-ph.CO].

[76] T. Sjostrand, S. Mrenna and P. Skands, JHEP05 (2006) 026 (LU TP 06-13, FERMILAB-PUB-06-052-CD-T) [hep-ph/0603175].

[77] J. F. Navarro, C. S. Frenk, and S. D. White, ApJ **490**, 493 (1997).

[78] Cohen-Tanugi, J., Pohl, M., Tibolla, O. and Nuss, E. 2009, in Proc. 31st ICRC (Lodz), 645 (http://icrc2009.uni.lodz.pl/proc/pdf/icrc0645.pdf)

[79] K. Griest and M. Kamionkowski, Phys. Rev. Lett. **64**, 615 (1990).

[80] J. Alcaraz *et al.*, Phys. Rev. D **67**, 075010 (2003); P. Achard *et al.*, Phys. Lett. **B597**, 145 (2004); J. A. R. Cembranos, A. Dobado and A. L. Maroto, Phys. Rev. **D65** 026005 (2002); Phys. Rev. **D70**, 096001 (2004); Phys. Rev. D **73**, 035008 (2006); Phys. Rev. D **73**, 057303 (2006); J. Phys. A **40**, 6631 (2007); J. A. R. Cembranos, J. L. Diaz-Cruz and L. Prado, Phys. Rev. D **84**, 083522 (2011). J. A. R. Cembranos, R. L. Delgado and A. Dobado, Phys. Rev. D **88**, 075021 (2013).

[81] A. Dobado and A. L. Maroto, Nucl. Phys. B **592**, 203 (2001); J. A. R. Cembranos, A. Dobado and A. L. Maroto, Phys. Rev. Lett. **90**, 241301 (2003); Phys. Rev. D **68**, 103505 (2003); A. L. Maroto, Phys. Rev. D **69**, 043509 (2004); Phys. Rev. D **69**, 101304 (2004); Int. J. Mod. Phys. **D13**, 2275 (2004). J. A. R. Cembranos *et al.*, JCAP **0810**, 039 (2008).

[82] J. A. R. Cembranos, A. Dobado and A. L. Maroto, Phys. Rev. D **68** 103505 (2003); astro-ph/0611911; AMS Collaboration, AMS Internal Note 2003-08-02

[83] MAGIC collaboration, [arXiv:astro-ph/1103.0477v1] (2011)

[84] J. Albert *et al.*, [ApJ, 667:358-366] (2007); L. Bergström and D. Hooper, [arXiv:hep-ph/0512317v2] (2006); http://www.magic.mppmu.mpg.de/introduction/techdetails.html

[85] H. U. Bengtsson, P. Salati and J. Silk, *Nucl.Phys.* B **346** 129, (1990)

[86] W. de Boer *et al.*, AIP Conf. Proc. **903** 607 (2007); L. Bergström *et al.*, JCAP **605** 006 (2006)

[87] W. B. Atwood *et al.*, arXiv:astro-ph.IM/0902.1089v1 (2009)

[88] A. A. Abdo *et al.*, arXiv:astro-ph.CO/1001.4531v1 (2010); M. L. Garde, arXiv:astro-ph.HE/1102.5701v1 (2011), L. Bergström and D. Hooper, arXiv:hep-ph/0512317v2 (2006).

[89] E. Komatsu *et al.* [WMAP Collaboration], ApJ. Suppl. 192 18 (2011).

[90] D. Nieto *et al.*, arXiv:1110.4744 [astro-ph.HE]; arXiv:1109.5935 [astro-ph.HE]

[91] G. Maier, arXiv:astro-ph.IM/0907.5118v1; The CTA consortium arXiv:astro-ph.IM/1003.3703v2; T. C. Consortium, arXiv:1111.2183 [astro-ph.IM]; http://www.cta-observatory.org/

[92] J. Aleksic *et al.*, arXiv:1109.6781 [astro-ph.CO]

[93] N. W. Evans, F. Ferrer and S. Sarkar, Phys. Rev. D **69**, 123501 (2004)

[94] L. Bergström, D. Hooper, arXiv:hep-ph/0512317v2 (2008)

[95] http://cossc.gsf.nasa.gov/egret/

[96] L. Bergström, P. Ullio and J. H. Buckley, *Astropart. Phys.* **9**, 137 (1998)

[97] P. Salucci *et al.*, arXiv:1111.1165 [astro-ph.CO]

[98] S. Rudaz and F. W. Stecker, Astrophys. J. **325**, 16 (1988); J. A. R. Cembranos, J. L. Feng, A. Rajaraman and F. Takayama, Phys. Rev. Lett. **95**, 181301 (2005); J. A. R. Cembranos, J. L. Feng and L. E. Strigari, Phys. Rev. Lett. **99**, 191301 (2007); Phys. Rev. D **75**, 036004 (2007); J. A. R. Cembranos and L. E. Strigari, Phys. Rev. D **77**, 123519 (2008); J. A. R. Cembranos, Phys. Rev. Lett. **102**, 141301 (2009); Phys. Rev. D **73**, 064029 (2006); T. Bringmann and C. Weniger, Phys. Dark Univ. **1**, 194 (2012). J. A. R. Cembranos, A. de la Cruz-Dombriz, V. Gammaldi, A.L. Maroto, Phys. Rev. D 85, 043505 (2012).

[99] Phys. Rev. Lett. **113**, 101101 (2014); J. A. R. Cembranos, V. Gammaldi and A. L. Maroto, Phys. Rev. D **90**, 043004 (2014); V. Gammaldi *et al.* arXiv:1404.2067 [hep-ph].

[100] R. M. Crocker, F. Melia and R. R. Volkas, arXiv:9911292v2; N.F. Bell, arXiv:0811.0847v1.

[101] K. C. Lai, G. L. Lin and T. C. Liu, Phys. Rev. D **80**, 103005 (2009).

[102] J.Beringer et al. (Particle Data Group), PR D86, 010001 (2012).

[103] M.G. Aartsen et al., IceCube Collaboration, arXiv:1212.4760v2 (2012).

[104] R. Abbasi et al., IceCube Collaboration, arXiv:1010.3980v2 (2010); M. G. Aartsen *et al.* [IceCube Collaboration], Astrophys. J. **779** (2013) 132.

[105] S. Adrian-Martinez et al. ANTARES Collaboration, Astrophy. J. 760:53(2012), arXiv:1207.3105 (2012); S. Schulte for the ANTARES Collaboration, icrc2013-0425.

[106] T. Seitz, R. Shanidze KM3NET Consortium, Nuclear Instrument and Methods in Physics Research A 626-627 (2011) S205-S207.

[107] R. M. Crocker, F. Melia, R. R. Volkas, arXiv:astro-ph: 0411471v4 (2003).

[108] N. Whitehorn, C. Kopper, N.K. Neilson for the IceCube Collaboration at IceCube Particle Astrophysics Symposium 2013, Madison, Wisconsin, USA; F. Halzen, S. Klein and C. Kopper, Proceedings of the 33th International Cosmic Ray Conference (http://www.cbpf.br/icrc2013); D. B. Fox, K. Kashiyama, P. Meszaros, arXiv:1305.6606v3 (2013); S. Razzaque, arXiv:1309.2756v1, http://astro.fnal.gov/events/Seminars/Slides/ NWhitehorn061013.pdf.

[109] S. D. Hunter *et al.*, Astrophys. J. **481**, 205 (1997).

[110] W. de Boer *et al.*, Astron. Astrophys. **444**, 51 (2005).

[111] F. W. Stecker, S. D. Hunter and D. A. Kniffen, Astropart. Phys. **29**, 25 (2008).

[112] A. A. Abdo *et al.* [Fermi-LAT Collaboration], Phys. Rev. Lett. **104**, 101101 (2010).

[113] D. Hooper and L. Goodenough, Phys. Lett. B **697**, 412 (2011);D. Hooper and T. Linden, Phys. Rev. D **84**, 123005 (2011).

[114] M. G. Aartsen *et al.* [IceCube Collaboration], Phys. Rev. Lett. **113**, 101101 (2014); J. A. R. Cembranos, V. Gammaldi and A. L. Maroto, Phys. Rev. D **90**, 043004 (2014); V. Gammaldi *et al.* arXiv:1404.2067 [hep-ph]; N. Whitehorn, C. Kopper, N.K. Neilson for the IceCube Collaboration at IceCube Particle Astrophysics Symposium 2013, Madison, Wisconsin, USA; F. Halzen, S. Klein and C. Kopper, Proceedings of the 33th International Cosmic Ray Conference (http://www.cbpf.br/icrc2013); D. B. Fox, K. Kashiyama and P. MÉszarÛs, Astrophys. J. **774**, 74 (2013).

[115] A. Boyarsky, D. Malyshev and O. Ruchayskiy, Phys. Lett. B **705**, 165 (2011).

[116] M. Chernyakova *et. al.*, ApJ **726**, 60 (2011); Astrophys. J. **726**, 60 (2011).

[117] K. N. Abazajian, JCAP **1103**, 010 (2011).

[118] F. W. Stecker, Astrophys. J. **212**, 60 (1977).

[119] T. Linden and S. Profumo, Astrophys. J. **714**, L228 (2010).

[120] A. W. Strong, I. V. Moskalenko and O. Reimer, Astrophys. J. **537**, 763 (2000) [Erratum-ibid. **541**, 1109 (2000)].

[121] M. Di Mauro *et. al.*, JCAP **1404**, 006 (2014); E. G. Berezhko and L. T. Ksenofontov, Astrophys. J. **791**, L22 (2014).

[122] http://press.web.cern.ch/sites/press.web.cern.ch/files/file/press/2015/04/pr05.15e_ams_days_resu

[123] T. Bringmann [arXiv: 0911.1124v1] (2009); N. Fornengo, L. Maccione and A. Vittino, JCAP **1404**, 003 (2014); I. Cholis, JCAP **1109**, 007 (2011). M. Cirelli, G. Giesen, CAP **1304**, 015 (2013); A. Ibarra, A. S. Lamperstorfer, J. Silk, Phys.Rev. D89, 063539 (2014).

[124] M. Cirelli, M. Kadastik, M. Raidal, A.Strumia, Nucl.Phys. B813, 1-21 (2009).

[125] C. Evoli, I. Cholis, D. Grasso, L. Maccione and P. Ullio, Phys. Rev. D **85**, 123511 (2012).

[126] T. Bringmann, M. Vollmann and C. Weniger, arXiv:1406.6027 [astro-ph.HE]; M. Cirelli, D. Gaggero, G. Giesen, M. Taoso and A. Urbano, arXiv:1407.2173 [hep-ph]; J. Lavalle, D. Maurin and A. Putze, Phys. Rev. D **90**, 081301 (2014); M. di Mauro, F. Donato, A. Goudelis and P. D. Serpico, Phys. Rev. D **90**, no. 8, 085017 (2014); D. Hooper, T. Linden and P. Mertsch, arXiv:1410.1527 [astro-ph.HE].

[127] O. Adriani *et al.* [PAMELA Collaboration], Nature 458, 607 (2009); Phys. Rev. Lett. **105**, 121101 (2010).

[128] J. A. R. Cembranos, V. Gammaldi, A. L. Maroto, JCAP 03, 041 (2015).

[129] R. M. Crocker, D. I. Jones, F. Aharonian, C. J. Law, F. Melia, T. Oka and J. Ott, Mon. Not. Roy. Astron. Soc. **413**, 763 (2011).

[130] B. C. Lacki, Monthly Notices of the Royal Astronomical Society: Letters (2014), 444, L39.

[131] T. Delahaye *et al.*, Phys. Rev. D 77, 063527 (2008).

[132] F. Melia, Astrophys. J. 387, L25-L28 (1992); G. Bertone, G. Sigl and J. Silk, Mon. Not. Roy. Astron. Soc. **337**, 98 (2002).

[133] T. Bringmann, M. Vollmann and C. Weniger, Phys. Rev. D **90**, no. 12, 123001 (2014).

[134] J. S. Perko, A & A 184, 119 (1987).

[135] M. Cirelli, D. Gaggero, G. Giesen, M. Taoso and A. Urbano, arXiv:1407.2173 [hep-ph]; T. Bringmann and P. Salati, Phys.Rev.D 75, 083006 (2007).

[136] R. Kappl and M. W. Winkler, JCAP **1409**, no. 09, 051 (2014).

[137] A. Morselli, Conference series 259, 012011 (2010), PASCOS 2010.

[138] T. Bringmann and P. Salati, Phys. Rev. D **75**, 083006 (2007).

[139] J. A. R. Cembranos, A. de la Cruz-Dombriz, V. Gammaldi, R. A. Lineros and A. L. Maroto, JHEP **1309**, 077 (2013).

[140] D. Hooper, C. Kelso and F. S. Queiroz, Astropart. Phys. **46**, 55 (2013).

[141] M. H. Seymour and M. Marx, arXiv:1304.6677 [hep-ph].

[142] J. A. R. Cembranos, A. de la Cruz-Dombriz, V. Gammaldi, R. A. Lineros, A. L. Maroto, JHEP 1309, 077 (2013).

[143] J. Beringer *et al.* [Particle Data Group Collaboration], Phys. Rev. D **86**, 010001 (2012).

[144] G. Altarelli and G. Parisi, Nucl. Phys. B **126**, 298 (1977).

[145] G. Marchesini and B.R. Webber, Nucl. Phys. B **238** 1 (1984); Nucl. Phys. B **310** 461 (1988).

[146] T. Sjöstrand and P. Skands, Eur. Phys. J. C **39** 129 (2005).

[147] Catani, Webber, Marchesini, Nucl. Phys. B349 (1991) 635-654.

[148] T. Sjöstrand, S. Mrenna, P. Skands, arXiv:0603175 [hep-ph].

[149] T. Sjöstrand, S. Mrenna, P. Skands, arXiv:0710.3820v1 [hep-ph]; http://home.thep.lu.se/ torbjorn/pythia81.html

[150] G. Corcella *et al.*, arXiv:0011363v3 [hep-ph].

[151] M. Bähr *et al.*, arXiv:0803.0883v3 [hep-ph]. S. Gieseke et al., arXiv:1102.1672v1 [hep-ph], K. Arnold et al., arXiv:1205.4902v1 [hep-ph].